

ABSTRACT

LEWIS, NICOLE MARIE. A Thermomechanically Coupled SMA Actuator Model for Finite Element Simulations of Adaptive Structures. (Under the direction of Stefan Seelecke).

This work presents a thermomechanically coupled Shape Memory Alloy (SMA) actuator model used to simulate adaptive structures in Finite Element Analyses. The model is based on the mesoscopic free energy model [1] to accurately describe the thermomechanically coupled actuator behavior of SMA wires. The commercially available FEA program ABAQUS and its user material feature UMAT were used to test and validate the SMA model for wires with homogeneous and inhomogeneous temperature profiles. The implementation was validated for SMA wires actuated under a constant load, attached to a spring element, an elastic beam and to another SMA wire for both adiabatic and isothermal temperature boundary conditions. The model is then used to simulate the displacement of an adaptive nozzle structure which is actuated by controlling the power to six SMA wires simultaneously. The results from this simulation were compared with experimental measurements taken with a current adaptive nozzle prototype. During the simulations, the required heat input, wire temperature, phase fraction changes, resulting strains, stresses, and the mechanical interactions with the structures were determined for each SMA wire. In simulations with more than one wire, second order effects of wire coupling were also observed and analyzed.

A Thermomechanically Coupled SMA Actuator Model for Finite Element Simulations of
Adaptive Structures

by
Nicole Lewis

A thesis submitted to the Graduate Faculty of
North Carolina State University
in partial fulfillment of the
requirements for the Degree of
Master of Science

Mechanical Engineering

Raleigh, North Carolina

2011

APPROVED BY:

Dr. Stefan Seelecke
Chair of Advisory Committee

Dr. Jeffery Eischen

Dr. Lawrence Silverberg

DEDICATION

This work* is dedicated to my parents: Patti and Paul Lewis. Thank you for all of your endless love, support and encouragement. I would not have made it this far without you!

*Note: I tried to make the title as simple as possible for you.

BIOGRAPHY

Nicole Lewis earned her undergrad degree at North Carolina State University in Biomedical Engineering with a concentration in Biomechanics. As a sophomore, she began working in the Adaptive Structures Laboratory under the direction of Dr. Seelecke on biomedically-based, multifunctional material projects. After graduation, she interned under Anita Bestelmeyer with the Computer-Aided-Engineering (CAE) group at Becton Dickinson in Research Triangle Park, NC, where she learned ABAQUS. She started her Master's degree in Mechanical Engineering with Dr. Seelecke in August of 2009 and began working with ABAQUS and modeling the behavior of Shape Memory Alloys. In January of 2011 she moved with the NCSU Adaptive Structures Laboratory to Saarbrücken, Deutschland, to continue working with Dr. Seelecke on the SMA modeling project at the Universität des Saarlandes. Nicole completed her Masters in Saarbrücken in May of 2011.

ACKNOWLEDGMENTS

I would first like to thank my advisor, Dr. Stefan Seelecke, for all of his encouragement, support, and guidance throughout the past 4 and a half years. It has been an honor and a privilege to work with you, “Vielen Dank!”

I would also like to thank my committee members, Dr. Jeffrey Eischen and Dr. Lawrence Silverberg for being on my committee and for their support throughout my graduate career at NC State. Also, I would especially like to thank Dr. Travis Turner at NASA Langley for all of his helpful discussions and support.

Thank you to Anita Bestelmeyer and the entire CAE Dream Team at BD for an invaluable internship with ABAQUS. You all are the best!

I would like to thank my labmates: Aseem Deodhar, Stephen Furst, Micah Hodgins, and Dr. Alexander York. We may not have a supersonic-waterball launcher in Deutschland, but at least we have Chris Tucker and Jackie Chan!

Last but not least, I would like to thank my wonderful parents Patti and Paul and my beautiful, talented sisters Jennifer and Michelle. Thank you for all of your love, support and understanding. You mean the world to me.

TABLE OF CONTENTS

List of Tables	vii
List of Figures	viii
Introduction.....	1
1.1 Motivation and Background.....	1
1.2 Literature Review of Current SMA Models	4
1.3 Thesis Objectives and Outline	8
SMA Model	10
2.1 Introduction.....	10
2.2 Main Equations	10
2.3 FEA Implementation.....	14
Simulations	16
3.1 Homogenous Temperature Profiles.....	16
3.1.1 Simulation 1: SMA Wire Initial Testing	17
3.1.1.1 Geometry and Parameters	17
3.1.1.2 Results.....	18
3.1.2 Simulation 2: SMA Wire with Concentrated Load	22
3.1.2.1 Geometry and Parameters	22
3.1.2.2 Results	24
3.1.3 Simulation 3: SMA Wire and Elastic Beam	27
3.1.3.1 Geometry and Parameters	27
3.1.3.2 Results	29
3.1.4 Simulation 4: Adaptive Nozzle in Smart Inhaler.....	34
3.1.4.1 Adaptive Nozzle Overview	34
3.1.4.2 Geometry and Assembly	35
3.1.4.3 Simulation Parameters.....	37
3.1.4.4 Results	38
3.1.4.5 Comparison with Actual Data.....	42
3.2 Inhomogeneous Temperature Profiles	43
3.2.1 Simulation 5: SMA Wire with Concentrated Load	44
3.2.1.1 Geometry and Parameters	44
3.2.1.2 Results: Adiabatic Boundary Conditions	46
3.2.1.3 Results: Isothermal Boundary Conditions.....	51
3.2.1.4 Results: Comparison	59
3.2.2 Simulation 6: SMA Wire and Spring.....	60
3.2.2.1 Geometry and Parameters	60
3.2.2.2 Results: Adiabatic Boundary Conditions	62
3.2.2.3 Results: Isothermal Boundary Conditions.....	67
3.2.2.4 Results: Comparison	74
3.2.3 Simulation 7: Dueling Wires	77
3.2.3.1 Geometry and Parameters	78
3.2.3.2 Results	79
3.2.4 Simulation 8: SMA Wire and Elastic Beam	89

3.2.4.1 Geometry and Parameters	89
3.2.4.2 Results: Adiabatic Boundary Conditions	91
91	
3.2.4.3 Results: Isothermal Boundary Conditions	96
3.2.4.4 Results: Comparison	103
Conclusions.....	105
References.....	107
Appendices.....	110
Appendix A: Homogeneous Temperature Profile, SMA Wire with Prestress	111
Appendix B: Homogeneous Temperature Profile, SMA Wire and Spring	114
Appendix C: UMAT Code.....	118

LIST OF TABLES

Table 1: Simulation 1: Initial Conditions and Model Parameters.....	18
Table 2: Simulation 2: Initial Conditions and Model Parameters.....	23
Table 3: Simulation 3: Initial Conditions and Model Parameters.....	28
Table 4: Simulation 4: Geometric Data.....	36
Table 5: Simulation 4: Model Parameter List.....	37
Table 6: Simulation 5: Initial Conditions and Model Parameters.....	45
Table 7: Simulation 6: Initial Conditions and Model Parameters.....	62
Table 8: Simulation 6, Case 2: Initial Conditions and Model Parameters.....	76
Table 9: Simulation 7: Initial Conditions and Model Parameters.....	79
Table 10: Simulation 8: Initial Conditions and Model Parameters.....	90
Table 11: SMA with Prestress, Initial Conditions and Model Parameters.....	111
Table 12: SMA with Spring, Initial Conditions and Model Parameters.....	115

LIST OF FIGURES

Figure 1: Behavior of SMA crystals under deformation, heating, and cooling.	2
Figure 2: Flow of Analysis.....	14
Figure 3: Simulation 1 schematic: SMA wire initial testing.....	17
Figure 4: Time resolved concentrated load input to SMA wire and corresponding phase fractions, strain and stress responses at T=273K.	18
Figure 5: (a) Displacement versus time response and (b) stress versus strain relationship at T=273K.	19
Figure 6: Time resolved concentrated load input to SMA wire and corresponding phase fractions, strain and stress responses at T=273K, 300K, 350K, 400K, and 450K.....	20
Figure 7: (a) Displacement versus time response and (b) stress versus strain relationship at T=273K, 300K, 350K, 400K, and 450K.....	21
Figure 8: Simulation 2 Schematic: SMA wire with a concentrated load and actuation.	23
Figure 9: Time resolved concentrated load and power input to SMA actuator and corresponding temperature, phase fractions, strain and stress responses.	24
Figure 10: SMA wire tip displacement versus time response.....	26
Figure 11: (a) Stress versus strain and (b) strain versus temperature relationships.	26
Figure 12: Simulation 3 schematic: SMA wire coupled with a 3-D elastic beam and actuation.....	28
Figure 13: Time resolved power input to SMA actuator and corresponding temperature, phase fractions, strain and stress responses.	29
Figure 14: SMA wire tip displacement versus time response.....	30
Figure 15: (a) Stress versus strain and (b) strain versus temperature relationships.	31
Figure 16: Time resolved power input to SMA actuator and corresponding temperature, phase fractions, strain and stress responses for different beam stiffness values.....	32
Figure 17: SMA wire tip displacement versus time response for different beam stiffness values.	33
Figure 18: (a) Adaptive nozzle prototype and FEA model. (b), (c) Adaptive nozzle geometry and SMA wire attachment.	35
Figure 19: Time resolved power input to SMA actuators and corresponding temperature, phase fractions, strain and stress responses for t=21-64s.	38
Figure 20: Multi-wire effects due to structural coupling. (a) Phase fractions versus time, (b) strain versus time, (c) stress versus time for t=29-35s.....	39
Figure 21: (a) Nozzle tip displacement. (b) Nozzle during actuation of wires 3 & 6.....	41
Figure 22: Prototype and simulation results [29].....	42
Figure 23: Simulation 5 schematic: SMA wire with a concentrated load and actuation for adiabatic and isothermal boundary conditions.....	45
Figure 24: Time resolved concentrated load and power input to SMA actuator and corresponding temperature, phase fractions, strain and stress responses for adiabatic boundary conditions.....	46

Figure 25: SMA Wire tip displacement versus time response for adiabatic boundary conditions.....	48
Figure 26: (a) Stress versus strain and (b) strain versus temperature relationships for adiabatic boundary conditions.	48
Figure 27: Evolution of (a) temperature and (b) martensite+ along the length of the SMA wire from t=12 to 15s for adiabatic boundary conditions.....	49
Figure 28: Evolution of (a) strain and (b) stress along the length of the SMA wire from t=12 to 15s for adiabatic boundary conditions.	50
Figure 29: Evolution of (a) temperature and (b) martensite+ along the length of the SMA wire from t=15-18s for adiabatic boundary conditions.	50
Figure 30: Evolution of (a) strain and (b) stress along the length of the SMA wire from t=15-18s for adiabatic boundary conditions.	51
Figure 31: Time resolved concentrated load and power input to SMA actuator and corresponding temperature, phase fractions, strain and stress responses for isothermal boundary conditions.....	51
Figure 32: SMA wire tip displacement versus time response for isothermal boundary conditions.....	53
Figure 33: (a) Stress versus strain and (b) strain versus temperature relationships for isothermal boundary conditions.....	54
Figure 34: Evolution of (a) temperature and (b) martensite+ along the length of the SMA wire from t=12-15s for isothermal boundary conditions.	55
Figure 35: Evolution of (a) strain and (b) stress along the length of the SMA wire from t=12 to 15s for isothermal boundary conditions.....	55
Figure 36: Evolution of heating along the length of the SMA wire from t=14.5-14.95s.	56
Figure 37: Evolution of martensite+ along the length of the SMA wire from t=14.5-14.95s.	56
Figure 38: Evolution of (a) temperature and (b) martensite+ along the length of the SMA wire from t=15-18s for isothermal boundary conditions.	57
Figure 39: Evolution of (a) strain and (b) stress along the length of the SMA wire from t=15-18s for isothermal boundary conditions.....	57
Figure 40: Evolution of temperature along the length of the SMA wire from t=16.7-17.1s.	58
Figure 41: Evolution of martensite+ along the length of the SMA wire from t=16.7-17.1s.	58
Figure 42: Displacement comparison of an actuated SMA wire under a concentrated load with homogeneous and inhomogeneous temperature profiles.....	59
Figure 43: Simulation 6 schematic: single SMA wire attached to a spring with actuation for adiabatic and isothermal boundary conditions.....	61
Figure 44: Time resolved power input to SMA actuator and corresponding temperature, phase fractions, strain and stress responses for adiabatic boundary conditions.	62
Figure 45: SMA Wire tip displacement versus time response for adiabatic boundary conditions.....	64
Figure 46: (a) Stress versus strain and (b) strain versus temperature relationships for adiabatic boundary conditions.	64
Figure 47: Evolution of (a) temperature and (b) martensite+ along the length of the SMA wire from t=9-12s for adiabatic boundary conditions.....	65

Figure 48: Evolution of (a) strain and (b) stress along the length of the SMA wire from t=9-12s for adiabatic boundary conditions.	65
Figure 49: Evolution of (a) temperature and (b) martensite+ along the length of the SMA wire from t=12-15s for adiabatic boundary conditions.	66
Figure 50: Evolution of strain and stress along the length of the SMA wire from t=12-15s for adiabatic boundary conditions.	66
Figure 51: Time resolved power input to SMA actuator and corresponding temperature, phase fractions, strain and stress responses for isothermal boundary conditions.	67
Figure 52: SMA Wire tip displacement versus time response for isothermal boundary conditions.	68
Figure 53: (a) Stress versus strain and (b) strain versus temperature relationships for isothermal boundary conditions.	69
Figure 54: Evolution of (a) temperature and (b) martensite+ along the length of the SMA wire from t=9-12s for isothermal boundary conditions.	70
Figure 55: Evolution of (a) strain and (b) stress along the length of the SMA wire from t=9-12s for isothermal boundary conditions.	70
Figure 56: Evolution of temperature along the length of the SMA wire from t=11.2-11.7s.	71
Figure 57: Evolution of martensite+ along the length of the SMA wire from t=11.2-11.7s.	71
Figure 58: Evolution of (a) temperature and (b) martensite+ along the length of the SMA wire from t=12-15s for isothermal boundary conditions.	72
Figure 59: Evolution of (a) strain and (b) stress along the length of the SMA wire from t=12-15s for isothermal boundary conditions.	72
Figure 60: Evolution of temperature along the length of the SMA wire from t=13.2-13.6s.	73
Figure 61: Evolution of martensite+ along the length of the SMA wire from t=13.2-13.6s.	73
Figure 62: Displacement comparison of an actuated SMA wire attached to a spring with homogeneous and inhomogeneous temperature profiles.	74
Figure 63: Simulation 6, Case 2 schematic: single SMA wire attached to a spring with actuation for adiabatic and isothermal boundary conditions.	75
Figure 64: Displacement comparison between adiabatic and isothermal boundary conditions.	76
Figure 65: Simulation 7 Schematic: Two SMA wires attached to each other with actuation.	78
Figure 66: Time resolved power input to two SMA actuators and corresponding temperature, phase fractions, strain and stress responses.	79
Figure 67: Displacement of the SMA wire connection point versus time response.	80
Figure 68: Evolution of temperature along the length of SMA wires 1 and 2 from t=12-15s.	82
Figure 69: Evolution of martensite+ along the length of SMA wires 1 and 2 from t=12-15s.	83
Figure 70: Evolution of strain along the length of SMA wires 1 and 2 from t=12-15s.	83
Figure 71: Evolution of stress along the length of SMA wires 1 and 2 from t=12-15s.	84
Figure 72: Evolution of latent heats as a result of phase transformation occurring in SMA wire 2 from t=12-13s.	84

Figure 73: Evolution of martensite+ as a result of phase transformation occurring in SMA wire 2 from t=12-13s.	85
Figure 74: Evolution of temperature along the length of SMA wires 1 and 2 from t=15-18s.	86
Figure 75: Evolution of martensite+ along the length of SMA wires 1 and 2 from t=15-18s.	86
Figure 76: Evolution of strain along the length of SMA wires 1 and 2 from t=15-18s.	87
Figure 77: Evolution of stress along the length of SMA wires 1 and 2 from t=15-18s.	87
Figure 78: Second order effects due to wire coupling. a) Temperature versus time, b) phase fractions versus time, c) strain versus time for t=6-9s.	88
Figure 79: Simulation 8 schematic: SMA wire coupled with a 3-D elastic beam for adiabatic and isothermal boundary conditions.	90
Figure 80: Time resolved power input to SMA actuator and corresponding temperature, phase fractions, strain and stress responses for adiabatic boundary conditions.	91
Figure 81: SMA wire tip displacement versus time response for adiabatic boundary conditions.	92
Figure 82: (a) Stress versus strain and (b) strain versus temperature relationships for adiabatic boundary conditions.	93
Figure 83: Evolution of (a) temperature and (b) martensite+ along the length of the SMA wire from t=9-12s for adiabatic boundary conditions.	94
Figure 84: Evolution of (a) strain and (b) stress along the length of the SMA wire from t=9-12s for adiabatic boundary conditions.	94
Figure 85: Evolution of (a) temperature and (b) martensite+ along the length of the SMA wire from t=12-15s for adiabatic boundary conditions.	95
Figure 86: Evolution of strain and stress along the length of the SMA wire from t=12-15s for adiabatic boundary conditions.	95
Figure 87: Time resolved power input to SMA actuator and corresponding temperature, phase fractions, strain and stress responses for isothermal boundary conditions.	96
Figure 88: SMA Wire tip displacement versus time response for isothermal boundary conditions.	97
Figure 89: (a) Stress versus strain and (b) strain versus temperature relationships for isothermal boundary conditions.	98
Figure 90: Evolution of (a) temperature and (b) martensite+ along the length of the SMA wire from t=9-12s for isothermal boundary conditions.	99
Figure 91: Evolution of (a) strain and (b) stress along the length of the SMA wire from t=9-12s for isothermal boundary conditions.	99
Figure 92: Evolution of temperature along the length of the SMA wire from t=11-11.7s. .	100
Figure 93: Evolution of martensite+ along the length of the SMA wire from t=11-11.7s. .	100
Figure 94: Evolution of (a) temperature and (b) martensite+ along the length of the SMA wire from t=12-15s for isothermal boundary conditions.	101
Figure 95: Evolution of (a) strain and (b) stress along the length of the SMA wire from t=12-15s for isothermal boundary conditions.	101
Figure 96: Evolution of temperature along the length of the SMA wire from t=13.5-14s. .	102
Figure 97: Evolution of martensite+ along the length of the SMA wire from t=13.5-14s. .	102

Figure 98: Displacement comparison of an SMA wire attached to an elastic beam with homogeneous and inhomogeneous temperature profiles.	103
Figure 99: SMA wire with prestress schematic.	111
Figure 100: Time resolved concentrated load and power input to SMA actuator and corresponding temperature, phase fractions, strain and stress responses.	112
Figure 101: SMA Wire tip displacement versus time response.	112
Figure 102: (a) Stress versus strain and (b) strain versus temperature relationships.	113
Figure 103: Time resolved power input to SMA actuator and corresponding temperature, phase fractions, strain and stress responses for different initial prestress values.	114
Figure 104: SMA wire with spring schematic.	114
Figure 105: Time resolved concentrated load and power input to SMA actuator and corresponding temperature, phase fractions, strain and stress responses.	115
Figure 106: SMA Wire tip displacement versus time response.	116
Figure 107: (a) Stress versus strain and (b) strain versus temperature relationships.	116
Figure 108: SMA wire tip displacement for different spring stiffness values.	117
Figure 109: Time resolved power input to SMA actuator and corresponding temperature, phase fractions, strain and stress responses for different spring stiffness values.	117

Chapter 1

Introduction

1.1 Motivation and Background

Shape Memory Alloy (SMA) wires are attractive materials for use in adaptive structures because of their superelastic and actuation capabilities. However, building and testing adaptive structure prototypes with multiple SMA wires and materials is a very time consuming and expensive process. Thus, there is an inherent need for modeling efforts, such as finite element tools, that are capable of coupling the non-linear SMA material in smart structures. As superelastic isothermal SMA models can already be found in commercial FE codes such as ANSYS or ABAQUS, actuator models which require simultaneous solution of momentum balance and heat transfer are not yet available. The current work addresses this through an implementation of a fully coupled thermo-mechanical SMA model in ABAQUS through its user material interface UMAT.

Shape memory alloys exhibit superelastic, quasiplastic, and actuation properties. Their superelastic property allows for them to be stretched or compressed to 6-8% beyond their initial shape without failure. When the load is removed the SMAs return to their original shape. SMAs can also exhibit quasiplastic behavior by remaining deformed until an external heat source is applied to restore them to their original shape. Lastly, SMAs can be used as linear actuators. When a voltage is applied across an SMA wire, the wire undergoes a phase

transformation which causes contraction by decreasing the wire's strain and thus providing a linear stroke. SMA wire actuators are small, lightweight, and have replaced many bulky gear systems.

Shape memory alloys are composed of many microscopic regularly-shaped crystals which are oriented in layers. In a one-dimensional setting appropriate for wire actuators, these crystals exist in one of three phases: martensite-, austenite, and martensite+. The amount of each phase depends on external forces and temperature applied to the SMA. At low temperatures, the martensite mixture prevails in the unloaded state with martensite+ favoring tensile loads and martensite- favoring compressive loads. This mixture can be de-twinned by the application of a load, which leads to substantial permanent elongation. During heating, SMAs transform from a loaded martensite+ or martensite- state to austenite, thereby contracting and recovering the former shape. Figure 1 below illustrates the behavior of the shape memory crystals under deformation and heating.

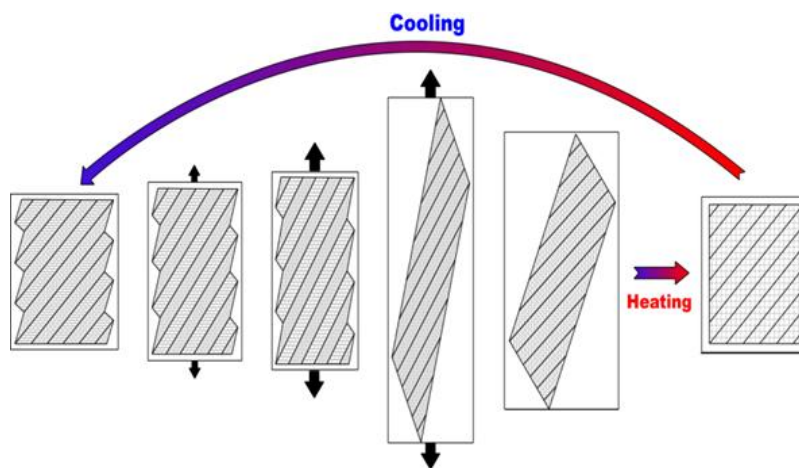


Figure 1: Behavior of SMA crystals under deformation, heating, and cooling.

SMA are most commonly incorporated into biomedical devices, aerospace and mechanical applications. In biomedicine, SMA arterial stents use the superelastic property of SMA wires to their advantage. SMA stents are able to be compressed inside tiny catheters and then return to their original shape after being deployed at an aneurysm site. SMA are also being investigated as actuators inside catheters to make “active catheters,” which are able to navigate through the circulatory system without having to substitute the catheter head when the blood vessels change shape [2]. In aerospace applications, SMA are used for their actuation properties to change the shape of aircraft wings and tails. Morphing aircraft wings have been investigated by [3]. SMA are also being studied to assist in the reduction of jet aircraft noise by way of adaptive jet exhaust-nozzle chevron systems [4]. In other mechanical applications, SMA wires have been used as actuators and have replaced gears and pistons in assembly lines.

The time and cost required to build and test SMA structures for can be very large, but finite element software has the ability to simulate and analyze structures without being very expensive and time consuming, which makes them valuable tools in the design process. Unfortunately, commercially available FEA software does not currently include built-in models that accurately simulate both the pseudoelastic and actuation behavior of SMA materials. However, FEA software does contain user material subroutine interfaces that have the ability to introduce user-defined non-linear, thermomechanically coupled actuation material models. Current FEA software with user materials include ANSYS, ABAQUS, and COMSOL.

1.2 Literature Review of Current SMA Models

There are two main types of SMA models: phenomenological and physics based models. Phenomenological models use experimental data to construct a phase diagram in order to predict the behavior of SMAs. Physics based models use equations from thermodynamics and statistics to predict phase transformations and stress/strain states. Within these two groups there are models capable of incorporating actuation and models without actuation.

A literature survey revealed a variety of SMA models being used to simulate single wire behavior and wires coupled with a structure in finite element programs such as COMSOL, ANSYS, and ABAQUS. A large database of superelastic, isothermal SMA models are already being used in simulations. Saleeb and Kumar [5] used the UMAT subroutine in ABAQUS to implement a phenomenological viscoelasticplastic SMA model. They conducted cyclic single-wire tensile tests under small strain rates to simulate nearly isothermal conditions. Mangalgi and Thakare [6] also used ABAQUS UMAT to model SMAs under stress loading with beam elements and the phenomenological Buravalla and Khandelwal model. Thamburaja and Nikabdullah [7] used ABAQUS Explicit and UMAT to implement a phenomenological NiTi model. They simulated a polycrystalline NiTi rod undergoing displacement controlled small strain rate deformations under isothermal conditions. They investigated non-isothermal behavior of an SMA ribbon by adjusting the strain rate in a displacement controlled simulation. They also used a surface film feature to implement convective cooling during mechanical deformation. Kleinstreuer et al [8] used a

built-in ABAQUS superelastic Nitinol UMAT to model the behavior of a Nitinol stent graft undergoing deformation. The ABAQUS NiTi superelastic user material is based on additive strain decomposition and used in isothermal simulations. Vidal et al [9] studied the force versus stroke of a Nitinol wire at constant temperature in ABAQUS Explicit. They used a Nitinol user material routine developed by Hibbitt, Karlsson and Sorensen. Peultier et al [10] investigated the force versus displacement characteristics of a superelastic NiTi ring at different temperatures. They incorporated a phenomenological SMA model within the UMAT subroutine in ABAQUS and used axisymmetrical solid elements to model the structure. The hysteresis of the NiTi ring for loading and unloading without plasticity effects was analyzed. Wang et al [11] implemented a phenomenological NiTi SMA model into ABAQUS UMAT in order to simulate a thin-wall tube under non-proportional extension-torsion loading. The tube was modeled using 8-node continuous brick elements and the simulation was conducted under isothermal and time independent conditions. Bouvet et al [12] used a phenomenological 3-D model to describe the major SMA macroscopic pseudoelastic behavior of Cu–Al–Be polycrystalline SMA without actuation. Auricchio et al [13, 14] have developed a phenomenological SMA model under large strains and homogeneous temperature profiles to model stent and orthodontic archwire deformation.

A few simulations incorporate actuation in addition to the superelastic behavior of SMA wires. Chang et al [15] developed a phenomenological continuum model to explain SMA wire behavior under uniaxial loading using an in-house FE code. Simulations were conducted

for a wire in room temperature air in the absence of joule heating and were able to match the displacement controlled experiments of clamped SMA wires. They also performed actuator simulations on a single SMA wire. Frautschi and Seelecke [16] used a physics based SMA model [1] to simulate an adaptive beam and adaptive airfoil wing components with joule heating. They used the usermat subroutine in ANSYS and modeled the SMA wires using 3-D link elements [17]. Yang and Seelecke [18] implemented the same SMA model into COMSOL to simulate the motion of a solid, 3-D elbow joint actuated by SMA wires. Li also implemented the same SMA model into the usermat subroutine of ANSYS to simulate an SMA beam bending with actuation [19]. Richter et al [20] implemented a physics based polycrystalline SMA model [21, 22] into the UMAT subroutine in ABAQUS. They modeled a NiTi wire using coupled temperature-displacement brick elements and performed strain controlled and actuation experiments. Roh et al [23] modified a 3-D model developed by Lagoudas into a 2-D incremental, plane stress model. They used shell elements to model NiTi SMA ribbons as film type actuators within ABAQUS UMAT. Roh et al [24] also developed a 3-D SMA thermomechanical model based on the aforementioned Lagoudas phenomenological model to consider large displacements, large strains, and material nonlinearity. They used 8-noded brick elements to model SMAs in ABAQUS UMAT.

The models briefly explained above are excellent tools for understanding SMA materials, in particular under isothermal and small strain-controlled simulations. However literature reviews returned very few models that account for actuation in addition to superelastic

behavior. This is because actuation requires a thermomechanically coupled SMA model. In addition, few SMA models use wire elements to model SMA wires, despite the fact that probably 95% of SMA actuator use one-dimensional wires. Wire elements are applicable for uniaxial SMA models and do not require as much computation time compared to other elements because they have less degrees of freedom per element. Also, the literature review did not reveal any simulations performed on 3-D structures involving multiple SMA wires. The simulations presented in this thesis were modeled using ABAQUS and the SMA model was implemented via the UMAT subroutine. The SMA model was written using the mesoscopic free energy model [1] which describes the thermomechanically coupled behavior of a uniaxial wire for the single crystal formulation.

By implementing this model via UMAT, the behavior of single and multi-wire adaptive structures through wire actuation will be accurately simulated. The UMAT feature will be able to represent the thermomechanical behavior of the wires as well as wire coupling. In addition, the use of wire elements with six total degrees of freedom per element will result in a lower simulation time compared with other elements. This SMA model tool implemented into finite element software will assist in the development and testing of adaptive structure prototypes with superelasticity and actuation.

1.3 Thesis Objectives and Outline

The objective of this work is to implement a thermomechanically coupled SMA actuator model into finite element software and simulate both single and multi-wire adaptive structures. The physics based, mesoscopic free energy model will accurately be able to simulate both the pseudoelastic and actuation behavior of SMA materials.

First, the SMA model equations and its implementation into the finite element software ABAQUS is explained. Then, initial simulations conducted with SMA wires using uniaxial, 3-D wire elements under homogeneous temperature profiles are presented. The first simulation consists of a single SMA wire with an applied load at constant temperature. In Simulation 2 an SMA wire was actuated with a constant, concentrated load at one end. An SMA wire was also coupled with a 3-D elastic beam and cyclically actuated. The last simulation conducted under homogeneous temperature profiles was a multi-wire, 3-D adaptive nozzle structure. The resulting behavior of the adaptive nozzle from the simulation was compared against actual data taken in the laboratory.

The next group of simulations were conducted with SMA wires using uniaxial, coupled temperature-displacement 3-D wire elements under inhomogeneous temperature profiles. The first inhomogeneous simulation consists of a single SMA wire with a concentrated load and actuation for adiabatic and isothermal boundary conditions. The displacement results from this simulation and Simulation 2 are compared and the differences are analyzed. In Simulation 6 an SMA wire is coupled with a spring for adiabatic and isothermal boundary

conditions. These displacement results are also compared with the results from the homogeneous simulation which is included in Appendix B. The next simulation studies two SMA wires tied to each other and the effects of wire coupling under inhomogeneous temperature profiles. The last simulation consists of an SMA wire attached to a 3-D, elastic beam with adiabatic and isothermal boundary conditions. These displacement results are also compared with the results from the homogeneous Simulation 3. This work ends with the conclusions, references and appendix.

Chapter 2

SMA Model

2.1 Introduction

The model is based on the mesoscopic free energy model developed by Müller-Achenbach-Seelecke for single crystal SMA wires [1]. The model uses equations derived from thermodynamics and mechanics to explain the macroscopic stress-strain behavior of the SMA material under uniaxial loading. The model also accounts for the changing wire temperature during loading through an energy balance equation. Simulations were conducted that show the SMA wire's stress and strain behavior in response to a variety of loading conditions including applied Joule heating. The model was written entirely in FORTRAN and implemented into ABAQUS using the User Material (UMAT) subroutine. The following subsections contain an overview of this SMA model.

2.2 Main Equations

SMA actuator behavior is controlled through Joule heating and mechanical loading. The combination of heat and stress result in phase transformations between the austenitic and martensitic phases and thus material deformation. The balance of energy for an SMA with a homogeneous temperature profile is given as

$$mc\dot{T} = -k(T - T_E(t)) + j(t) - \dot{x}^+ H^+(\sigma) - \dot{x}^- H^-(\sigma) \quad (1)$$

where m is the mass of the SMA material, c is the specific heat and \dot{T} is the rate of change of temperature with time. For inhomogeneous temperature profiles, the $mc \dot{T}$ term in Eq (1) is replaced by a local energy change and a flux term, which results in

$$\rho c \frac{\partial T}{\partial t} - \lambda \frac{\partial^2 T}{\partial x^2} = -k(T - T_E(t)) + j(t) - \dot{x}^+ H^+(\sigma) - \dot{x}^- H^-(\sigma) \quad (2)$$

$\rho c \frac{\partial T}{\partial t}$ is the temperature-dependent change in internal energy with respect to time, and $\lambda \frac{\partial^2 T}{\partial x^2}$ is the conductive heat flux along the length of the wire element. The terms in the RHS of Eq (1) and Eq (2) represent the gain or loss of thermal energy in the material where $-k(T - T_E(t))$ is the convective cooling with the environment, $j(t)$ is the addition of Joule heating for actuation, and $\dot{x}^+ H^+(\sigma)$ and $\dot{x}^- H^-(\sigma)$ are the addition/loss of stress dependent latent heats occurring with martensitic+ and martensitic- phase transformations respectively. The kinetics of the phase transformation result from transitions between the martensitic and austenitic variants that are dictated by statistical thermodynamics using

$$\dot{x}^+ = -\dot{x}^+ p^{+A} + \dot{x}^A p^{A+} \quad (3)$$

$$\dot{x}^- = -\dot{x}^- p^{-A} + \dot{x}^A p^{A-} \quad (4)$$

where \dot{x}^+ is the rate of transformation for martensite+ and \dot{x}^- is the rate of transformation for martensite-. They are calculated by multiplying x^+ , x^- , x^A , which are the current amounts of martensite+, martensite-, and austenite, respectively, by the phase transformation probabilities, $p^{\pm A}$ and $p^{A\pm}$. The phase transformation probability equations are given by

$$p^{\pm A}(\sigma, T) = \frac{1}{\tau} \frac{e^{-\frac{V_{LE}}{2E_M kT}(\sigma_M \mp \sigma)^2}}{\operatorname{erfc}\left[\sqrt{\frac{V_{LE}}{2E_M kT}}(\sigma_M \mp \sigma)\right]} \quad (5)$$

$$p^{A\pm}(\sigma, T) = \frac{1}{\tau} \frac{e^{-\frac{V_{LE}}{2E_A kT}(\sigma_A \mp \sigma)^2}}{\operatorname{erf}\left[\sqrt{\frac{V_{LE}}{2E_A kT}}(\sigma_A + \sigma)\right] + \operatorname{erf}\left[\sqrt{\frac{V_{LE}}{2E_A kT}}(\sigma_A - \sigma)\right]} \quad (6)$$

where $p^{\pm A}$ is the probability of transforming from either martensite+ or – to austenite and $p^{A\pm}$ is the probability of transforming from austenite to either martensite+ or –. $1/\tau$ is the fluctuation frequency of the lattice layers, V_{LE} is the volume of a lattice element, k is the Boltzmann constant, and E_M and E_A are the elastic modulus of martensite and austenite, respectively. σ_M and σ_A are the transformation stress at which a phase transformation begins from martensite to austenite and from austenite to martensite, respectively. The probabilities are calculated using equations from Boltzmann principles of statistical thermodynamics and are dependent on the current temperature, T , and the macroscopic stress, σ , in the wire. The stress is determined from the stress-strain equation

$$\sigma(\varepsilon) = \frac{E_M(\varepsilon - (x^+ - x^-)\varepsilon_T)}{x^+ + x^- + \frac{E_M}{E_A}(1 + x^+ + x^-)} \quad (7)$$

where σ is the macroscopic stress calculated from the macroscopic strain ε . The phase fraction and elastic moduli terms on the RHS of Eq (6) are calculated using ε and the transformation strain ε_T . The equations explained above are implemented into ABAQUS via the UMAT option. During a simulation, ABAQUS passes a new strain increment and

updated state dependent variables (SDVs) of phase fractions and wire temperature to the SMA model. The new phase fractions and wire temperature are solved via the RADAU5 integration scheme, and are subsequently used to calculate the macroscopic strain and stress in the wire. ABAQUS uses the SMA stress value in addition to the SMA tangent modulus in order to complete the global stiffness matrix and solve the global displacement matrix using the Newton-Raphson iteration method. The SMA's tangent modulus is given by

$$\frac{d\sigma}{d\varepsilon} = \frac{\partial\sigma}{\partial\varepsilon} + \frac{\partial\sigma}{\partial x^+} \frac{dx^+}{d\varepsilon} + \frac{\partial\sigma}{\partial x^-} \frac{dx^-}{d\varepsilon} \quad (8)$$

$$\frac{\partial\sigma}{\partial\varepsilon} = \frac{E_M}{x^+ + x^- + \frac{E_M}{E_A}(1 - x^+ - x^-)} \quad (9)$$

$$\frac{\partial\sigma}{\partial x^+} = \frac{(-E_M \varepsilon_T) \left(x^+ + x^- + \frac{E_M}{E_A}(1 - x^+ - x^-) \right) - \left(1 - \frac{E_M}{E_A} \right) \left(E_M (\varepsilon - (x^+ - x^-) \varepsilon_T) \right)}{\left(x^+ + x^- + \frac{E_M}{E_A}(1 - x^- - x^+) \right)^2} \quad (10)$$

$$\frac{\partial\sigma}{\partial x^-} = \frac{(E_M \varepsilon_T) \left(x^+ + x^- + \frac{E_M}{E_A}(1 - x^+ - x^-) \right) - \left(1 - \frac{E_M}{E_A} \right) \left(E_M (\varepsilon - (x^+ - x^-) \varepsilon_T) \right)}{\left(x^+ + x^- + \frac{E_M}{E_A}(1 - x^- - x^+) \right)^2} \quad (11)$$

The SMA material properties and state dependent variables are used with the equations above and implemented into a finite element user material subroutine to simulate adaptive structures actuated by SMA wires.

2.3 FEA Implementation

The SMA model described above is able to determine the behavior of an SMA wire through controlled head inputs and loads in finite element simulations. The commercially available finite element software ABAQUS was chosen to simulate the adaptive structure for its user material (UMAT) option, which allows the user to implement their own model. The UMAT subroutine is capable of calculating nonlinear and hysteretic materials which is necessary to describe SMA material behavior. The code we implemented in UMAT solves for the tangent modulus, stress, and the state dependent variables of phase fractions and temperature. The outline for simulating a multi-wire adaptive structure is illustrated in Figure 2.

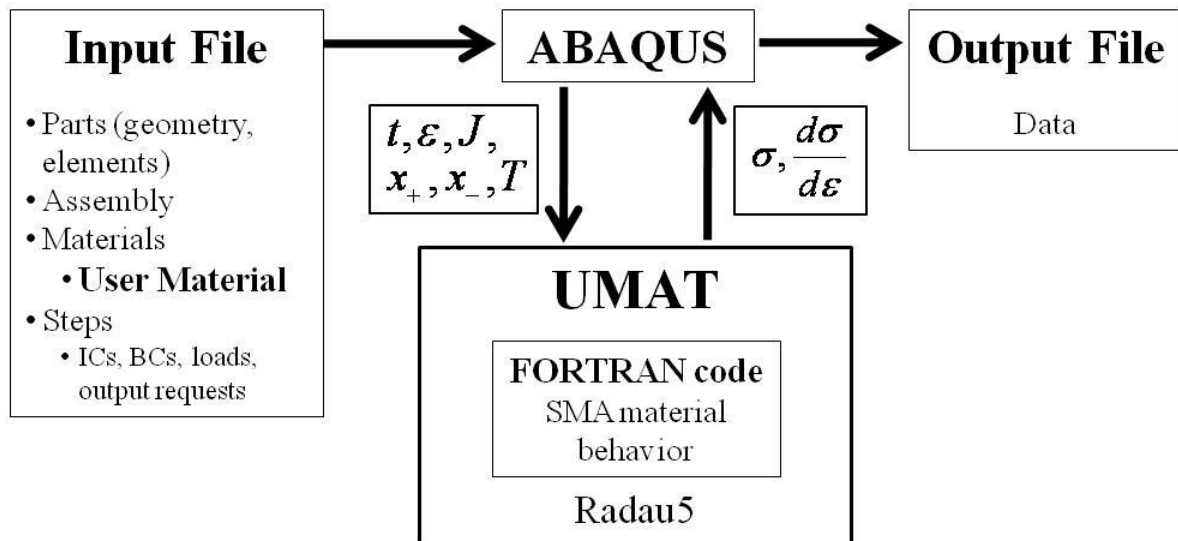


Figure 2: Flow of Analysis.

The first step in the simulation is to submit the input file to ABAQUS. The input file contains information about the part geometries, assemblies, material properties, and the loading steps

to be performed in the analysis. For a simulation with multiple SMA wires, each SMA wire is modeled as a separate part with a different material name, thus enabling the wires to share one UMAT subroutine with the same SMA model. Different material names also allow for each wire to have their own initial conditions, SDVs, and material properties. Joule heating information for all simulations is communicated to the SMA model via a list of amplitudes and actuation times in the material properties list (PROPS) for each wire.

Within each time step and iteration, ABAQUS solves for the local and global displacements and calls the SMA material code via the UMAT subroutine. The SMA wires' SDVs and strain increments are communicated to the FORTRAN code for every time increment. The FORTRAN code uses these inputs to calculate the SMA behavior based on the model from Section 2.2 and returns the stress and tangent modulus to ABAQUS along with the updated SDV values.

Chapter 3

Simulations

In order to thoroughly validate the SMA model, simulations within two different groups are performed. The first group of simulations are conducted under homogenous temperature profiles, where the heat flux equilibrium equations are solved within the SMA UMAT code using the energy balance equation from Eq (1) in Chapter 2 and independently of ABAQUS. The second group of simulations are conducted for inhomogeneous temperature profiles, where the heat flux equilibrium equations are solved at the structural level in ABAQUS.

3.1 Homogenous Temperature Profiles

All of the simulations conducted under homogenous temperature profiles use three-dimensional, two-node truss elements (T3D2) to model the SMA wires. T3D2 elements only exhibit axial stress and strain degrees of freedom which is characteristic of wire behavior. The temperature of the SMA wires is solved within the UMAT subroutine and incorporated into the simulation through a state dependent variable. Thus, the boundary conditions at the end of the SMA wires are considered as adiabatic.

3.1.1 Simulation 1: SMA Wire Initial Testing

3.1.1.1 Geometry and Parameters

In order to validate the SMA model's behavior without actuation, a single SMA wire was first tested under mechanical loading and unloading conditions at five different temperatures. In this initial simulation, a SMA wire of length 0.05m and radius 25.0e-6m is modeled using a single three-dimensional, two-node truss element (T3D2) shown in Figure 3. The top of the SMA wire, SMA Node 2, is fixed in displacement and rotation and a concentrated load of magnitude 3.25N is applied to the bottom of the SMA wire, SMA Node 1, in the negative Y direction. The concentrated load is gradually applied for 10 seconds before being gradually released. The results for the simulation at a temperature of 273K are illustrated in Figure 4 below.

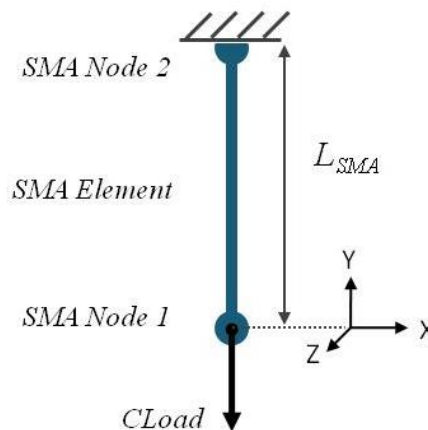
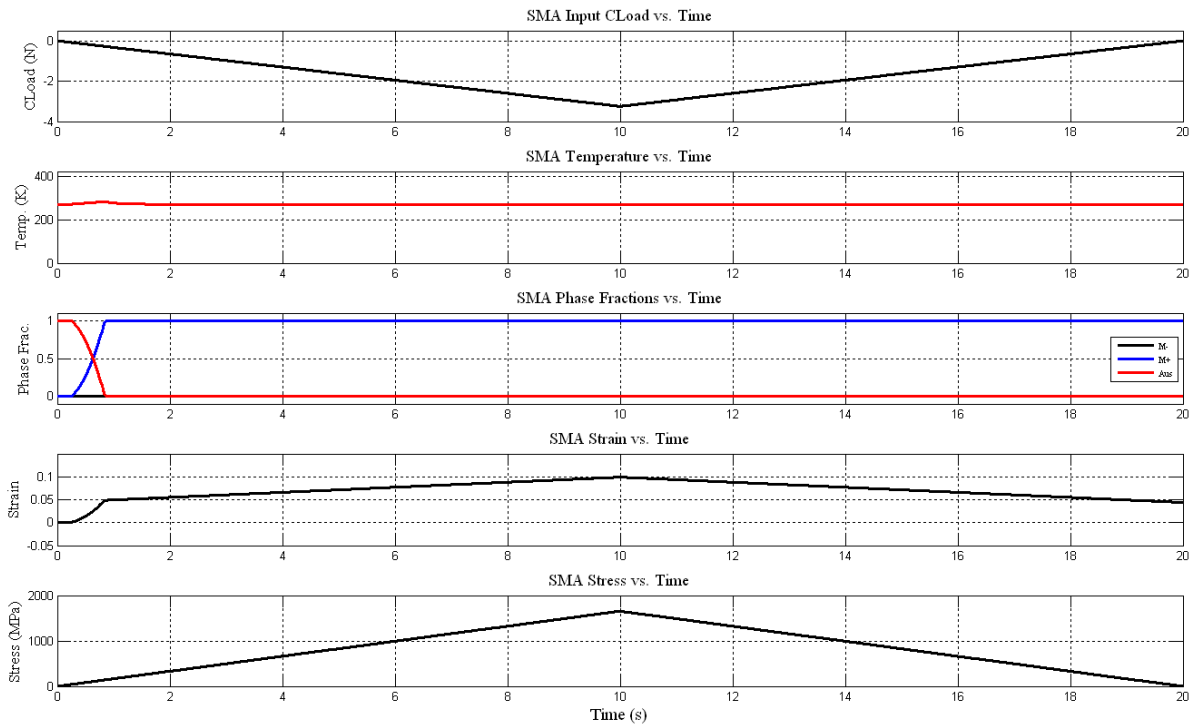


Figure 3: Simulation 1 schematic: SMA wire initial testing.

Table 1: Simulation 1: Initial Conditions and Model Parameters.

Parameter	Variable	Value
SMA radius	r_{SMA}	25.0e-6 m
SMA length	L_{SMA}	0.05 m
Martensite +	M+	0%
Martensite -	M-	0%
Pre-stress	σ_o	0.0 MPa
External Temperature	T_{ext}	273.0 K

3.1.1.2 Results

**Figure 4:** Time resolved concentrated load input to SMA wire and corresponding phase fractions, strain and stress responses at $T=273K$.

The first graph of Figure 4 plots the concentrated load, which causes changes in the SMA wire's temperature, phase fractions, strain and stress in the following graphs. When the concentrated load is applied from $t=0$ to 10s, the SMA wire experiences a superelastic phase transformation from 100% austenite to 100% martensite+. During this transformation, latent heating occurs inside the wire and its effects are visible in the temperature versus time graph as a small wave occurring at $t=0.75$ s. The change to 100% martensite+ causes a direct increase in the wire's strain from 0.0% to 9.917% and results in a displacement of 4.959mm in the negative Y direction, which is graphed in Figure 5a. The stress-strain relationship from Eq (7) causes the wire to reach a maximum stress value of 1655.0 MPa. When the concentrated load is gradually released from $t=10$ to 20s the wire remains in 100% martensite+, the strain decreases to 4.4% and the stress decreases to 0.0 MPa, leaving the wire in a quasiplastic state. From here, the SMA wire will only return to 100% austenite if an external heat is applied.

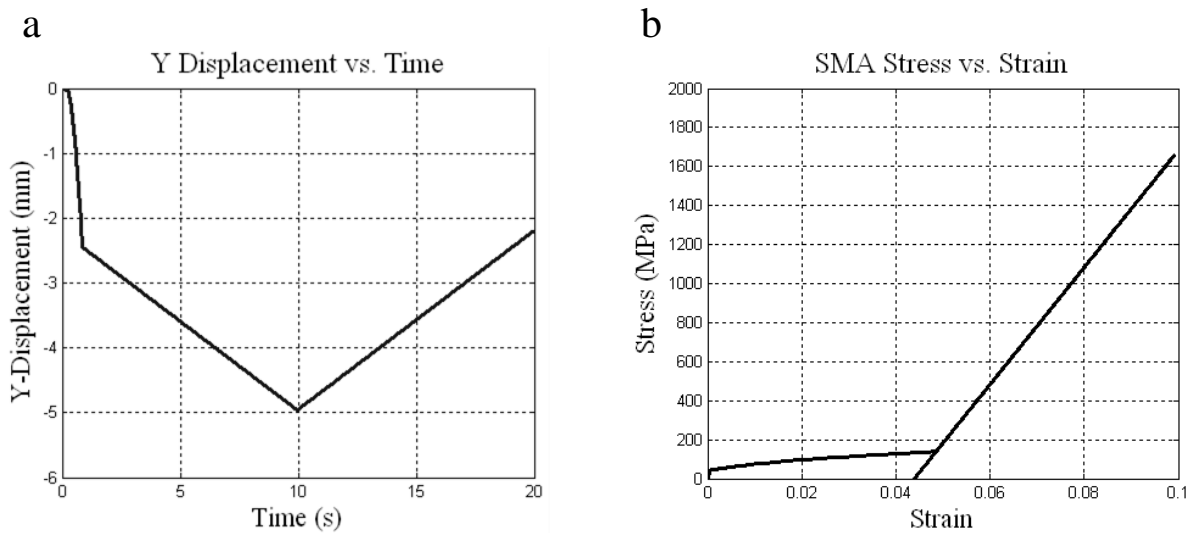


Figure 5: (a) Displacement versus time response and (b) stress versus strain relationship at $T=273$ K.

The same simulation was then conducted at temperatures of 300K, 350K, 400K, and 450K.

The resulting stress versus strain relationship for each temperature case is compared in Figure 6 below.

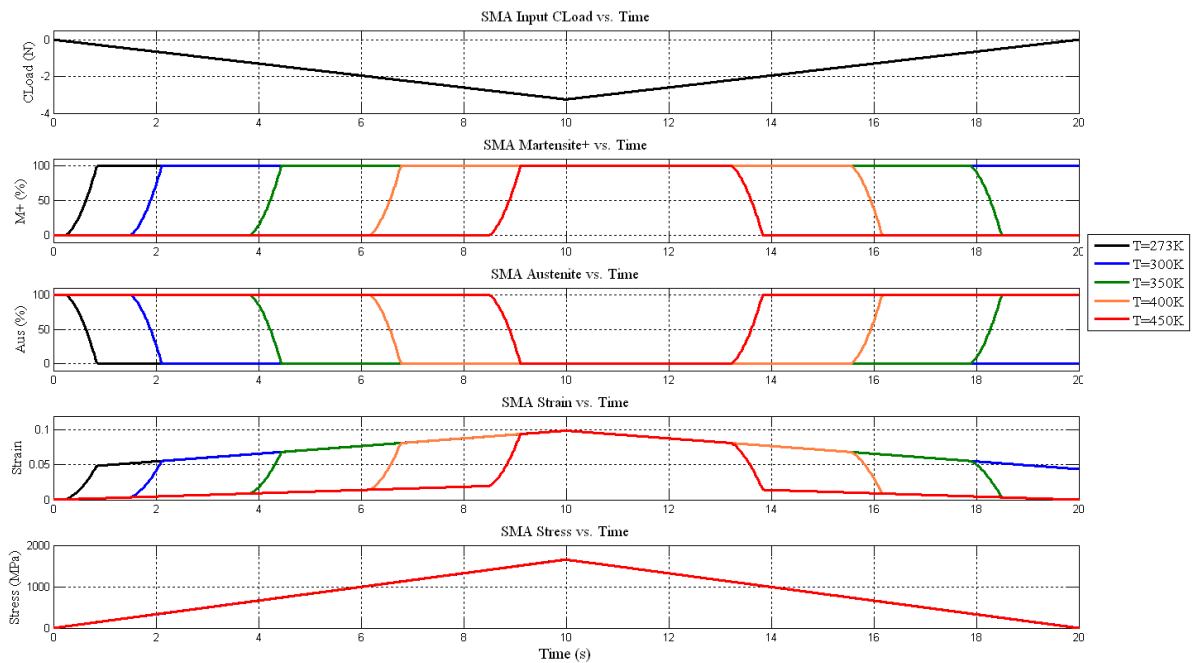


Figure 6: Time resolved concentrated load input to SMA wire and corresponding phase fractions, strain and stress responses at $T=273\text{K}$, 300K , 350K , 400K , and 450K .

The first graph of Figure 6 plots the concentrated load which causes changes in the SMA wire's temperature, phase fractions, strain and stress for all temperatures in the following graphs. When the concentrated load is applied from $t=0$ to 10s , the SMA wires at all temperatures experience a superelastic phase transformation from 100% austenite to 100% martensite+, however the time of the transformation is dependent on the external temperature. The wires at higher temperatures take longer to transform to 100% martensite+

than the wires at lower temperatures. The change to 100% martensite+ causes a direct increase in the wires' strain from 0.0% to 9.917% and results in a displacement of 4.959mm in the negative Y direction, which is graphed in Figure 7a. The stress-strain relationship from Eq (7) causes the wires to reach a maximum stress value of 1655.0 MPa. When the concentrated load is gradually released from $t=10$ to 20s the wires remain in 100% martensite+, the strain decreases to 4.4% and the stress decreases to 0.0 MPa, leaving the wires in a quasiplastic state. From here, the SMA wires will only return back to 100% austenite if an external heat is applied.

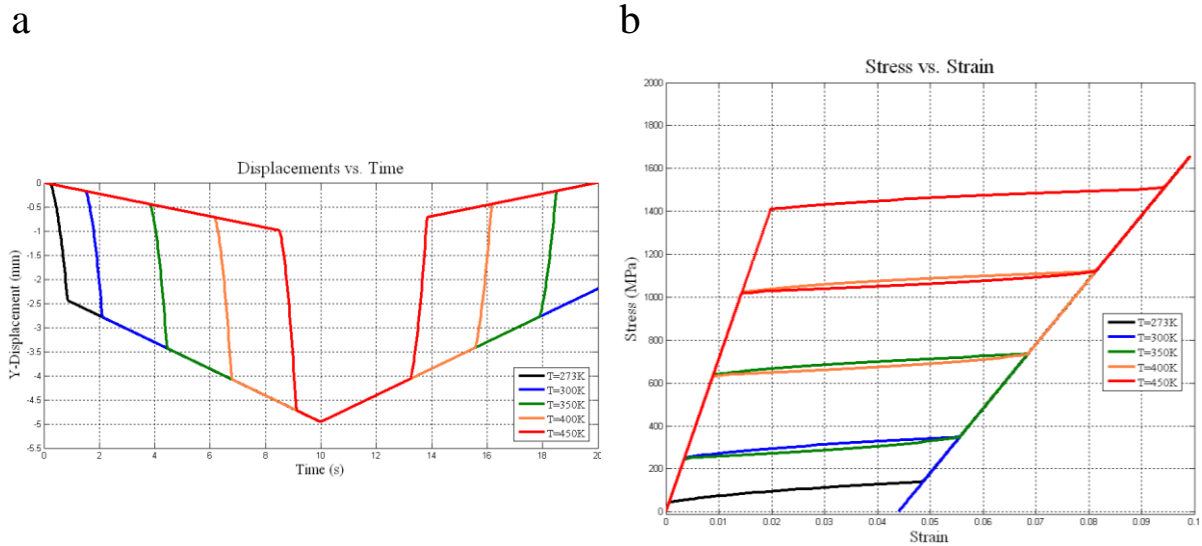


Figure 7: (a) Displacement versus time response and (b) stress versus strain relationship at $T=273\text{K}$, 300K , 350K , 400K , and 450K .

The SMA model shows hysteresis for loading and unloading cases at different temperatures without actuation. In order to further validate the accuracy of the model described above and to illustrate its capabilities, a variety of simulations were conducted with each one increasing

in complexity. The second simulation performed under homogeneous temperature profiles consists of a SMA wire under a concentrated load with actuation. Next, simulations of an SMA wire coupled with a 3-D elastic beams and a simulation of multiple SMA wires implemented in an adaptive structure are also explained under homogenous temperature profiles.

3.1.2 Simulation 2: SMA Wire with Concentrated Load

The SMA model described in Chapter 2 was first implemented into a series of simulations with homogeneous temperature, phase fraction, strain and stress profiles. This second simulation performed consists of a single SMA wire cyclically actuated under a concentrated load. This simulation illustrates the model's ability to predict SMA wire behavior with actuation.

3.1.2.1 Geometry and Parameters

A SMA wire of length 0.05m and radius 25.0e-6m is modeled using a single three-dimensional, two-node truss element (T3D2) shown in Figure 8. The top of the SMA wire, SMA Node 2, is fixed in displacement and rotation and a concentrated load of magnitude 1.0N is applied to the bottom of the SMA wire, SMA Node 1, in the negative Y direction and held constant for the entire simulation. Power is cyclically supplied to the wire in the form of Joule heating in a triangular waveform with an amplitude of 0.3 Watts for 5 cycles to actuate

the SMA wire. The initial conditions and model parameters for the simulation are listed in Table 2 and the results from the simulation are explained in Figures 9-11 in the Results section below.

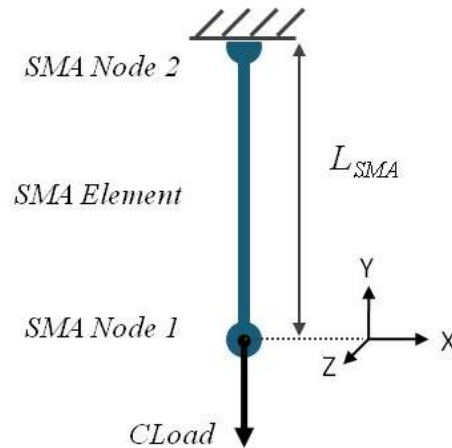


Figure 8: Simulation 2 Schematic: SMA wire with a concentrated load and actuation.

Table 2: Simulation 2: Initial Conditions and Model Parameters.

Parameter	Variable	Value
SMA radius	r_{SMA}	25.0e-6 m
SMA length	L_{SMA}	0.05 m
Martensite +	M+	50%
Martensite -	M-	50%
Pre-stress	σ_o	0.0 MPa
External Temperature	T_{ext}	273.0 K

3.1.1.2 Results

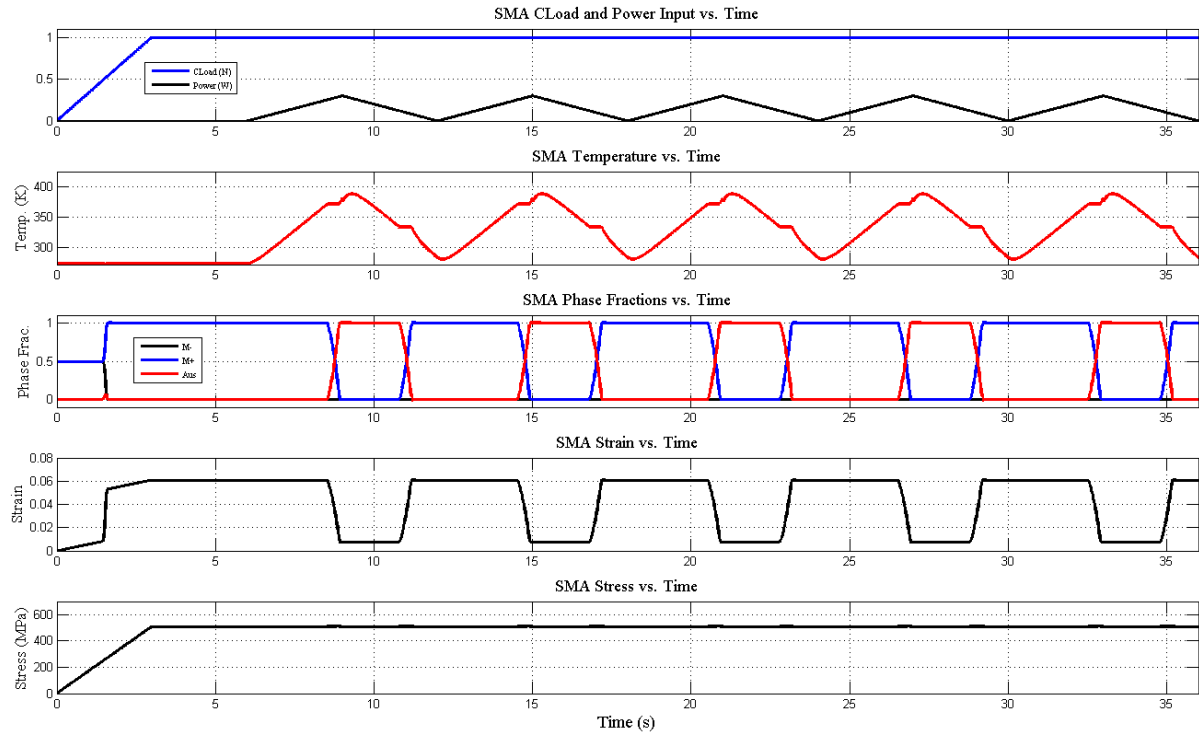


Figure 9: Time resolved concentrated load and power input to SMA actuator and corresponding temperature, phase fractions, strain and stress responses.

The concentrated load and joule heating cycles applied to the SMA are shown in the first graph of Figure 9. These inputs result in changes to the SMA wire's temperature, phase fractions, strain and stress which are also shown in Figure 9 below the input graph. When the concentrated load is applied from $t=0$ to 3s, the SMA wire experiences a superelastic phase transformation from 50% martensite⁺ and 50% martensite⁻ to 100% martensite⁺. The change to 100% martensite⁺ causes a direct increase in the wire's strain from 0.0% to 6.10% and results in a displacement of 3.049mm in the negative Y direction, which is graphed in Figure 10. The stress-strain relationship from Eq (7) causes the wire to reach a maximum

stress value of 509.3 MPa. When power is applied to the SMA wire from $t=6$ to 9s in the first graph it causes the internal temperature of the SMA to rise. When the internal temperature rises above the martensite to austenite transformation temperature, the wire begins to transform from 100% martensite+ and, in this simulation, completely transforms to 100% austenite. Latent heating occurs inside the wire during this transformation and its effects are visible in the temperature versus time graph as a small wave occurring at $t=8$ s. The change in phase fractions also causes a direct decrease in strain from 6.10% to 0.72%, which in turn causes a change in displacement of 2.69mm in the positive Y direction. When the joule heating is gradually released from $t=9$ to 12s, the temperature of the wire also decreases and drops below the austenite to martensite transformation temperature. At this temperature, the wires begin transforming back to martensite+. Latent heats of transformation also occur during this transformation and are visible in the temperature versus time graph as a small wave occurring at $t=11$ s. The concentrated load continuously applied to the end of the wire causes the phase fractions of the SMA wire return to 100% martensite+ from 100% austenite, which causes the strain to increase from 0.72% to 6.10%. The same sequence of wire transformation occurs for the next 4 joule heating cycles. The SMA stress versus strain and strain versus temperature responses are graphed in Figure 11.

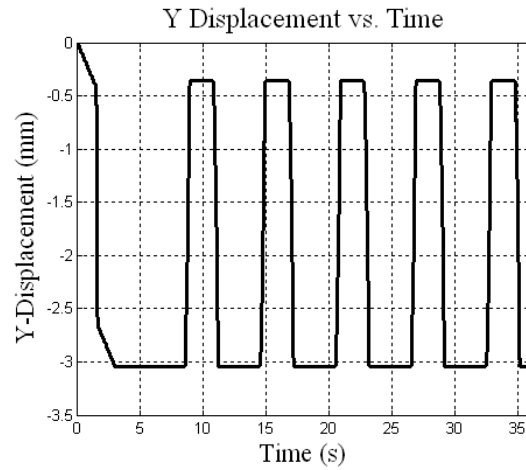


Figure 10: SMA wire tip displacement versus time response.

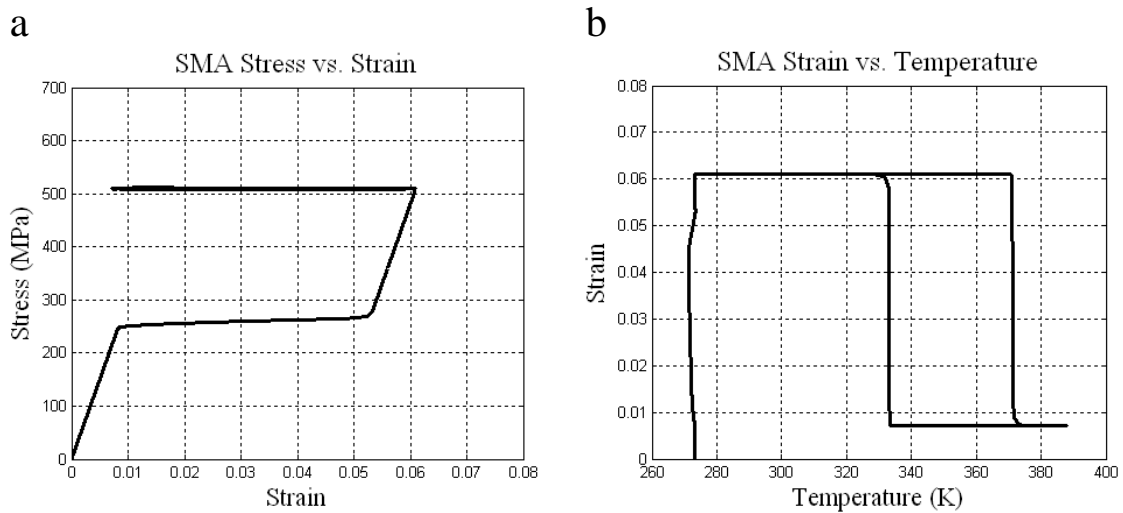


Figure 11: (a) Stress versus strain and (b) strain versus temperature relationships.

This simulation illustrates the behavior of a single SMA wire cyclically actuated under a concentrated load. The SMA temperature, phase fractions, strain, stress and displacement were graphed and analyzed for the SMA wire versus time for 5 cycles of actuation. The stress versus strain and the strain versus temperature plots were also observed.

Additional simulations involving an SMA wire under initial stress and coupled with a stiff spring with actuation were also performed. These simulations are included in Appendix A and Appendix B.

3.1.3 Simulation 3: SMA Wire and Elastic Beam

The third simulation performed also implements the same SMA model described in Eq (1) of Chapter 2 for an SMA wire with a homogeneous temperature profile. This simulation increases in complexity by coupling the SMA wire with a stiff, 3-D elastic beam structure and observing the effects of wire actuation. The resulting temperature, phase fractions, strain, stress, and displacements are investigated versus time.

3.1.3.1 Geometry and Parameters

In this simulation, a SMA wire is coupled with a stiff, 3-D elastic beam and actuated with joule heating. The SMA wire has a length of 0.05m, a radius 25.0e-6m and is modeled using a single three-dimensional, two-node truss element (T3D2) shown in Figure 12. The elastic beam has a length of 0.01m, a circular cross-section with a radius of 0.001m and is modeled using 20 three-dimensional beam elements (B31). The top of the SMA wire, SMA Node 2, is fixed in displacement and rotation and the bottom of the SMA wire, SMA Node 1, is connected to the left end of the beam, Beam Node 1, via a multi-point constrain in the form

of a tie. The right end of the beam, Beam Node 21, is fixed in displacement and rotation. Power is cyclically supplied to the wire in the form of Joule heating in a triangular waveform with an amplitude of 0.64 Watts for 5 cycles to actuate the SMA wire. The initial conditions and model parameters for the simulation are listed in Table 3 and the results from the simulation are explained in Figures 13-15 in the Results section below.

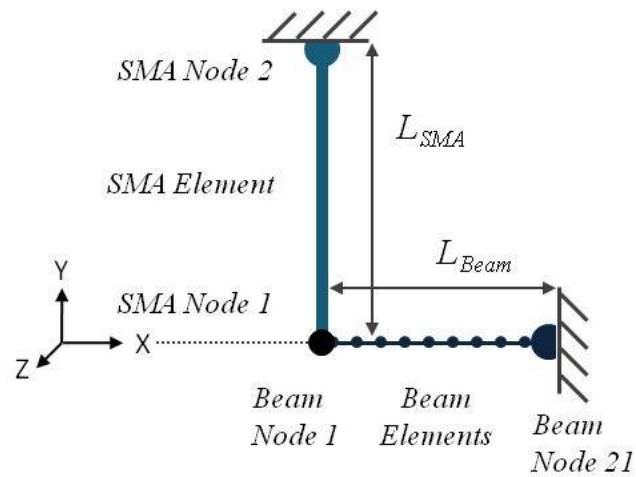


Figure 12: Simulation 3 schematic: SMA wire coupled with a 3-D elastic beam and actuation.

Table 3: Simulation 3: Initial Conditions and Model Parameters.

Parameter	Variable	Value
Beam radius	r_{Beam}	0.01m
Beam length	L_{Beam}	0.001m
Beam Elastic Modulus	E_{Beam}	1000MPa
Beam Poisson's Ratio	ν	0.3
SMA radius	r_{SMA}	25.0e-6 m
SMA length	L_{SMA}	0.05 m
Initial Condition: Martensite+	M_{+o}	100%
Initial Condition: Martensite-	M_{-o}	0%
Initial Condition: Pre-stress	σ_o	0.0 MPa
External Temperature	T_{ext}	273.0 K

3.1.3.2 Results

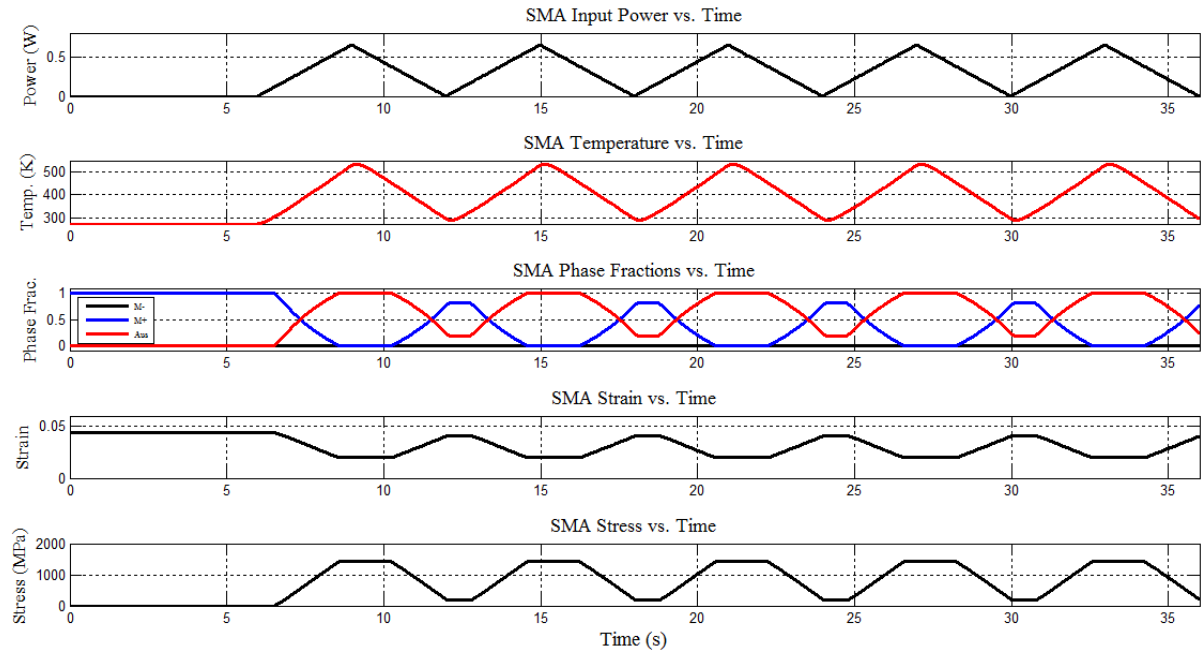


Figure 13: Time resolved power input to SMA actuator and corresponding temperature, phase fractions, strain and stress responses.

The SMA wire is initially in 100% martensite+ with 4.4% strain (0.0 MPa of pre-stress). As power is applied to the SMA wire in the first graph, changes in the SMA wire temperature, phase fractions, strain, and stress occur in the following graphs versus time. When the wire is heated to 0.64W from $t=6$ to 9s in the first graph is causes the internal temperature of the SMA to rise to 529K. When the internal temperature rises above the martensite to austenite transformation temperature, the wire begins to transform from 100% martensite+ and, in this simulation, transforms completely to austenite. The change in phase fractions causes a direct decrease in strain from 4.4% to 1.99%, which in turn causes a change in displacement of 1.205mm in the positive Y direction as shown in Figure 14. In addition, the stress-strain

relationship from Eq (7) causes the wires to reach a maximum stress value of 1415 MPa. When the joule heating is gradually released from $t=9$ to 12s, the temperature of the wire also decreases and drops below the austenite to martensite transformation temperature. At this temperature, the wire begins transforming back to martensite+. The external restoring force from the elastic beam also assists in wire transformation back to martensite+. The phase fractions at the end of transformation are 81.54% martensite+ and 18.46% austenite, which correspond to a strain value of 4.104% and a stress value of 173.6MPa. When power is supplied to the SMA wire at $t=12$ s for the next joule heating cycles the same sequence of wire heating and transformation occurs. The SMA stress versus strain and strain versus temperature responses are graphed in Figure 15.

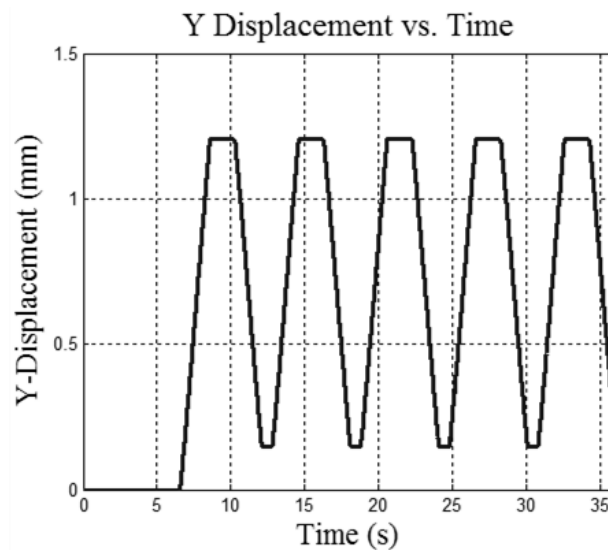


Figure 14: SMA wire tip displacement versus time response.

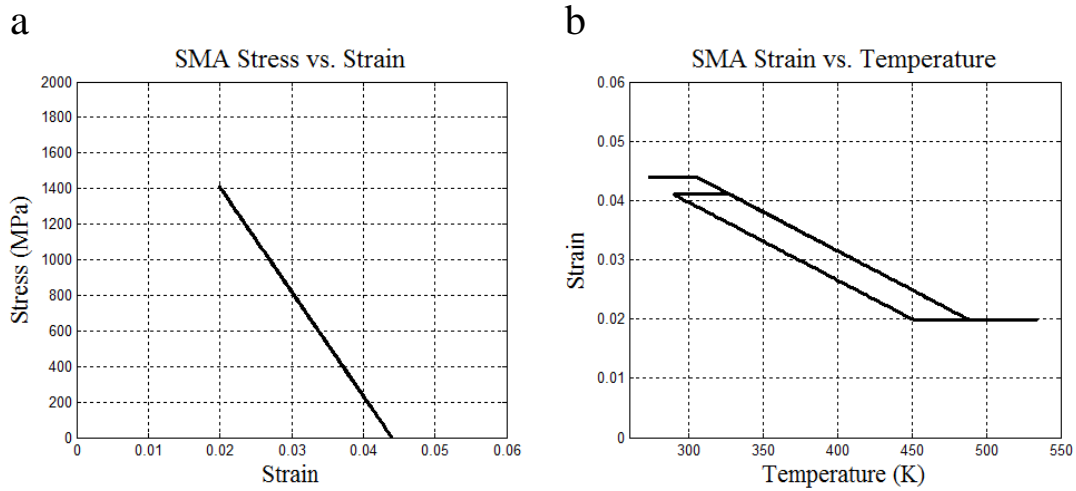


Figure 15: (a) Stress versus strain and (b) strain versus temperature relationships.

Additional tests were also performed by varying the elastic modulus of the 3-D beam. The same simulation was analyzed with the beam's elastic modulus equal to 2000MPa, 500MPa, 250MPa, and 125MPa. The effects of different elastic modulus values are shown in Figure 16.

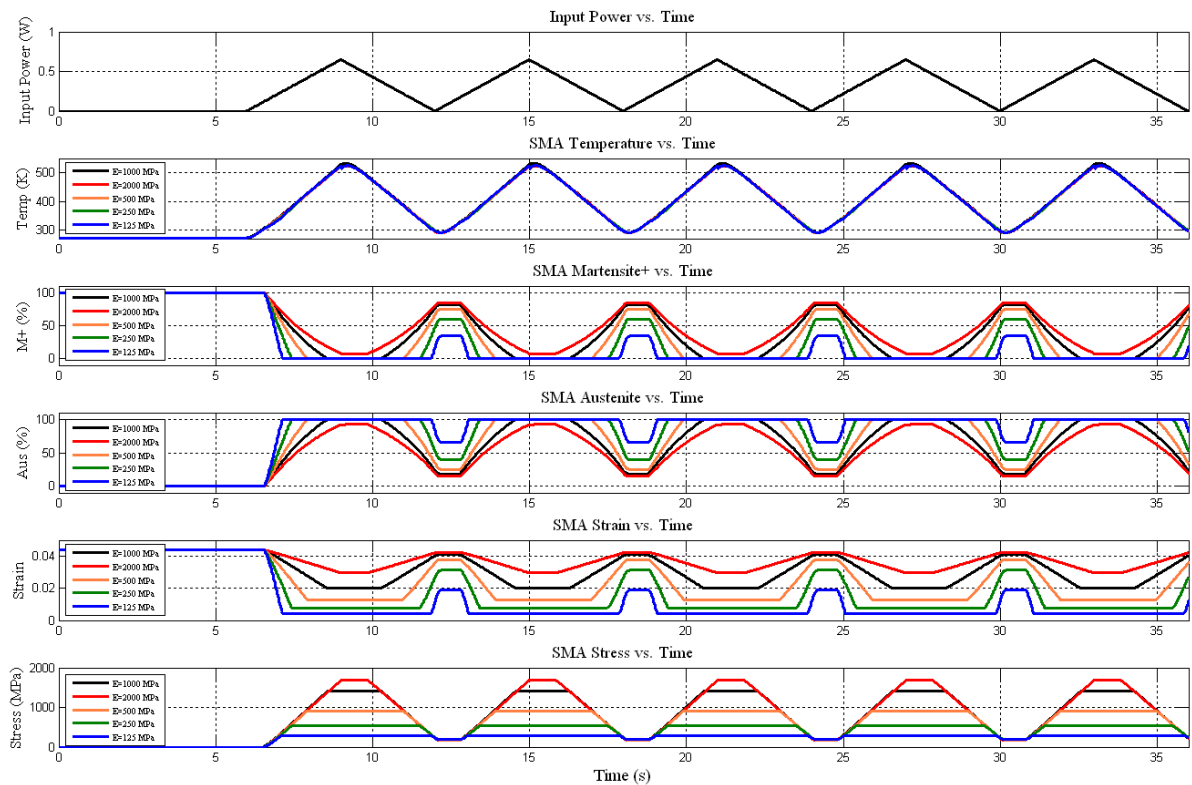


Figure 16: Time resolved power input to SMA actuator and corresponding temperature, phase fractions, strain and stress responses for different beam stiffness values.

All of the SMA wires are initially in 100% martensite+ with 4.4% strain (0.0 MPa of pre-stress). As power is applied to the SMA wires in the first graph of Figure 16, changes in temperature, phase fractions, strain, and stress occur and are also graphed versus time. When the wire is heated to 0.64W from $t=6$ to 9s in the first graph is causes the internal temperature of all of the SMA wires to rise to the same value. When the internal temperature rises above the martensite to austenite transformation temperature, the wires begin to transform from 100% martensite+ and settle at different amounts of austenite and martensite+, depending on the stiffness of the beam. Beams with larger stiffness values result in less transformation to austenite than beams with smaller stiffness values. The amount of martensite+ and austenite

in the wire results in different values of SMA wire strain and stress. This also affects the displacement of the SMA wire end, as shown in Figure 17. When the power is gradually released from the wires, each transforms at a different rate and settles at different values of phase fraction, strain, and stress due to the different beam stiffness's.

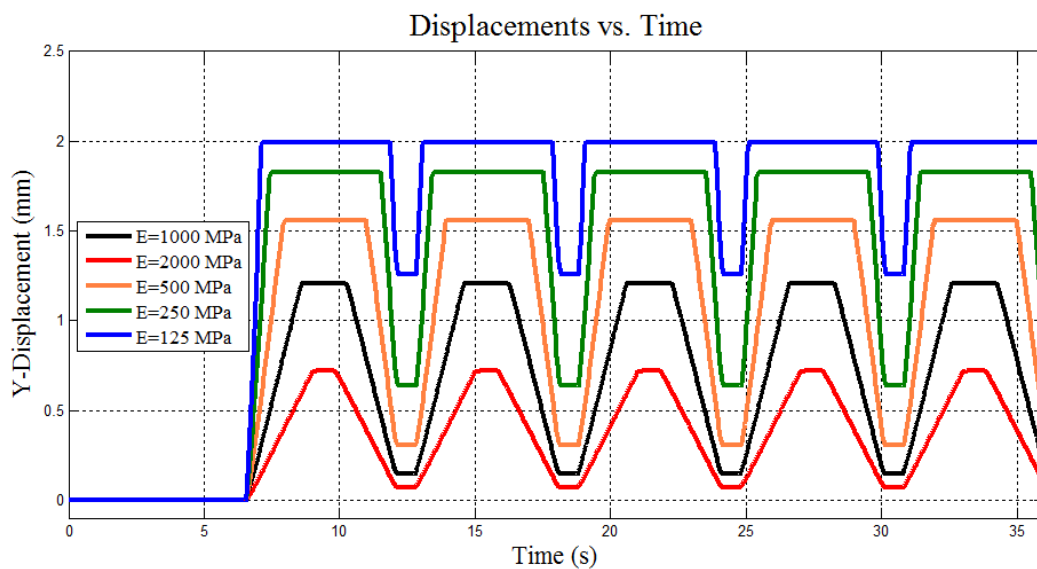


Figure 17: SMA wire tip displacement versus time response for different beam stiffness values.

This simulation illustrates the behavior of a single SMA wire coupled with an elastic beam and cyclically actuated. The SMA temperature, phase fractions, strain, stress and displacement were graphed and analyzed for the SMA wire versus time for 5 cycles of actuation. The stress versus strain and the strain versus temperature plots were also observed. Simulations where the SMA wire was coupled with elastic beams of varying stiffness were also conducted, showing that the SMA model is able to predict SMA wire behavior when a SMA is coupled with a 3-D elastic structure.

3.1.4 Simulation 4: Adaptive Nozzle in Smart Inhaler

This next simulation also uses the SMA model described in Chapter 2 for homogeneous temperature, phase fraction, strain and stress profiles along the SMA wire. For this simulation, an analysis was performed using multiple SMA wires attached to a three-dimensional solid structure. The simulation was conducted according to an experiment performed in the laboratory and the results of the simulation were compared against those of the actual prototype.

3.1.4.1 Adaptive Nozzle Overview

The adaptive nozzle is the main component of the smart inhaler system developed by researchers at North Carolina State University [25]. The smart inhaler, motivated by Kleinstreuer and Zhang [26] and Roberts and Kleinstreuer [27], is a targeted drug delivery device that has the ability to inject aerosol particles from a controlled release position such that they are transported to precise locations within the human respiratory system. This technology has potential for use in lung cancer treatment because medication can be sent directly to the tumor site. An SMA-actuated adaptive nozzle is designed to provide a controlled release position; and a prototype has been built and described in [28]. Simulating the adaptive nozzle using FE analysis will assist in predicting the nozzle's behavior and further validate the overall performance of the device while reducing the amount of time and money required to build physical prototypes.

The purpose of this simulation is to record the adaptive nozzle tip's trajectory under different wire actuation sequences and to monitor the change in temperature, phase fraction, strain and stress inside each SMA wire. In order to provide controlled drug delivery, the nozzle tip must remain parallel with the air flow. By actuating the wires in pairs, a sigmoidal nozzle shape is obtained (Figure 21b) and the nozzle tip will correctly release the aerosol particles.

Subsection 3.1.4.2 explains the geometry and assembly of the adaptive nozzle.

3.1.4.2 Geometry and Assembly

The adaptive nozzle used in the simulation was modeled in ABAQUS according to the geometry of the actual prototype. Figures 18a, b, c show both the Adaptive Nozzle Prototype, FEA Model of the Adaptive Nozzle, and schematics of the SMA wire orientation around the nozzle.

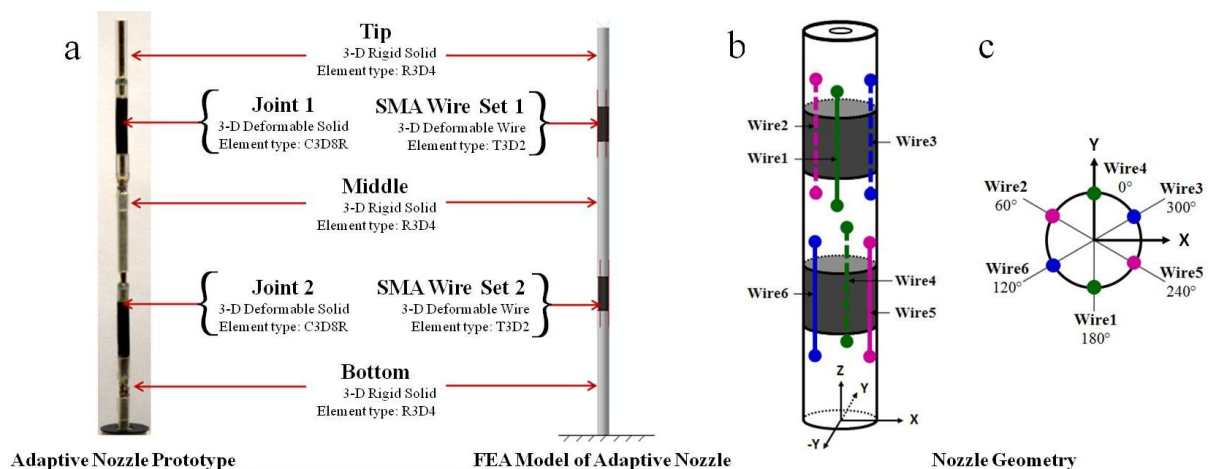


Figure 18: (a) Adaptive nozzle prototype and FEA model. (b), (c) Adaptive nozzle geometry and SMA wire attachment.

The adaptive nozzle in Figure 18 is composed of three solid parts, two flexible joints, and six SMA wires equally spaced around the two joints. The nozzle's bottom, middle and tip, which do not experience any deformation, are modeled as 3-D rigid parts using R3D4 elements in ABAQUS. The elastic joints are modeled as 3-D solid deformable parts using C3D8R elements. Each of the six SMA wires is modeled as a 3-D part using a single T3D2 truss element. Table 4 lists the geometrical properties of each part along with their element type.

Table 4: Simulation 4: Geometric Data.

Part	Length	Diameter	Element Type
Nozzle Tip	22.225mm	3.175mm	R3D4
Nozzle Middle	38.100mm	3.175mm	R3D4
Nozzle Bottom	34.925mm	3.175mm	R3D4
Joints 1, 2	9.525mm	3.175mm	C3D8R
SMA Wires 1-6	19.05mm	50.0e-3mm	T3D2

The bottom of the nozzle is fixed in displacement and rotation. The top and bottom surfaces of each joint are tied in displacement and rotation to the rigid parts. The end of each wire is tied to a point on a rigid part via a multi-point constraint (MPC) in the form of a tie. In order to maintain the sigmoidal shape described in Subsection 3.1.4.1, the SMA wires must be actuated in pairs. In addition, each pair must have one wire 180 degrees across from its partner and it must be located on the opposite nozzle joint, as illustrated in Figure 18. The three pairs of wires are: wires 1 & 4, 2 & 5, and 3 & 6. The wires will be actuated in these pairs for the entire simulation.

3.1.4.3 Simulation Parameters

The initial position of the nozzle is axially aligned along the Z-axis with no deformation. The external temperature was set constant at a value of 293K. Each SMA wire is pre-stressed to 150.0 MPa which corresponds to 4.7% strain. Triangular waveforms of amplitudes of 0.11 watts of power (Joule heating) are applied for equal durations of time to each of the three sets of SMA wires at different time intervals. The SMA wire temperature, phase fractions, strain, and stress outputs are recorded along with the nozzle tip displacement. Material properties for the SMA actuators are based on typical NiTi data and can be found in Table 5.

Table 5: Simulation 4: Model Parameter List.

Parameter	Variable	Value
SMA wire density	ρ	6.4e+03 kg/m ³
Elastic modulus of martensite	E_M	71.1e+09 Pa
Elastic modulus of austenite	E_A	30.0e+09 Pa
Transformation strain	ε_T	0.044
Latent heats of phase transformation	H^+, H^-	154.0e+06 J/m ³
Low temperature for transformation		323.0 K
Transformation stress at low temperature		430.0e+06 Pa
High temperature for transformation		353.0 K
Transformation stress at high temperature		660.0e+06 Pa
Hysteresis width		295.0e+06 Pa
Relaxation time	τ	1.00e-02 1/s
Volume of a lattice element	V_{LE}	5.0e-23 m ³
Heat transfer coefficient	k	400.0 W/m ² K
Specific heat	c	836.0 J/kgK

3.1.4.4 Results

A typical simulation was performed over a period of 64 seconds. Each pair of wires was actuated before another wire pair was actuated. The initial round of heating from $t=0$ to 22s is only for the nozzle to stabilize, thus the cycles following the first cycle of actuation are analyzed. The SMA wire results from $t=21$ to 64 seconds are shown in Figure 19 below.

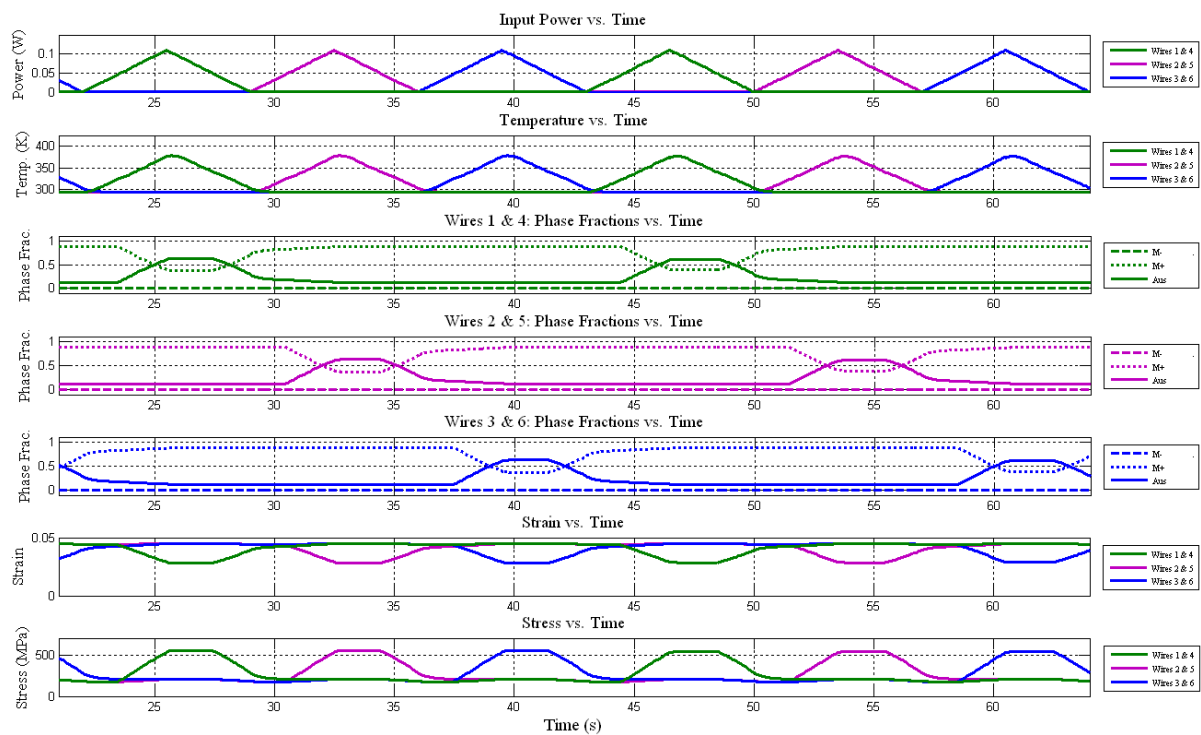


Figure 19: Time resolved power input to SMA actuators and corresponding temperature, phase fractions, strain and stress responses for $t=21-64s$.

The power applied to the wires in the first graph causes changes in the SMA wire temperature, phase fractions, strain, and stress in the following graphs versus time. When SMA wires 1 & 4 are heated to 0.11W from $t=22.0$ to 25.5s, their internal temperature increases and reaches 378K. When the temperature of the wires rises above the martensite to

austenite transformation temperature during heating, the wires begin transforming from 87.8% martensite+ and 12.2% austenite and, in this simulation, settle at 37.61% martensite+ and 62.39% austenite. The change in phase fractions causes a direct decrease in strain from 4.422% to 2.822%. The stress-strain relationship from Eq (7) causes the wires to reach a maximum stress value of 547.9 MPa. When the power is gradually removed from $t=25.5$ to 29s, the temperature of the SMA wires begins to decrease and during the process, drops below the austenite to martensite transformation temperature. At this temperature, the wires begin transforming back to martensite+. Their phase fractions at the end of transformation are 71.28% martensite+ and 28.72% austenite, which correspond to a strain value of 3.921% and a stress value of 282.4MPa. The wire temperature decreases with decreasing power until it reaches the external simulation temperature of 293K. When power is gradually supplied from $t=29$ to 32.5s to actuate SMA wires 2 & 5, the same sequence of wire heating and transformation occurs as in SMA wires 1 & 4. This is also true for the actuation of SMA wires 3 & 6 when power is supplied from $t=36$ to 39.5s.

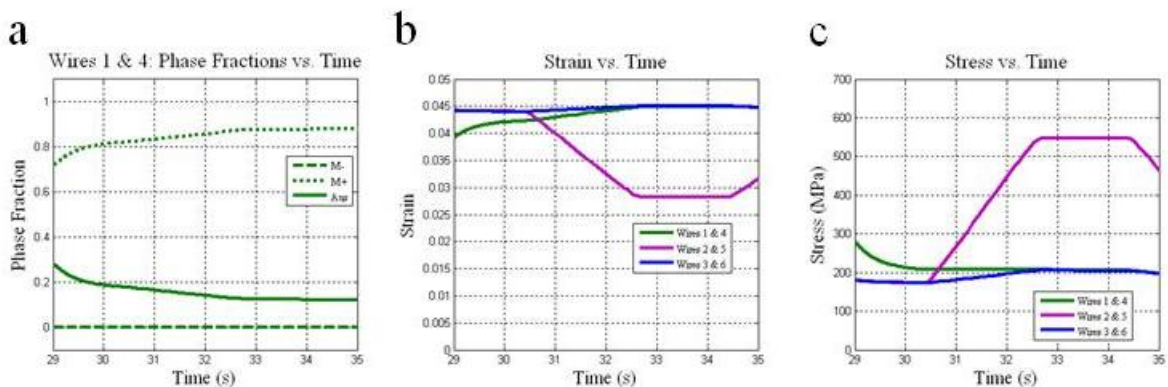


Figure 20: Multi-wire effects due to structural coupling. (a) Phase fractions versus time, (b) strain versus time, (c) stress versus time for $t=29-35s$.

In an adaptive structure with more than one SMA wire, second order effects can be observed in non-actuated wires due to wire coupling, as shown in Figure 20. Effects of wire coupling in the adaptive nozzle are best observed during the actuation of wires 2 & 5. After SMA wires 1 & 4 were actuated, they returned to 71.28% martensite+ and 28.72% austenite, and a strain value of 3.921%. In order to return to 87.8% martensite+, an external tensile force must be applied to the wires to increase their strain and cause a transformation favoring the martensite+ variant. When SMA wires 2 & 5 are actuated from $t=29$ to 36s, their decrease in strain causes additional tension to be applied to wires 1, 3, 4, & 6. As a result, wires 1 & 4 increase in strain from 3.921% to 4.494%, enough to transform them back into 87.78% M+ as seen in Figures 20a and 20b. In addition, due to the structure's geometry wires 3 & 6 albeit still in their 87.78% martensite+ state, are also elastically strained to 4.494%. This causes a stress increase in these wires of 205.1 MPa, as shown in Figure 20c.

The same types of secondary effects are seen in wires 2 & 5 when wires 3 & 6 are actuated. However, after wires 3 & 6 are actuated, they remain in 71.28% martensite+ and 28.72% austenite with 3.921% strain because there is no deformation to strain them back. The appearance of second order effects shows the model's ability to calculate coupling between the wires in a multi-wire adaptive structure.

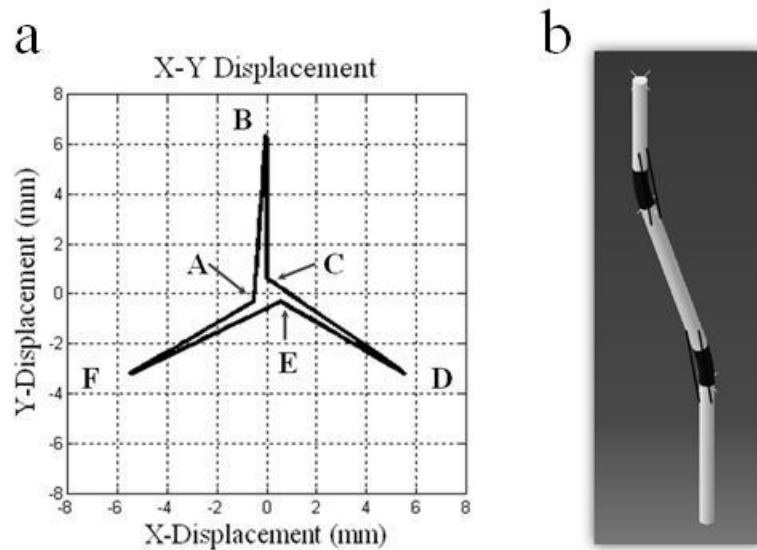


Figure 21: (a) Nozzle tip displacement. (b) Nozzle during actuation of wires 3 & 6.

A trajectory of the nozzle tip displacement is shown in Figure 21a and an intermediate, sigmoidal nozzle shape during deformation is shown in Figure 21b. The nozzle tip is initially in equilibrium at Point A. The actuation of wires 1 & 4 causes the nozzle to displace 6.4mm along the Y-axis to Point B. When the power decreases at $t=25.5s$, wires 1 & 4 relax and the nozzle tip moves from Point B to Point C. When SMA wires 2 & 5 are actuated at $t=29s$, the nozzle tip deforms from Point C to Point D. When power is released at $t=32.5s$, wires 2 & 5 relax and the nozzle tip moves from Point D to Point E. When wires 3 & 6 are actuated at $t=36s$, the nozzle tip moves from Point E to Point F. The nozzle tip is brought back to the origin, Point G, when power is released.

3.1.4.5 Comparison with Actual Data

The simulation results for the nozzle tip displacement in the X-Y plane were compared against results obtained from the prototype. The prototype was built in the laboratory according to the geometry listed in Table 4 and tested while using NI LABVIEW Machine Vision and MATLAB to track the nozzle tip's trajectory [15]. Figure 22 shows the simulation data graphed with the prototype data.

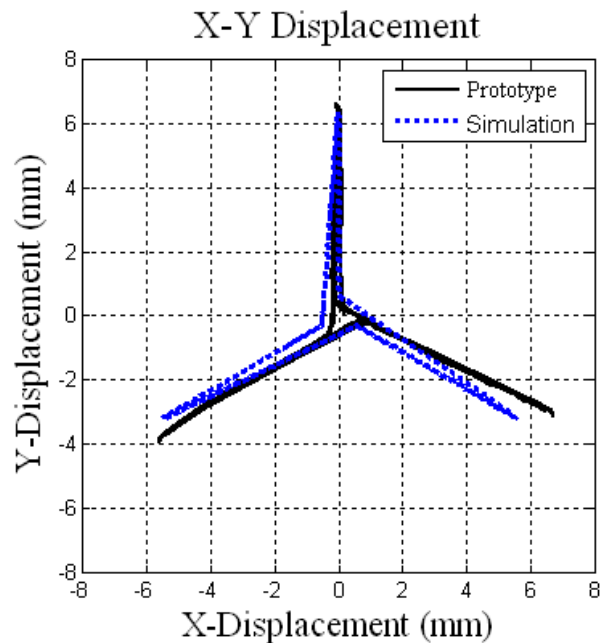


Figure 22: Prototype and simulation results [29].

The trajectory of the nozzle tip from the simulation is similar to the one from the prototype. Due to the sequence of wire actuation, both trajectories have a three-pointed star shape. In addition, both trajectories display similar features during the simulation, as illustrated by

Points C, E, and G in Figure 21a. Overall, the maximum difference in displacement between the two trajectories is 1mm, which occurs at the end points of the three-pointed star.

Difference sequences of wire pair actuation would result in different shaped trajectories.

3.2 Inhomogeneous Temperature Profiles

The second group of simulations is performed under inhomogeneous temperature profiles, where the heat flux equilibrium equations are solved at the structural level within ABAQUS. Thus, the energy balance equation from Eq (1) is rewritten to incorporate the local energy change and a flux term in Eq (2). This new equation is used to calculate the temperature and heat flux for every element along the SMA wire. The elements used to represent the SMA wire are coupled temperature displacement T3D2T elements, which have the same mechanical degrees of freedom as the T3D2 elements used in the homogeneous simulations, but they also have temperature as a degree of freedom. Inhomogeneous temperature profiles describe SMA wire behavior more accurately than homogeneous profiles because they include effects of isothermal boundaries at the ends of the wires. They can also allow for conductive heat transfer studies from SMA wires into other solid structures.

The first inhomogeneous simulation performed consists of a SMA wire under a concentrated load with actuation for adiabatic and isothermal boundary conditions at the ends of the wire.

Next, simulations of an SMA wire coupled with a spring element, two SMA wires coupled together, and an SMA wire coupled with a 3-D elastic beam are presented.

3.2.1 Simulation 5: SMA Wire with Concentrated Load

The fifth simulation performed consists of a SMA wire under a concentrated load with actuation in order to validate the inhomogeneous model and illustrate its capabilities. The SMA model described in Chapter 2 was first implemented into a series of simulations with inhomogeneous temperature, phase fraction, strain and stress profiles using Eq (2) to solve the heat flux equilibrium equations in ABAQUS. This simulation consists of a single SMA wire cyclically actuated under a concentrated load with adiabatic and isothermal boundary conditions and illustrates the model's ability to predict SMA wire behavior with actuation under a concentrated load.

3.2.1.1 Geometry and Parameters

In this simulation, a SMA wire of length 0.05m and radius 25.0e-6m is modeled using 300 three-dimensional, two-node, coupled temperature displacement truss elements (T3D2T) shown in Figure 23. The top of the SMA wire, SMA Node 301, is fixed in displacement and rotation and a concentrated load of magnitude 1.0N is applied to the bottom of the SMA wire, SMA Node 1, in the negative Y direction and held constant for the entire simulation. Power is cyclically supplied to the entire wire in the form of Joule heating in a triangular

waveform with an amplitude of 0.3 Watts for 3 cycles to actuate the SMA wire. The initial conditions and model parameters for the simulation are listed in Table 6 and the results from the simulation are explained in the Results section below.

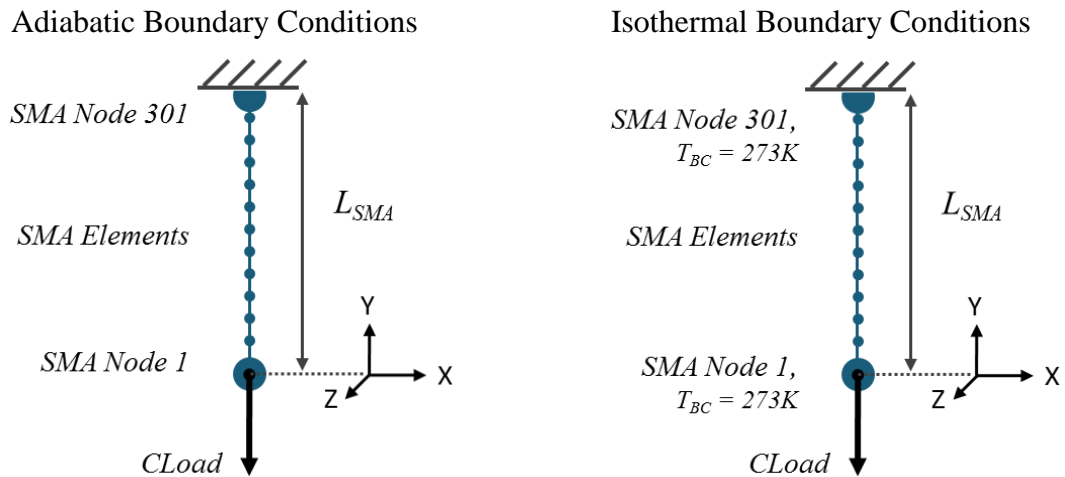


Figure 23: Simulation 5 schematic: SMA wire with a concentrated load and actuation for adiabatic and isothermal boundary conditions.

Table 6: Simulation 5: Initial Conditions and Model Parameters

Parameter	Variable	Value
SMA radius	r_{SMA}	25.0e-6 m
SMA length	L_{SMA}	0.05 m
Martensite +	M+	50%
Martensite -	M-	50%
Pre-stress	σ_o	0.0 MPa
External Temperature	T_{ext}	273.0 K

Two cases with different thermal boundary conditions were analyzed for this simulation. The first case incorporates adiabatic boundary conditions at both the ends of the SMA wire and the second incorporates isothermal boundary conditions at both ends of the SMA wire.

3.2.1.2 Results: Adiabatic Boundary Conditions

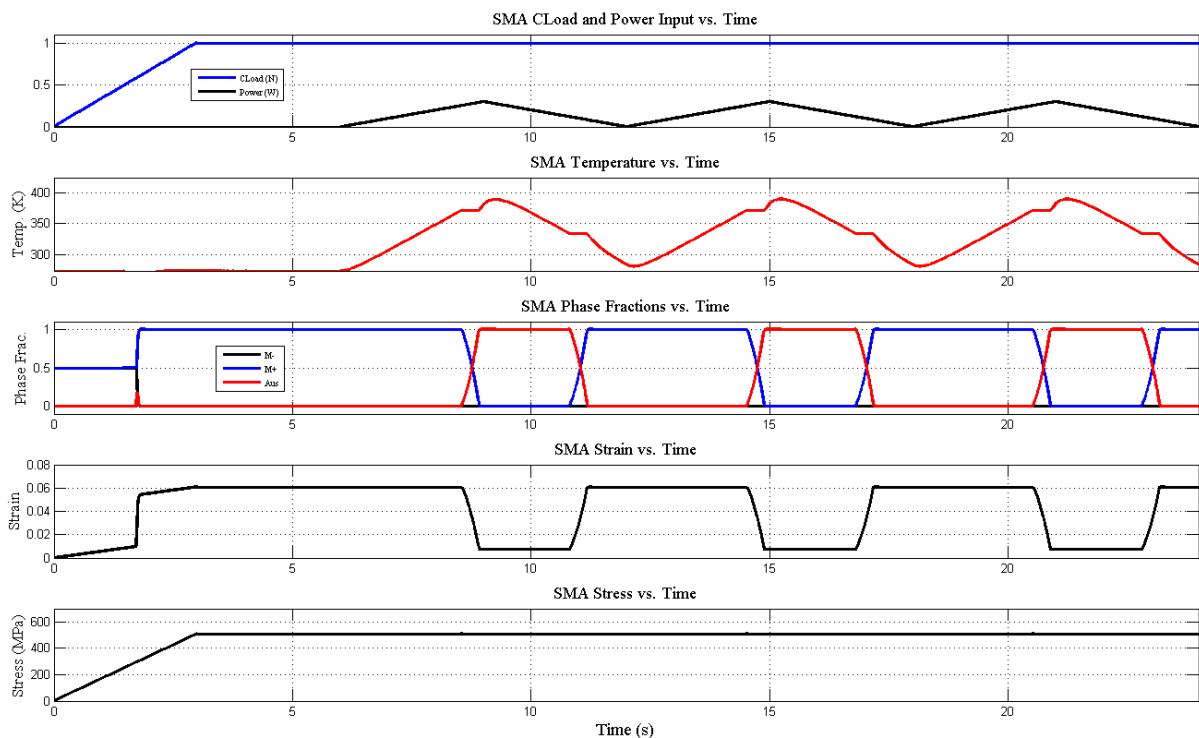


Figure 24: Time resolved concentrated load and power input to SMA actuator and corresponding temperature, phase fractions, strain and stress responses for adiabatic boundary conditions.

The concentrated load and joule heating cycles applied to the SMA are shown in the first graph of Figure 24. These inputs result in changes to the SMA wire's temperature, phase fractions, strain and stress which are also shown in Figure 24 below the input graph. Due to

the inhomogeneous profile, the data in Figure 24 above was taken from the SMA wire's middle element. Profiles along the entire wire are shown in Figures 27-30 for $t=12-18$ s. When the concentrated load is applied from $t=0$ to 3s, the SMA wire experiences a superelastic phase transformation from 50% martensite⁺ and 50% martensite⁻ to 100% martensite⁺. The change to 100% martensite⁺ causes a direct increase in the wire's strain from 0.0% to 6.098% and results in a displacement of 3.049mm in the negative Y direction, graphed in Figure 25. The stress-strain relationship from Eq (7) causes the wire to reach a maximum stress value of 509.3 MPa. When power is applied to the SMA wire from $t=6$ to 9s in the first graph it causes the internal temperature of the SMA to rise. When the internal temperature rises above the martensite to austenite transformation temperature, the wire begins to transform from 100% martensite⁺ and, in this simulation, completely transforms to 100% austenite. Latent heating occurs inside the wire during this transformation and its effects are visible in the temperature versus time graph as a small wave occurring at $t=8$ s. The change in phase fractions also causes a direct decrease in strain from 6.098% to 0.7163%, which in turn causes a change in displacement of 2.6908mm in the positive Y direction as shown in Figure 25. When the joule heating is gradually released from $t=9$ to 12s, the temperature of the wire also decreases and drops below the austenite to martensite transformation temperature. At this temperature, the wires begin transforming back to martensite⁺. The concentrated load applied to the end of the wire also assists in the transformation back to martensite⁺. Latent heats of transformation also occur during this transformation and are visible in the temperature versus time graph as a small wave occurring at $t=11$ s. The phase fractions of the SMA wire return to 100% martensite⁺ from 100%

austenite, which causes the strain to increase from 0.71632% to 6.098%. The same sequence of wire transformation occurs for the next 2 joule heating cycles. The SMA stress versus strain and strain versus temperature responses are graphed in Figure 26.

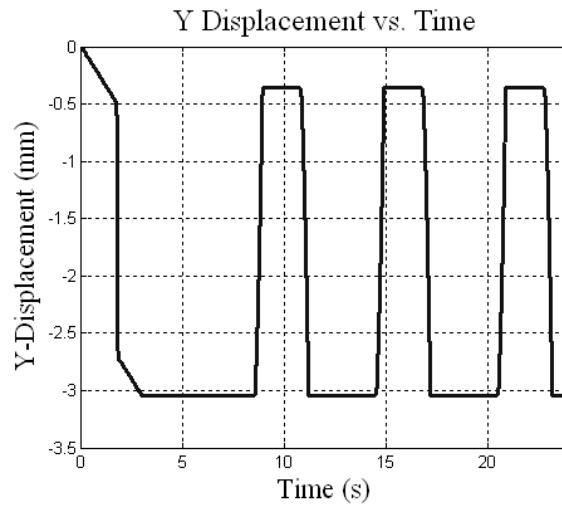


Figure 25: SMA Wire tip displacement versus time response for adiabatic boundary conditions.

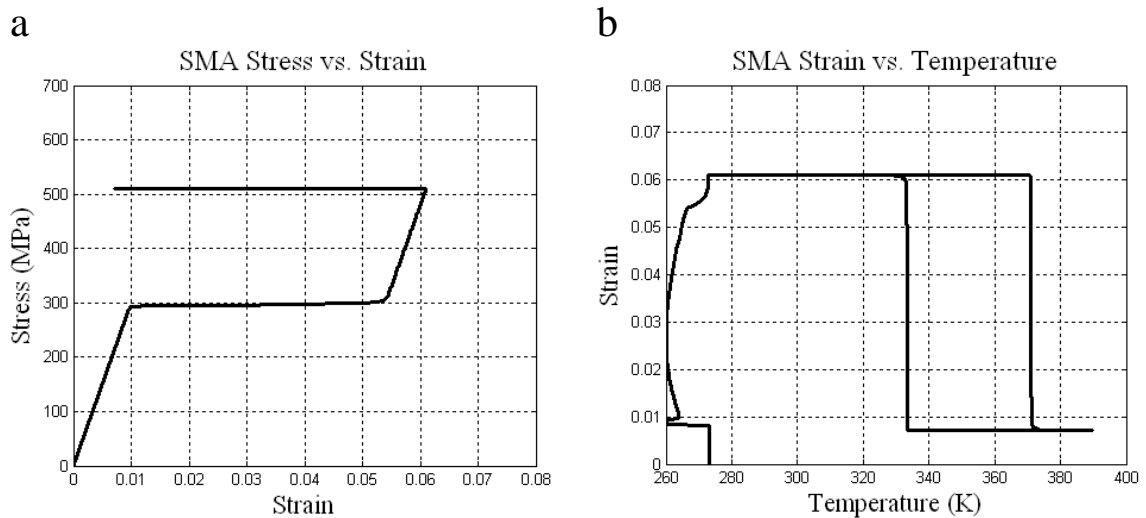


Figure 26: (a) Stress versus strain and (b) strain versus temperature relationships for adiabatic boundary conditions.

The following graphs show the temperature, martensite+ and strain profiles along the SMA wire during heating from $t=12$ to 15s and cooling from $t=15$ to 18s. All three graphs show the effects of adiabatic temperature boundary conditions on the SMA wire. As power is supplied, the temperature profile along the wire rises uniformly, and the temperature at the center of the wire is equal to the temperature at its ends. A uniform increase in temperature causes a uniform transformation from martensite+ to austenite along the wire, which directly results in a uniform strain change.

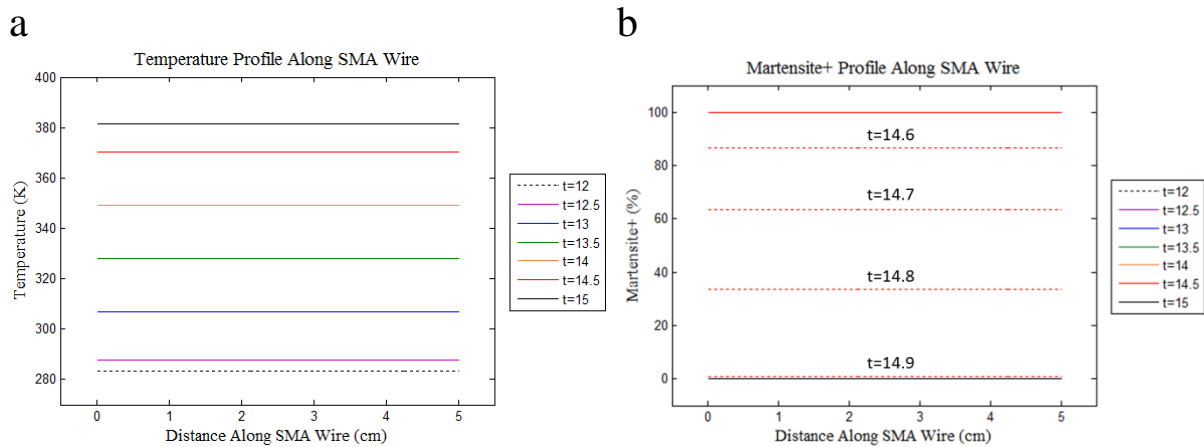


Figure 27: Evolution of (a) temperature and (b) martensite+ along the length of the SMA wire from $t=12$ to 15s for adiabatic boundary conditions.

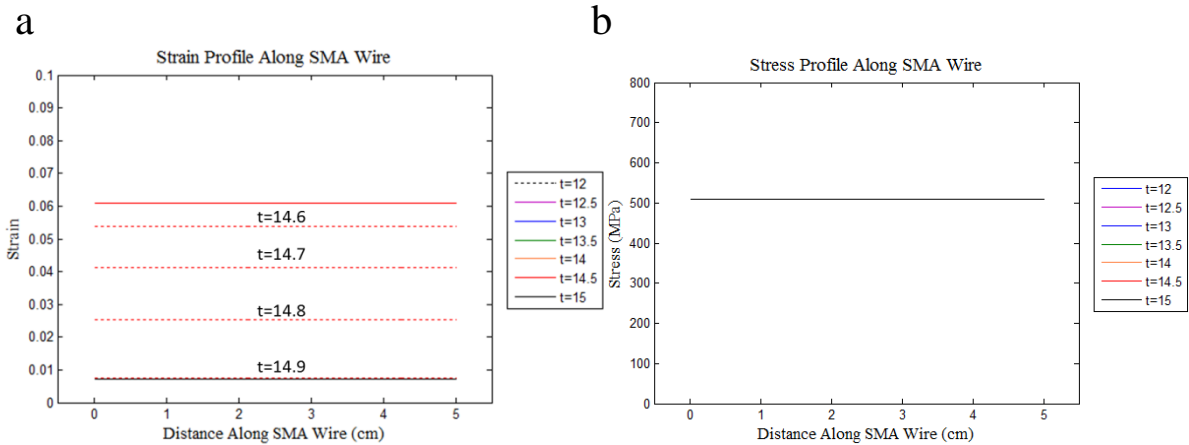


Figure 28: Evolution of (a) strain and (b) stress along the length of the SMA wire from t=12 to 15s for adiabatic boundary conditions.

When power is gradually released the temperature profile uniformly decreases and the martensite+ and strain profiles increase also uniformly. The stress in the wire is consistent because of the applied concentrated load at the beginning of the simulation.

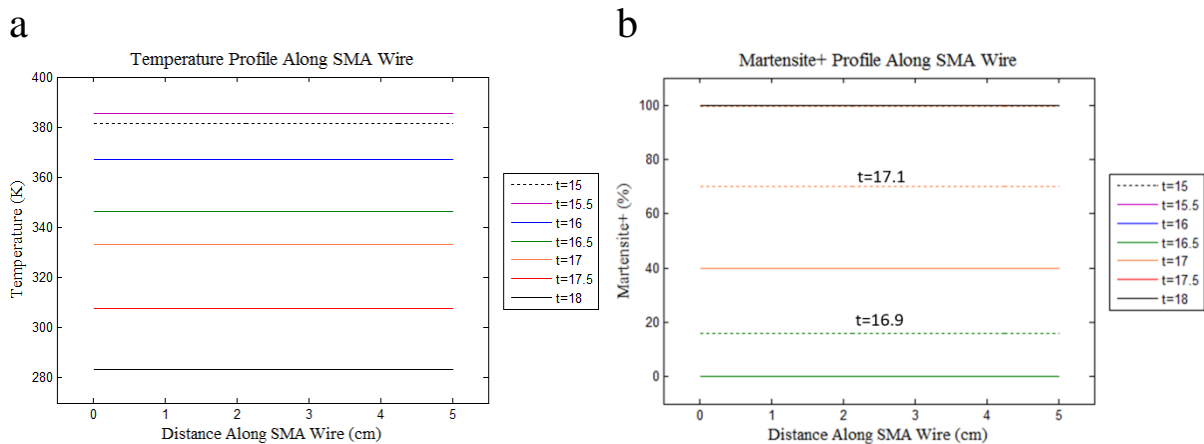


Figure 29: Evolution of (a) temperature and (b) martensite+ along the length of the SMA wire from t=15-18s for adiabatic boundary conditions.

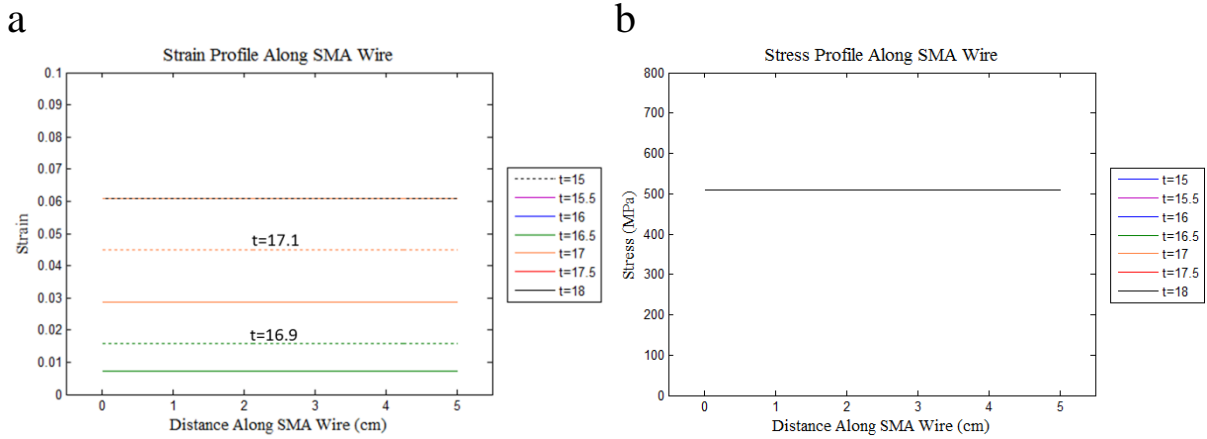


Figure 30: Evolution of (a) strain and (b) stress along the length of the SMA wire from t=15-18s for adiabatic boundary conditions.

3.2.1.3 Results: Isothermal Boundary Conditions

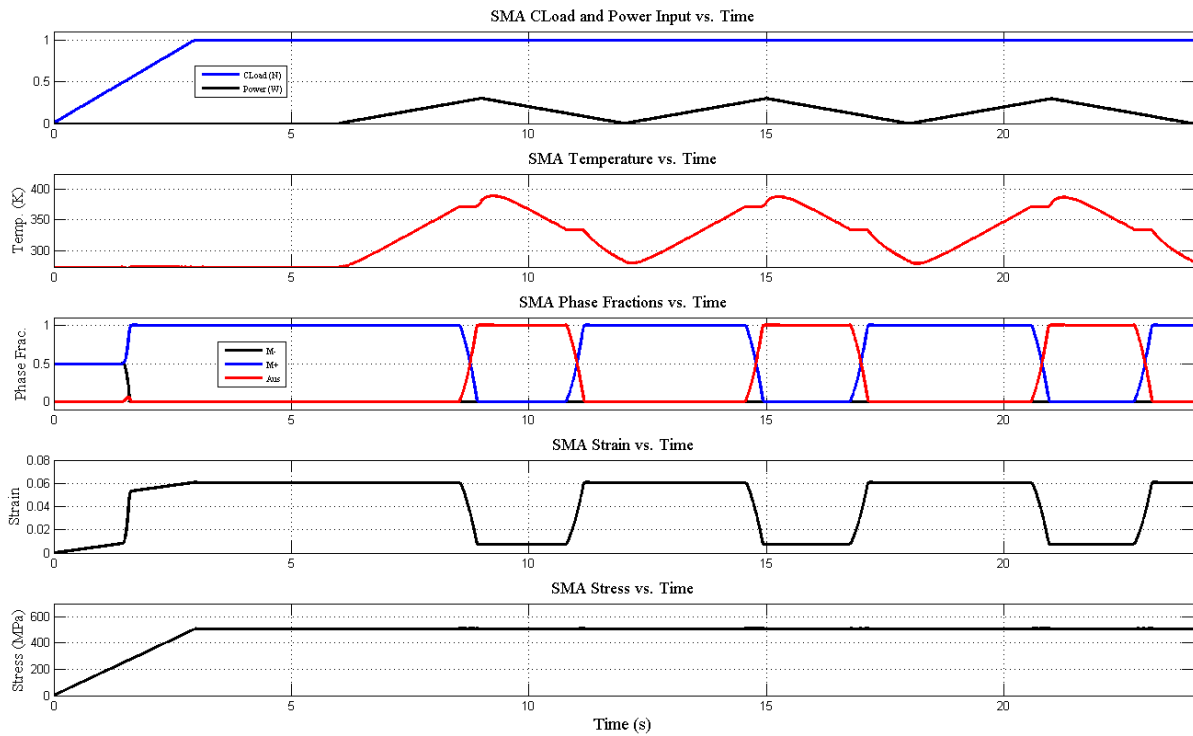


Figure 31: Time resolved concentrated load and power input to SMA actuator and corresponding temperature, phase fractions, strain and stress responses for isothermal boundary conditions.

The concentrated load and joule heating cycles applied to the SMA are shown in the first graph of Figure 31. These inputs result in changes to the SMA wire's temperature, phase fractions, strain and stress which are also shown in Figure 31 below the input graph. Due to the inhomogeneous profile, the data in Figure 31 above was taken from the SMA wire's middle element. Profiles along the entire wire are shown in Figures 34-41 for $t=12-18s$. When the concentrated load is applied from $t=0$ to $3s$, the SMA wire experiences a superelastic phase transformation from 50% martensite⁺ and 50% martensite⁻ to 100% martensite⁺. The change to 100% martensite⁺ causes a direct increase in the wire's strain from 0.0% to 6.098% and results in a displacement of 3.049mm in the negative Y direction, which is graphed in Figure 32. The stress-strain relationship from Eq (7) causes the wire to reach a maximum stress value of 509.3 MPa. When power is applied to the SMA wire from $t=6$ to $9s$ in the first graph it causes the internal temperature of the SMA to rise. When the internal temperature rises above the martensite to austenite transformation temperature, the wire begins to transform from 100% martensite⁺ and, in this simulation, completely transforms to 100% austenite. Latent heating occurs inside the wire during this transformation and its effects are visible in the temperature versus time graph as a small wave occurring at $t=8s$. The change in phase fractions also causes a direct decrease in strain from 6.098% to 0.7163%, which in turn causes a change in displacement of 2.6908mm in the positive Y direction. When the joule heating is gradually released from $t=9$ to $12s$, the temperature of the wire also decreases and drops below the austenite to martensite transformation temperature. At this temperature, the wires begin transforming back to martensite⁺. The concentrated load which is continuously applied to the end of the wire also

assists in transforming the wire back to martensite+. Latent heats of transformation also occur during this transformation and are visible in the temperature versus time graph as a small wave occurring at $t=11$ s. The phase fractions of the SMA wire return to 100% martensite+ from 100% austenite, which causes the strain to increase from 0.7163% to 6.098%. The same sequence of wire transformation occurs for the next 2 joule heating cycles. The SMA stress versus strain and strain versus temperature responses are graphed in Figure 33.

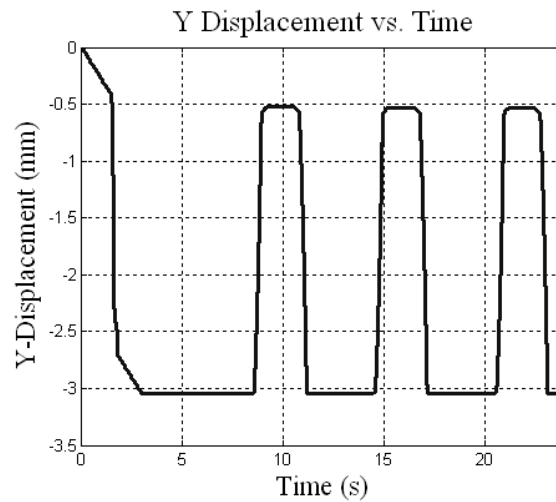


Figure 32: SMA wire tip displacement versus time response for isothermal boundary conditions.

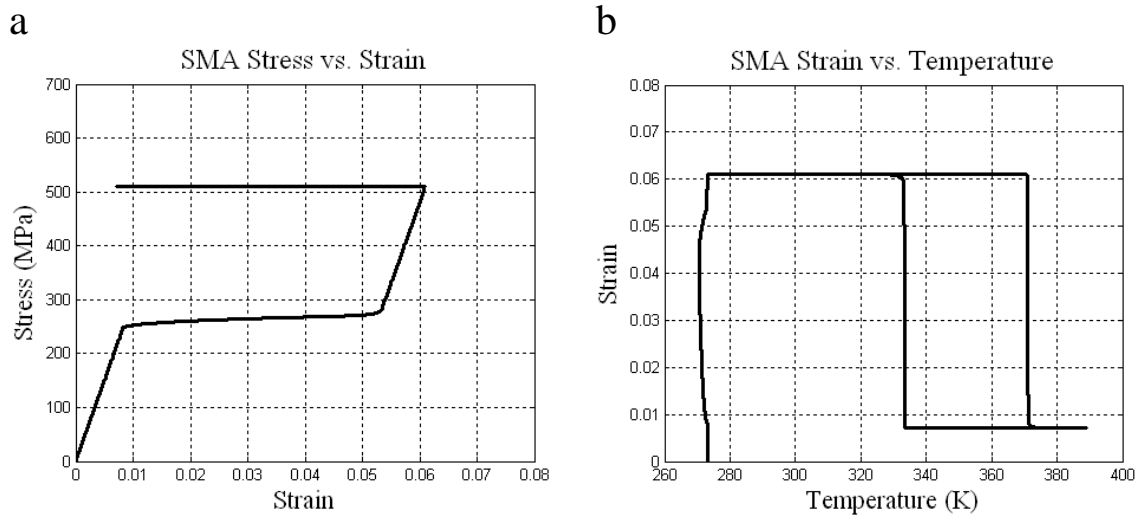


Figure 33: (a) Stress versus strain and (b) strain versus temperature relationships for isothermal boundary conditions.

The following graphs show the temperature, martensite+ and strain profiles along the SMA wire during heating from $t=12$ to 15 s and cooling from $t=15$ to 18 s. All three graphs show the effects of isothermal temperature boundary conditions on the ends of the SMA wire. As power is supplied, the temperature in the center of the wire is not equal to the temperature at the wire's ends. As a result, the transition from martensite+ to austenite occurs proportionally with the temperature at each point along the wire. The amount of martensite+ and austenite along the wire directly results in the strain along the wire.

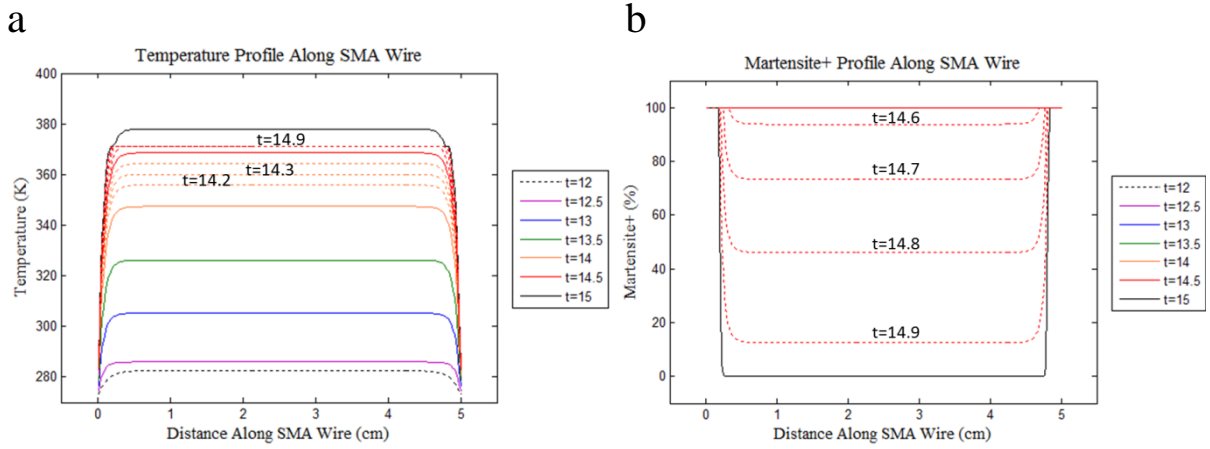


Figure 34: Evolution of (a) temperature and (b) martensite+ along the length of the SMA wire from t=12-15s for isothermal boundary conditions.

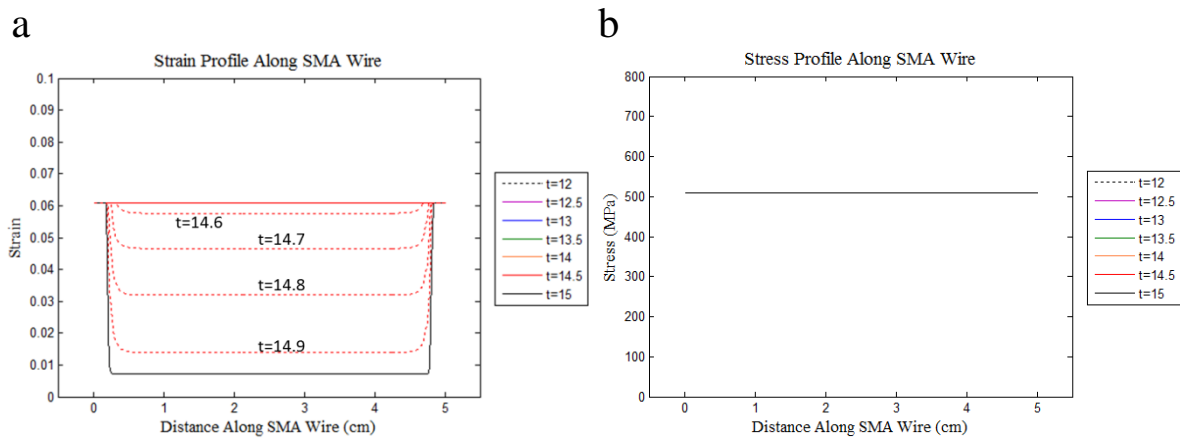


Figure 35: Evolution of (a) strain and (b) stress along the length of the SMA wire from t=12 to 15s for isothermal boundary conditions.

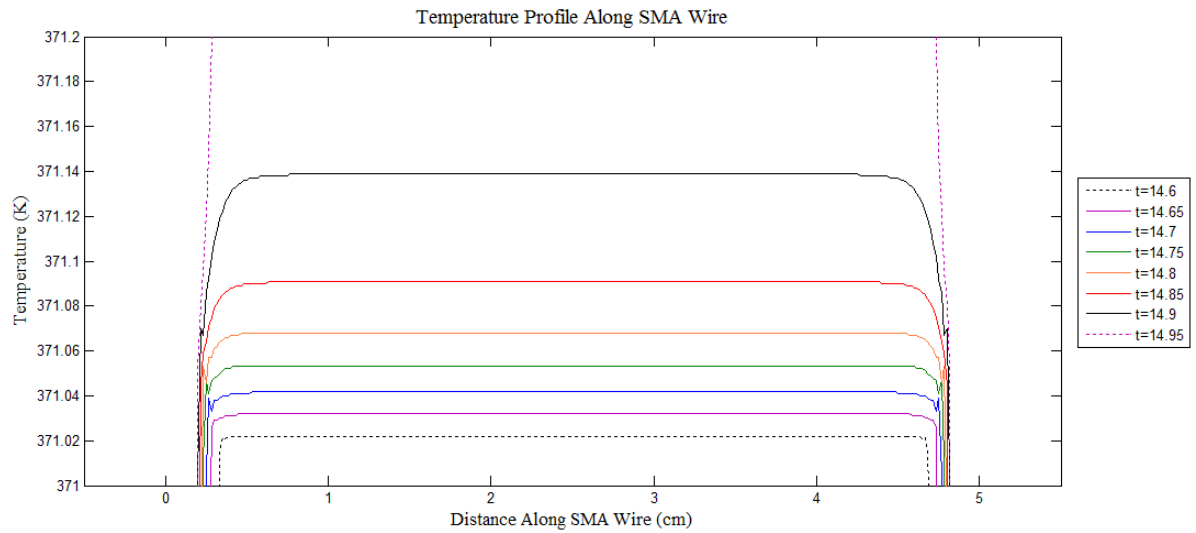


Figure 36: Evolution of heating along the length of the SMA wire from $t=14.5$ - 14.95 s.

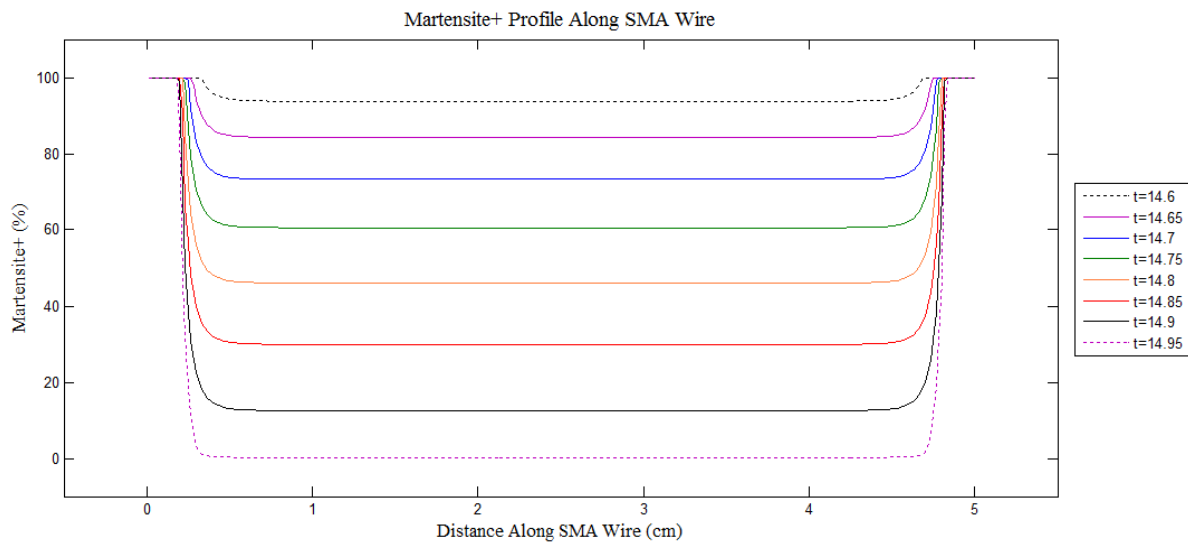


Figure 37: Evolution of martensite+ along the length of the SMA wire from $t=14.5$ - 14.95 s.

When power is gradually released the temperature along the wire decreases and approaches the temperature at the ends of the wire. A decrease in temperature results in a decrease in

austenite and an increase in martensite+, which also results in an increase in strain. The stress in the wire is consistent because of the applied concentrated load at the beginning of the simulation.

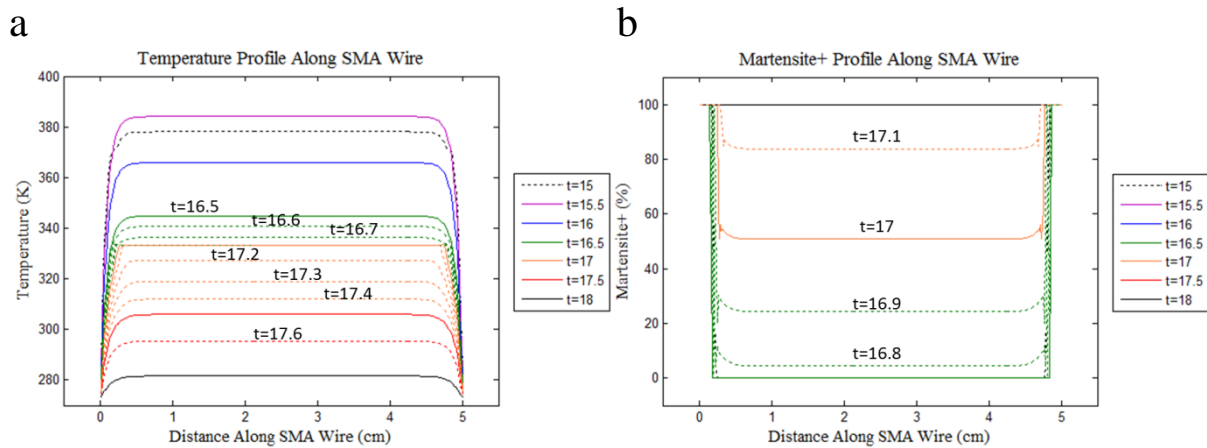


Figure 38: Evolution of (a) temperature and (b) martensite+ along the length of the SMA wire from t=15-18s for isothermal boundary conditions.

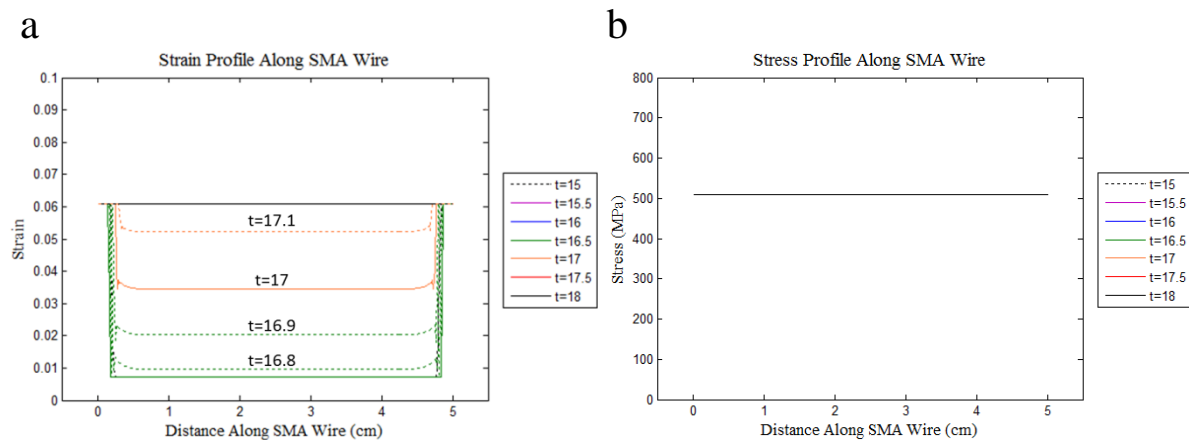


Figure 39: Evolution of (a) strain and (b) stress along the length of the SMA wire from t=15-18s for isothermal boundary conditions.

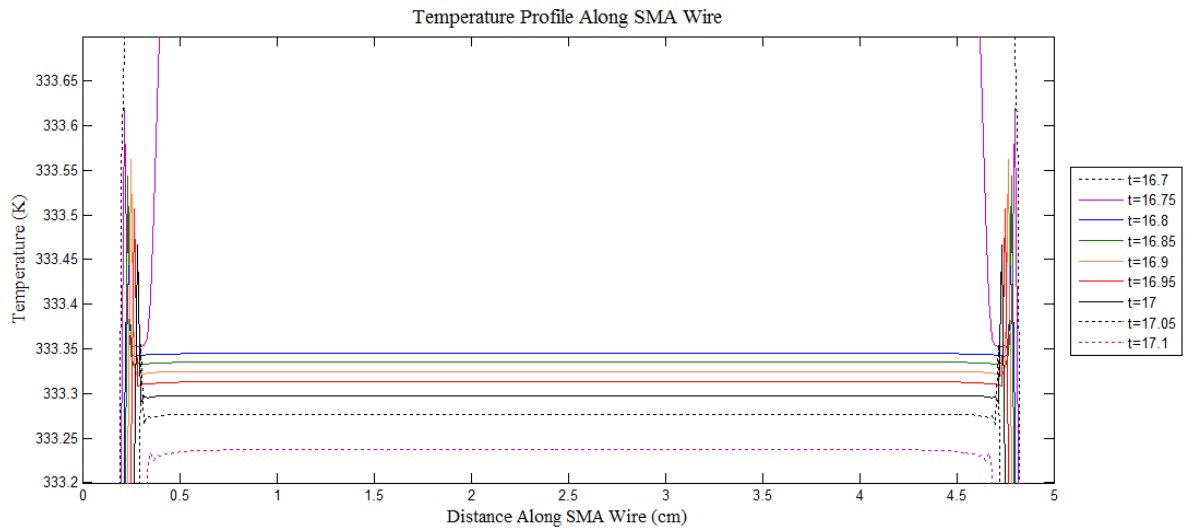


Figure 40: Evolution of temperature along the length of the SMA wire from $t=16.7-17.1$ s.

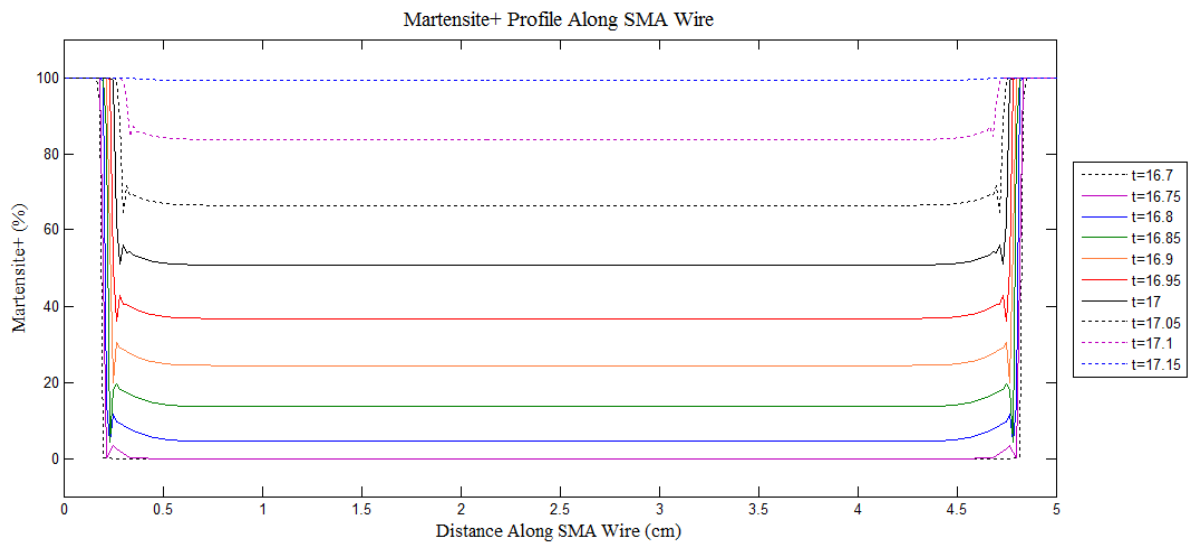


Figure 41: Evolution of martensite+ along the length of the SMA wire from $t=16.7-17.1$ s.

The results from these simulations of an SMA wire under an applied load with actuation shows the model's ability to predict SMA wire behavior for adiabatic and isothermal boundary conditions.

3.2.1.4 Results: Comparison

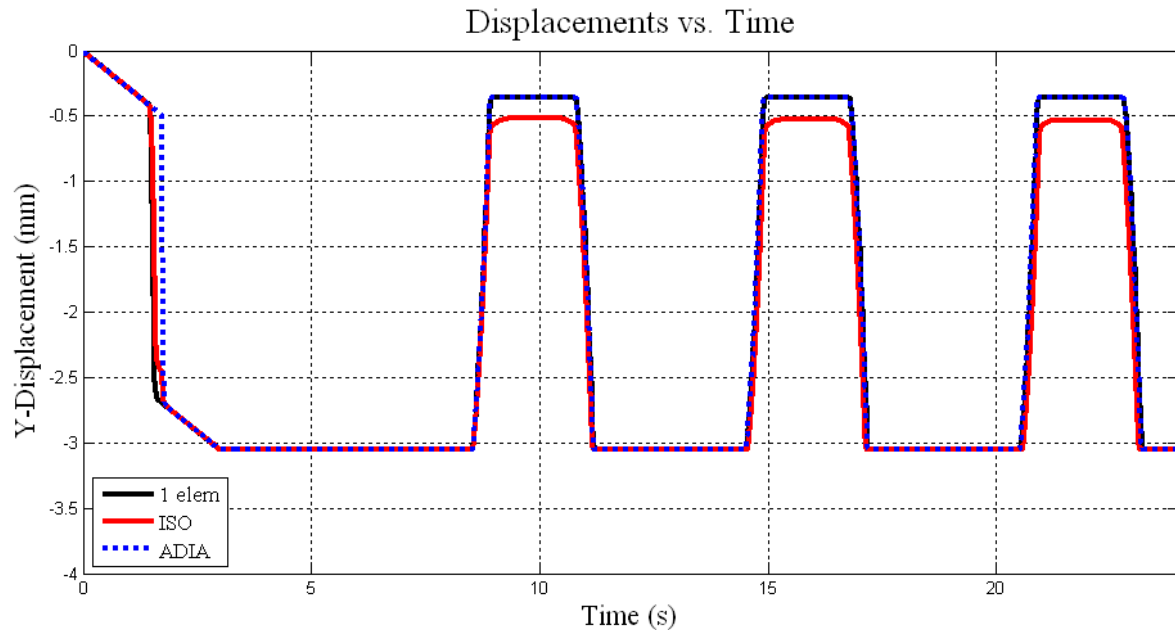


Figure 42: Displacement comparison of an actuated SMA wire under a concentrated load with homogeneous and inhomogeneous temperature profiles.

The above graph compares the displacement of a single wire element from Simulation 2 (black line) against an inhomogeneous wire with adiabatic temperature boundary conditions (dashed blue line) and an inhomogeneous wire with isothermal boundary conditions (red line). All simulations were identical in geometry, material properties, applied load and actuation. The results show a difference in displacement between all three cases. The single element and adiabatic boundary condition cases have 0.165mm more displacement than the isothermal case. This difference in displacement is due to the ends of the wire with isothermal boundary conditions, which do not allow for a full transformation to austenite and thus a decrease in strain resulting in a larger displacement. These differences in

displacement, although small in this case, show that temperature boundary conditions have an effect on the performance of SMA wires and should be considered in SMA simulations.

This simulation shows the model's ability to predict the coupled temperature-displacement behavior for a SMA wire SMA wire under an applied load with actuation with an inhomogeneous temperature profile under both adiabatic and isothermal boundary conditions.

3.2.2 Simulation 6: SMA Wire and Spring

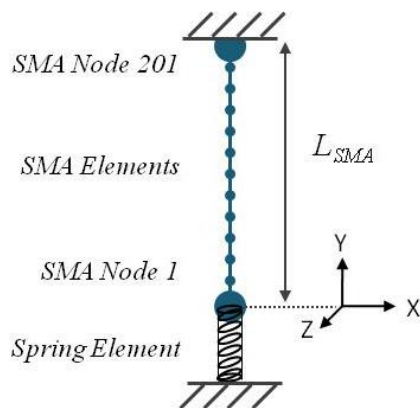
This next simulation also implements the same SMA model described in Chapter 2 using Eq (2) for inhomogeneous temperature, phase fraction, strain and stress profiles along the SMA wire with both adiabatic and isothermal boundary conditions. The sixth simulation increases in complexity by coupling the SMA wire with a very stiff spring element and observing the effects of wire actuation. The resulting temperature, phase fractions, strain, stress, and displacements are investigated versus time.

3.2.2.1 Geometry and Parameters

In this simulation, a SMA wire is coupled with a very stiff spring and actuated with joule heating. The SMA wire has a length of 0.05m, a radius 25.0e-6m and is modeled using 200

three-dimensional, two-node, coupled temperature displacement truss elements (T3D2T) shown in Figure 43. The spring is modeled as a single SPRING1 element. The top of the SMA wire, SMA Node 201, is fixed in displacement and rotation and the bottom of the SMA wire, SMA Node 1, is tied to the SPRING1 element. The SPRING1 element is fixed to the ground on one end and acts only in one direction. Power is cyclically supplied to the wire in the form of Joule heating in a triangular waveform with an amplitude of 0.65 Watts for 2 cycles to actuate the SMA wire. The initial conditions and model parameters for the simulation are listed in Table 7 and the results from the simulation are explained in the Results section below.

Adiabatic Boundary Conditions



Isothermal Boundary Conditions

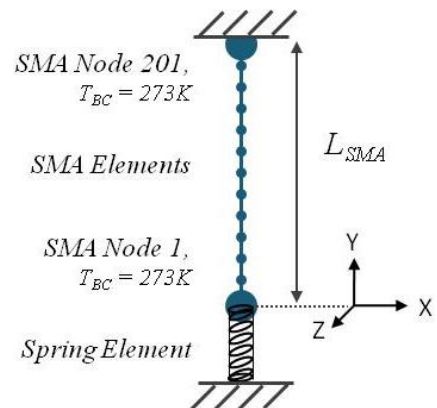


Figure 43: Simulation 6 schematic: single SMA wire attached to a spring with actuation for adiabatic and isothermal boundary conditions.

Table 7: Simulation 6: Initial Conditions and Model Parameters.

Parameter	Variable	Value
Spring Stiffness	k_{spring}	3.0e+03 N/m
SMA radius	r_{SMA}	25.0e-6 m
SMA length	L_{SMA}	0.05 m
Initial Condition: Martensite+	M_{+o}	100%
Initial Condition: Martensite-	M_{-o}	0%
Initial Condition: Pre-stress	σ_o	0.0 MPa
External Temperature	T_{ext}	273.0 K

3.2.2.2 Results: Adiabatic Boundary Conditions

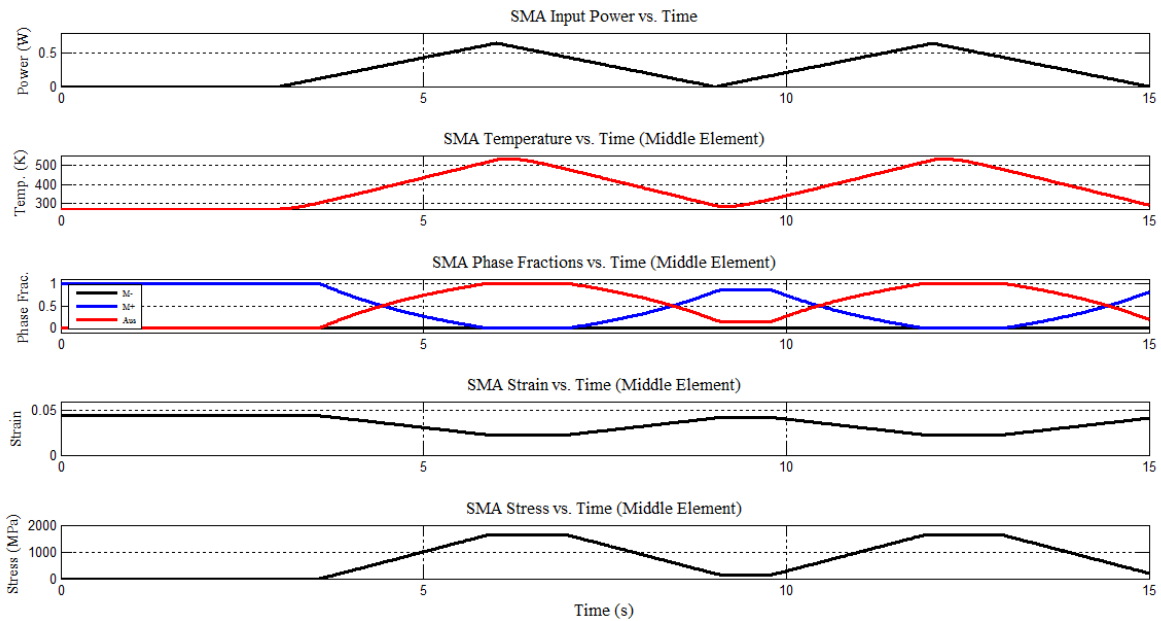


Figure 44: Time resolved power input to SMA actuator and corresponding temperature, phase fractions, strain and stress responses for adiabatic boundary conditions.

The SMA wire is initially in 100% martensite+ with 4.4% strain (0.0 MPa of pre-stress). The temperature boundary conditions at both ends of the SMA wire are adiabatic. As power is

applied to the SMA in the first graph, changes in the SMA wire temperature, phase fractions, strain, and stress occur in the following graphs versus time. Due to the inhomogeneous profile, the data in Figure 44 above was taken from the SMA wire's middle element. Profiles along the entire wire are shown in Figures 47-50 for $t=9-15$ s. When the wire is gradually heated to 0.65W from $t=3$ to 6s in the first graph it causes the internal temperature of the SMA to rise and reach 533.2K. When the internal temperature rises above the martensite to austenite transformation temperature the wire begins to transform from 100% martensite+ and, in this simulation, completely transform to austenite. The change in phase fractions causes a direct decrease in strain from 4.4% to 2.279%, which in turn causes a change in displacement of the wire end from 0.0mm to 1.061mm as shown in Figure 45. The stress-strain relationship from Eq (7) causes the wire to reach a maximum stress value of 1620 MPa. When the joule heating is gradually released from $t=6$ to 9s, the temperature of the wire decreases and drops below the austenite to martensite transformation temperature. At this temperature, the wire begins transforming back to martensite+. The phase fractions at the end of transformation are 85.8% martensite+ and 14.2% austenite, which correspond to a strain value of 4.213% and a stress value of 143 MPa. The SMA wire does not return to 100% martensite+ at the end of the actuation cycles because the spring stiffness does not provide enough restoring force to the SMA wire. When power is supplied to the SMA wire at $t=9$ s for the next joule heating cycle, the same sequence of wire heating and transformation occurs from the previous state of the SMA. The SMA stress versus strain and strain versus temperature responses are graphed in Figure 46.

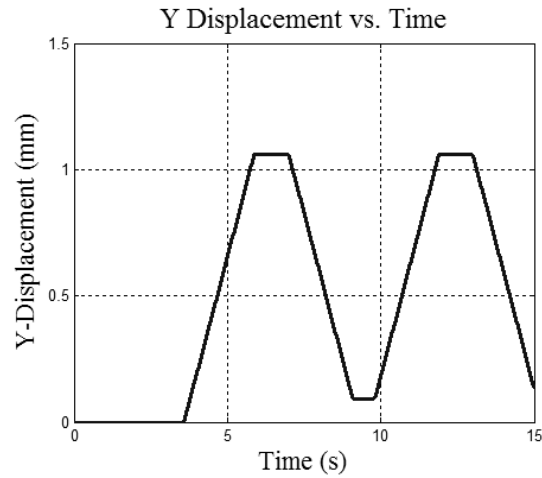


Figure 45: SMA Wire tip displacement versus time response for adiabatic boundary conditions.

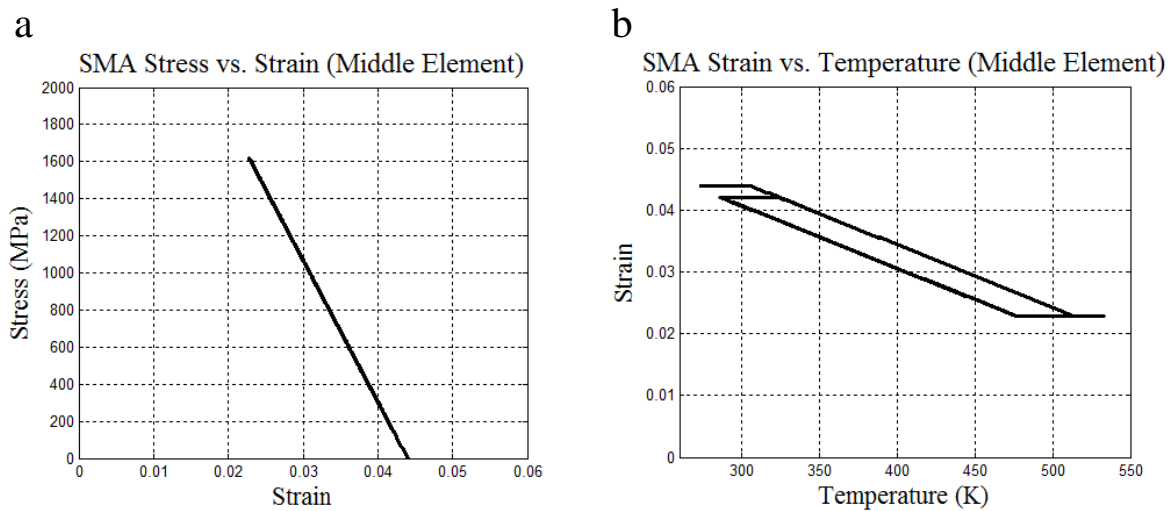


Figure 46: (a) Stress versus strain and (b) strain versus temperature relationships for adiabatic boundary conditions.

The following graphs show the temperature, martensite+ and strain profiles along the SMA wire during heating from $t=9$ to 12 s and cooling from $t=12$ to 15 s. All four graphs show the effects of adiabatic temperature boundary conditions on the SMA wire. As power is supplied, the temperature profile along the wire rises uniformly, and the temperature at the center of

the wire is equal to the temperature at its ends. A uniform increase in temperature causes a uniform transformation from martensite+ to austenite along the wire, which directly results in a uniform strain and stress change.

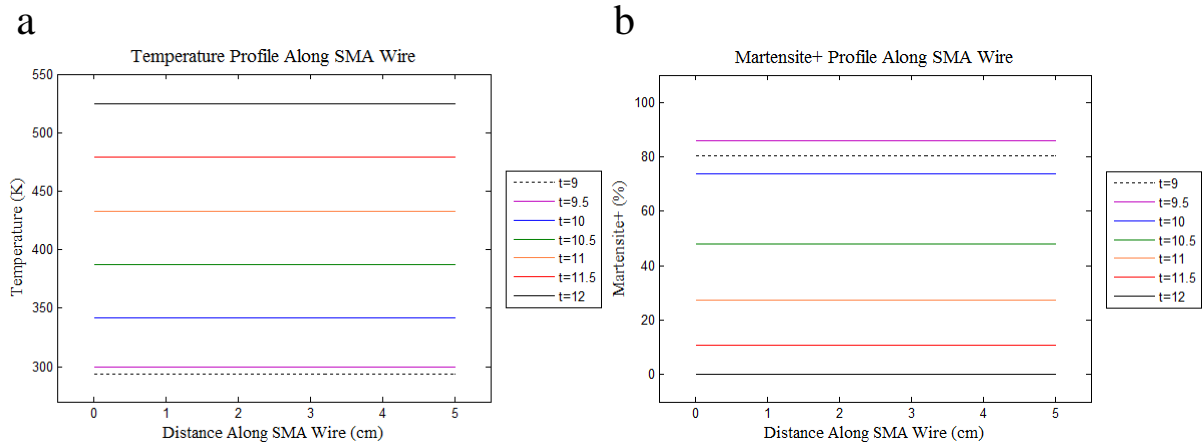


Figure 47: Evolution of (a) temperature and (b) martensite+ along the length of the SMA wire from t=9-12s for adiabatic boundary conditions.

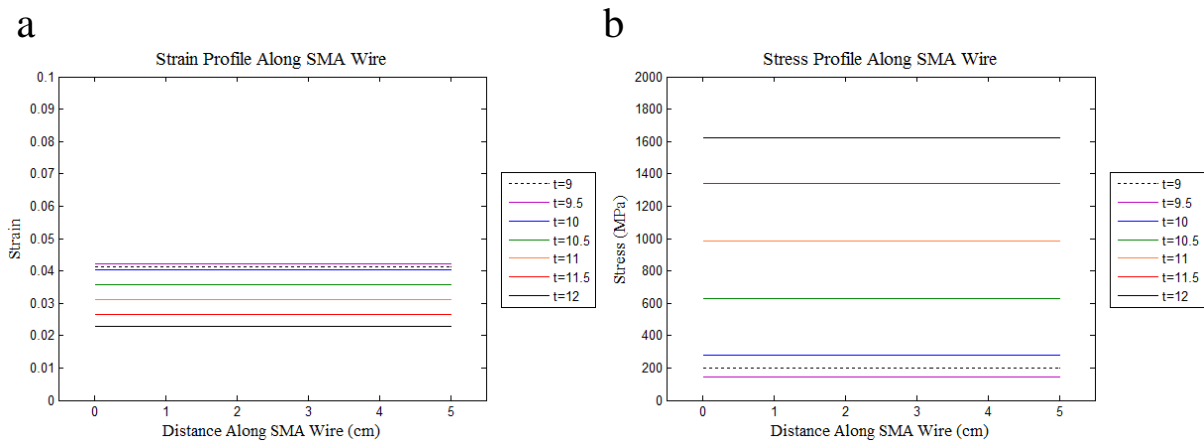


Figure 48: Evolution of (a) strain and (b) stress along the length of the SMA wire from t=9-12s for adiabatic boundary conditions.

When power is gradually released from t=12 to 15s the temperature profile uniformly decreases and the martensite+, strain and stress profiles also change uniformly.

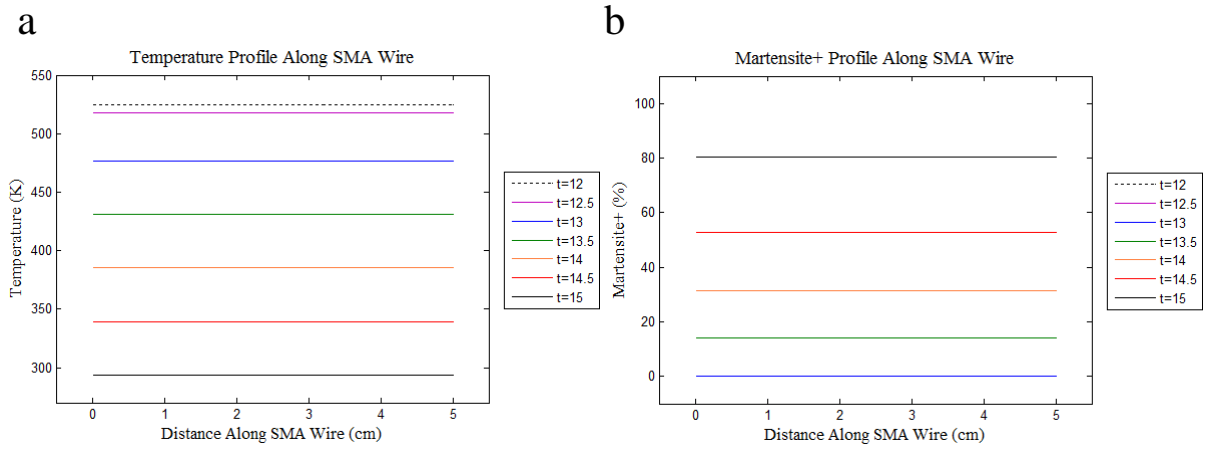


Figure 49: Evolution of (a) temperature and (b) martensite+ along the length of the SMA wire from t=12-15s for adiabatic boundary conditions.

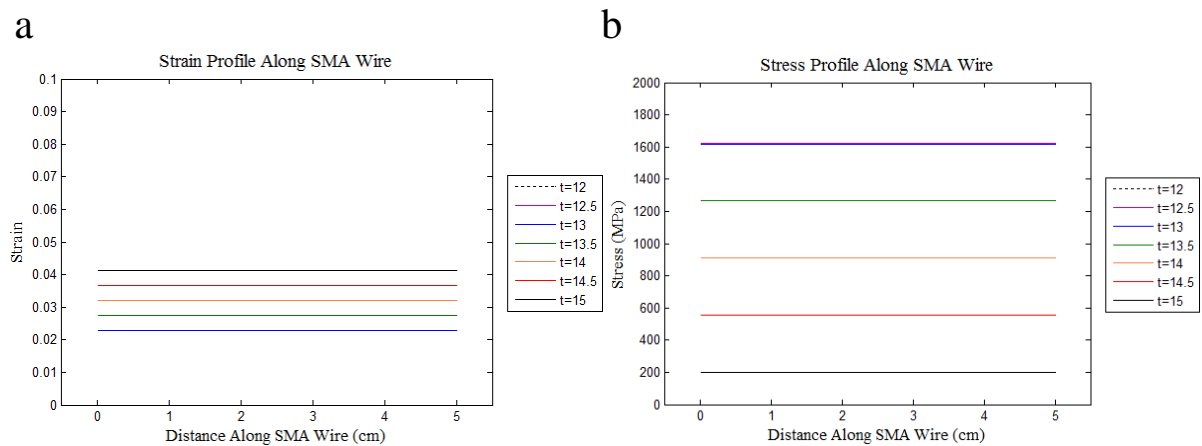


Figure 50: Evolution of strain and stress along the length of the SMA wire from t=12-15s for adiabatic boundary conditions.

3.2.2.3 Results: Isothermal Boundary Conditions

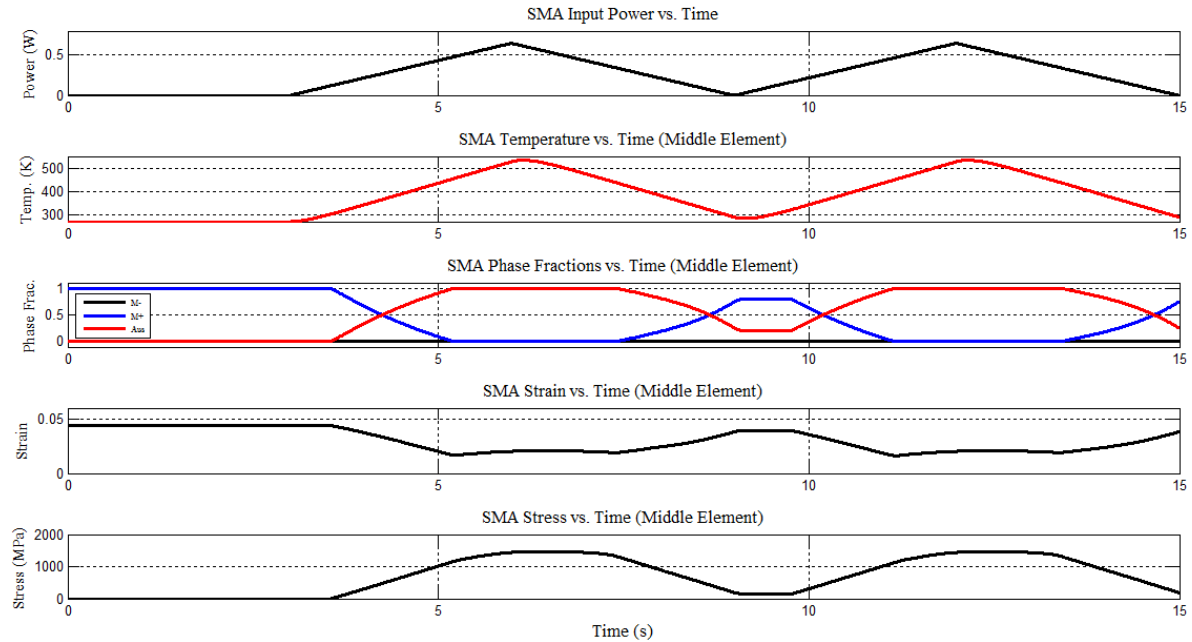


Figure 51: Time resolved power input to SMA actuator and corresponding temperature, phase fractions, strain and stress responses for isothermal boundary conditions.

The SMA wire is initially in 100% martensite+ with 4.4% strain (0.0 MPa of pre-stress). The temperature boundary conditions at both ends of the SMA wire are adiabatic. As power is applied to the SMA in the first graph, changes in the SMA wire temperature, phase fractions, strain, and stress occur in the following graphs versus time. Due to the inhomogeneous profile, the data in Figure 51 above was taken from the SMA wire's middle element. Profiles along the entire wire are shown in Figures 54-61 for $t=9-15$ s. When the wire is gradually heated to 0.65W from $t=3$ to 6s in the first graph it causes the internal temperature of the SMA to rise and reach 533.7K. When the internal temperature rises above the martensite to austenite transformation temperature the wire begins to transform from 100% martensite+ and, in this simulation, completely transforms to austenite. The change in phase fractions

causes a direct decrease in strain from 4.4% to 2.055%, which in turn causes a change in displacement of the wire end from 0.0mm to 0.9562mm, as shown in Figure 52. The stress-strain relationship from Eq (7) causes the wires to reach a maximum stress value of 1461 MPa. When the joule heating is gradually released from $t=6$ to 9s, the temperature of the wire decreases and drops below the austenite to martensite transformation temperature. At this temperature, the wire begins transforming back to martensite+. The phase fractions at the end of transformation are 79.87% martensite+ and 20.13% austenite, which correspond to a strain value of 3.947% and a stress value of 147 MPa. The SMA wire does not return to 100% martensite+ at the end of the actuation cycles because the spring stiffness does not provide enough restoring force to the SMA wire. When power is supplied to the SMA wire at $t=9$ s for the next joule heating cycle, the same sequence of wire heating and transformation occurs from the previous state of the SMA. The SMA stress versus strain and strain versus temperature responses are graphed in Figure 53.

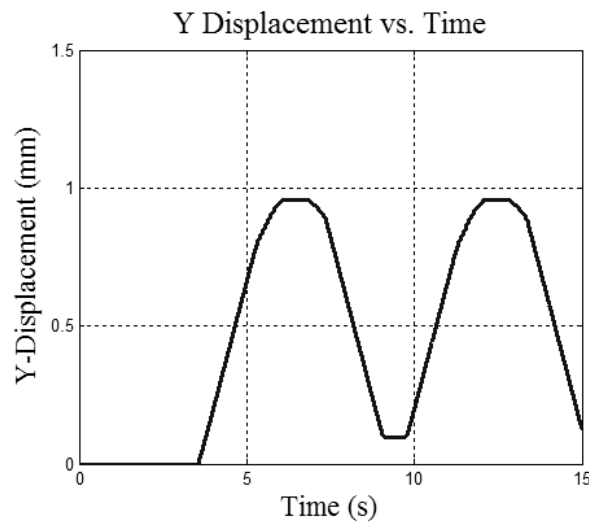


Figure 52: SMA Wire tip displacement versus time response for isothermal boundary conditions.

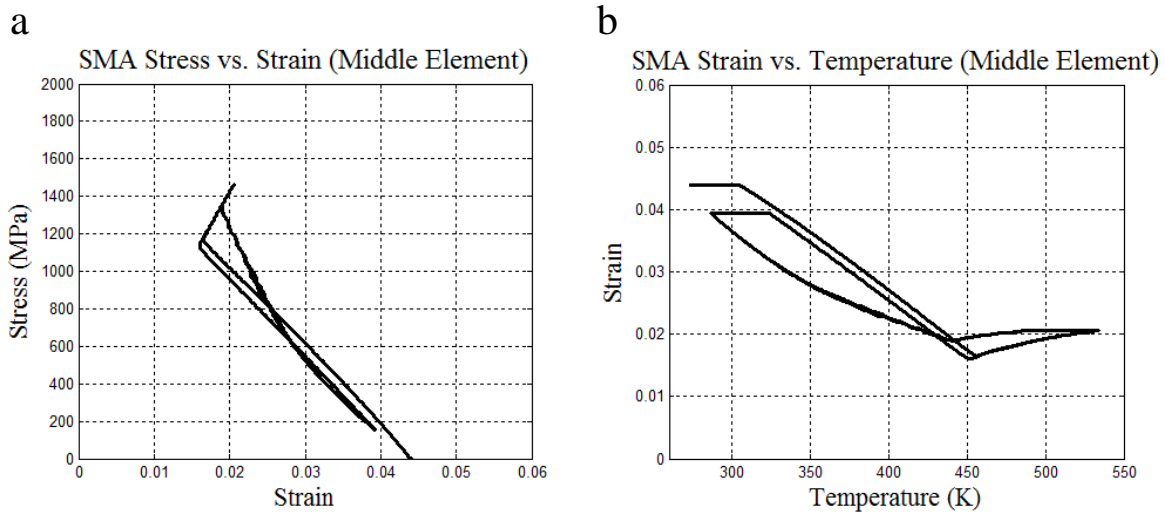


Figure 53: (a) Stress versus strain and (b) strain versus temperature relationships for isothermal boundary conditions.

The following graphs show the temperature, martensite+ and strain profiles along the SMA wire during heating from $t=9$ to 12s and cooling from $t=12$ to 15s. All four graphs show the effects of isothermal temperature boundary conditions on the ends of the SMA wire. As power is supplied, the temperature in the center of the wire is not equal to the temperature at the wire's ends. As a result, the transition from martensite+ to austenite occurs proportionally with the wire's temperature. The amount of martensite+ and austenite along the wire directly results in the strain and stress change along the wire.

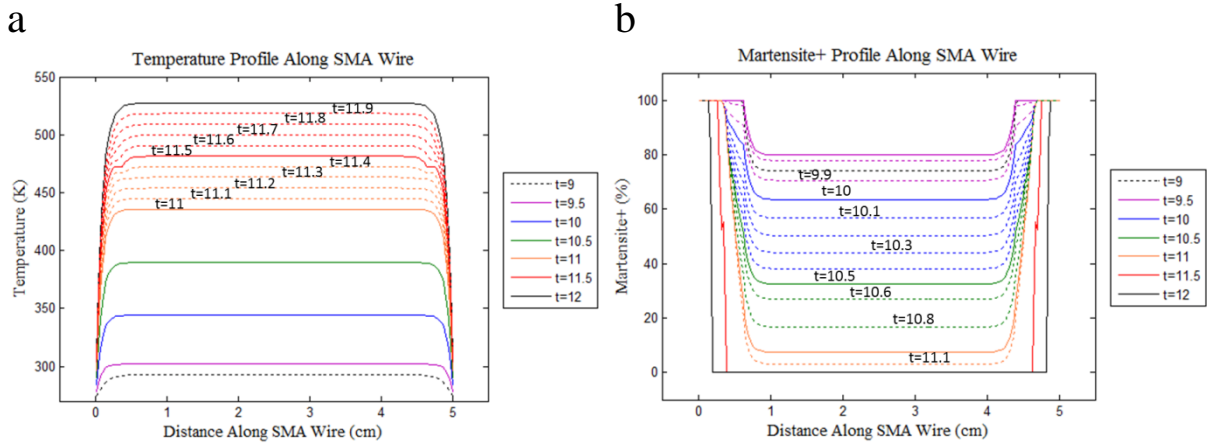


Figure 54: Evolution of (a) temperature and (b) martensite+ along the length of the SMA wire from t=9-12s for isothermal boundary conditions.

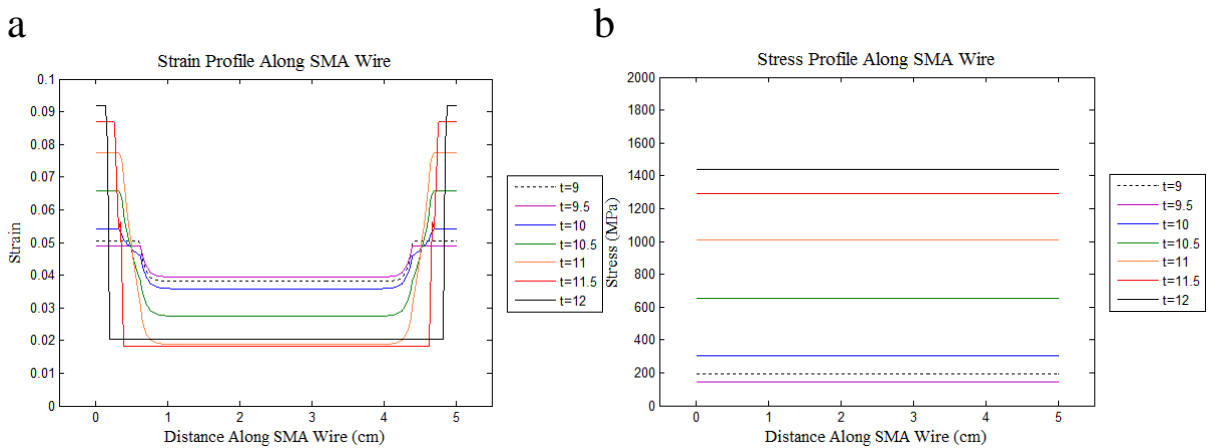


Figure 55: Evolution of (a) strain and (b) stress along the length of the SMA wire from t=9-12s for isothermal boundary conditions.

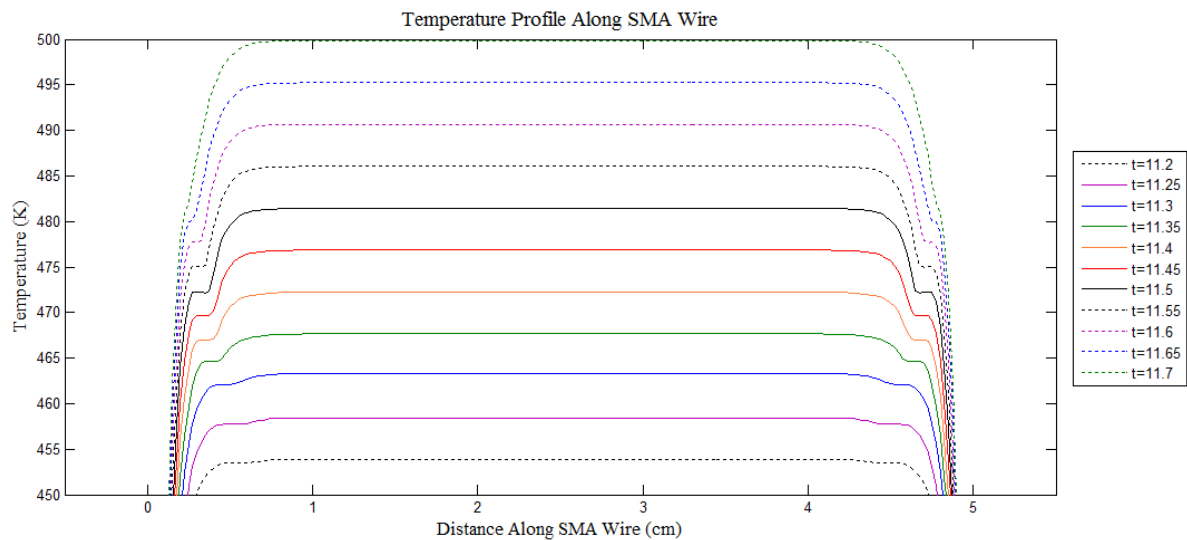


Figure 56: Evolution of temperature along the length of the SMA wire from $t=11.2-11.7$ s.

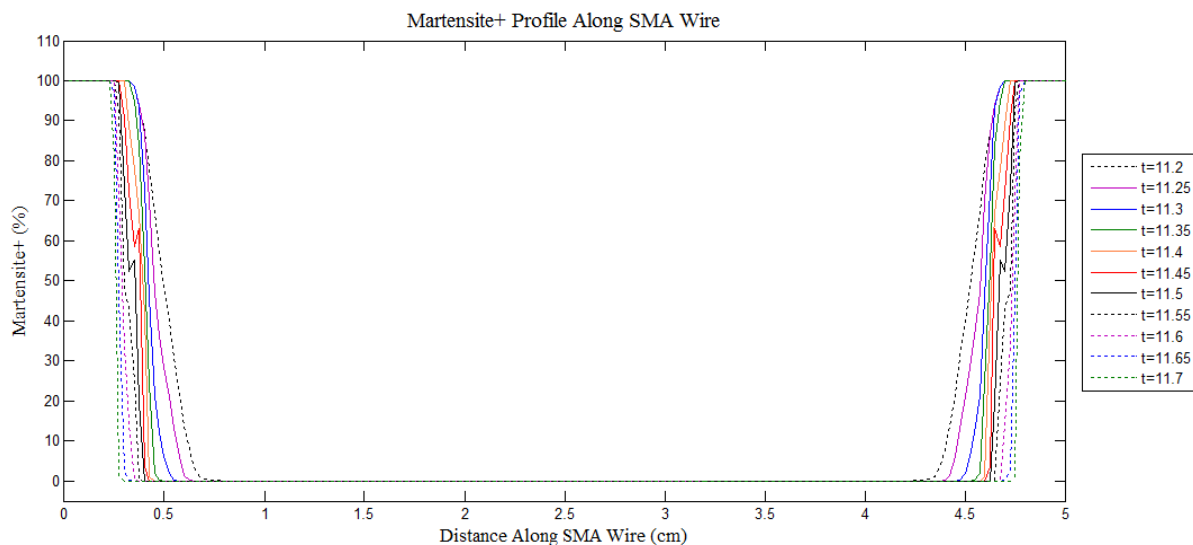


Figure 57: Evolution of martensite+ along the length of the SMA wire from $t=11.2-11.7$ s.

When power is gradually released from $t=12$ to 15 s the temperature along the wire decreases and approaches the temperature at the ends of the wire. A decrease in temperature results in a

decrease in austenite and an increase in martensite+, which also results in an increase in strain and a decrease in stress.

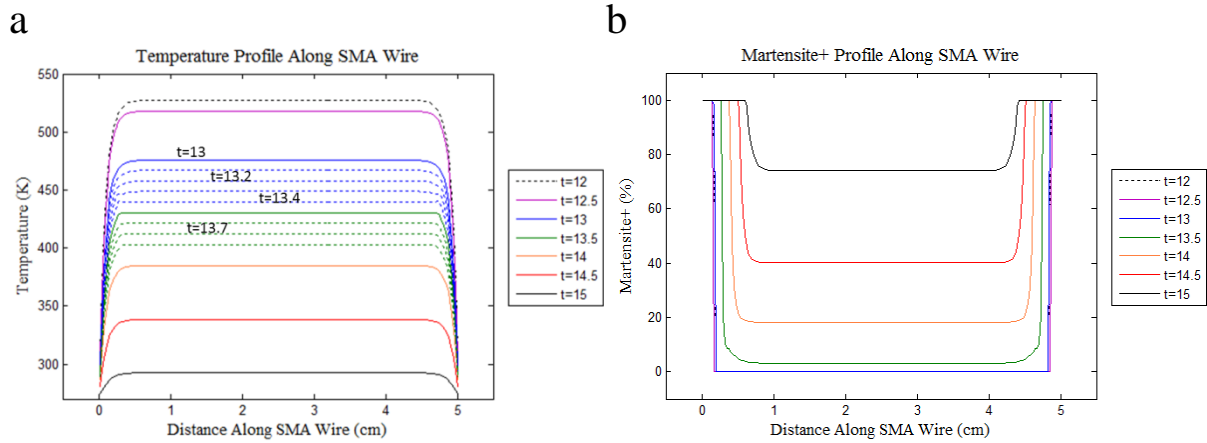


Figure 58: Evolution of (a) temperature and (b) martensite+ along the length of the SMA wire from t=12-15s for isothermal boundary conditions.

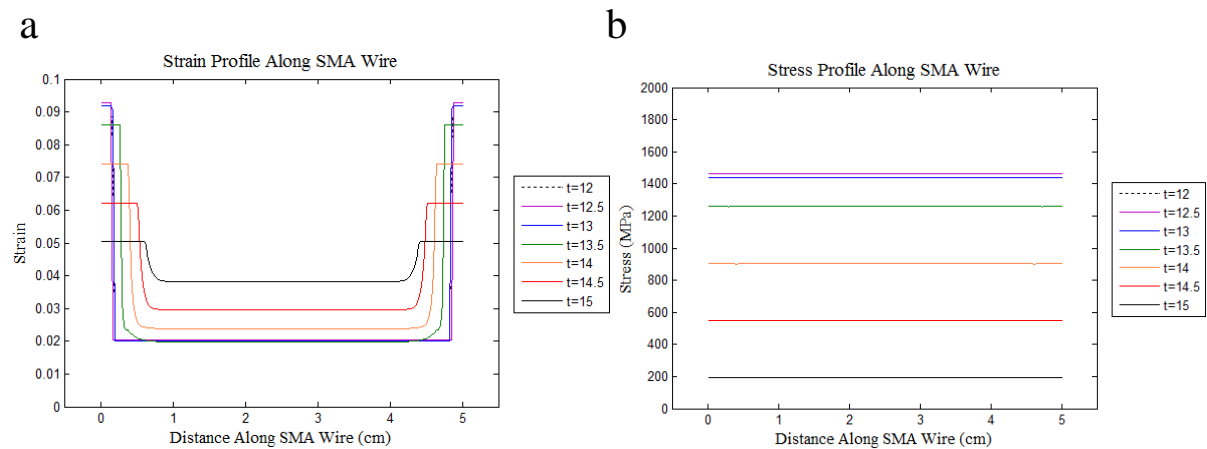


Figure 59: Evolution of (a) strain and (b) stress along the length of the SMA wire from t=12-15s for isothermal boundary conditions.

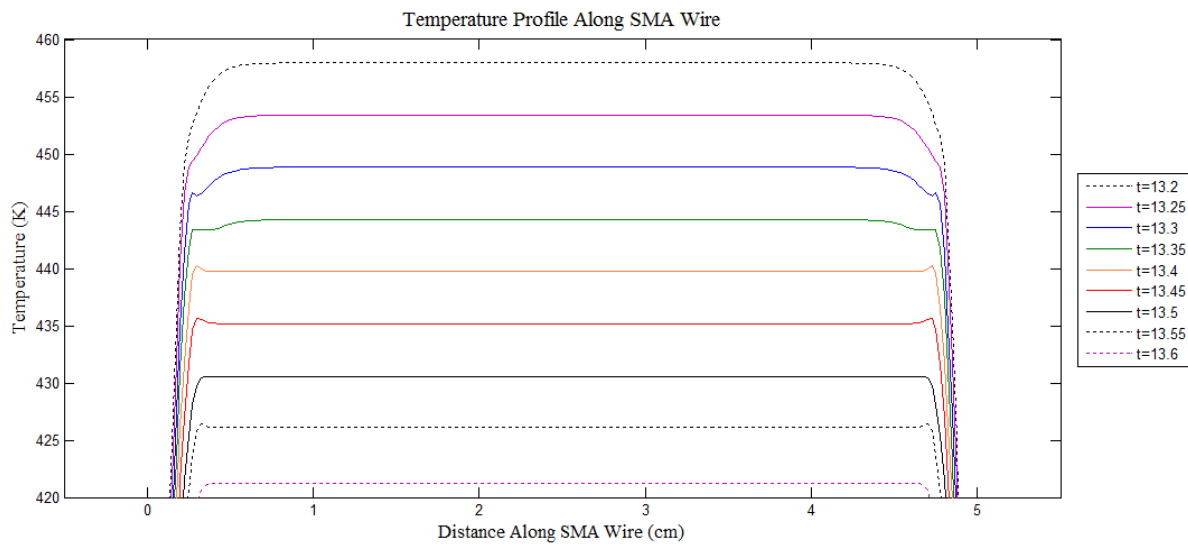


Figure 60: Evolution of temperature along the length of the SMA wire from $t=13.2$ - 13.6 s.

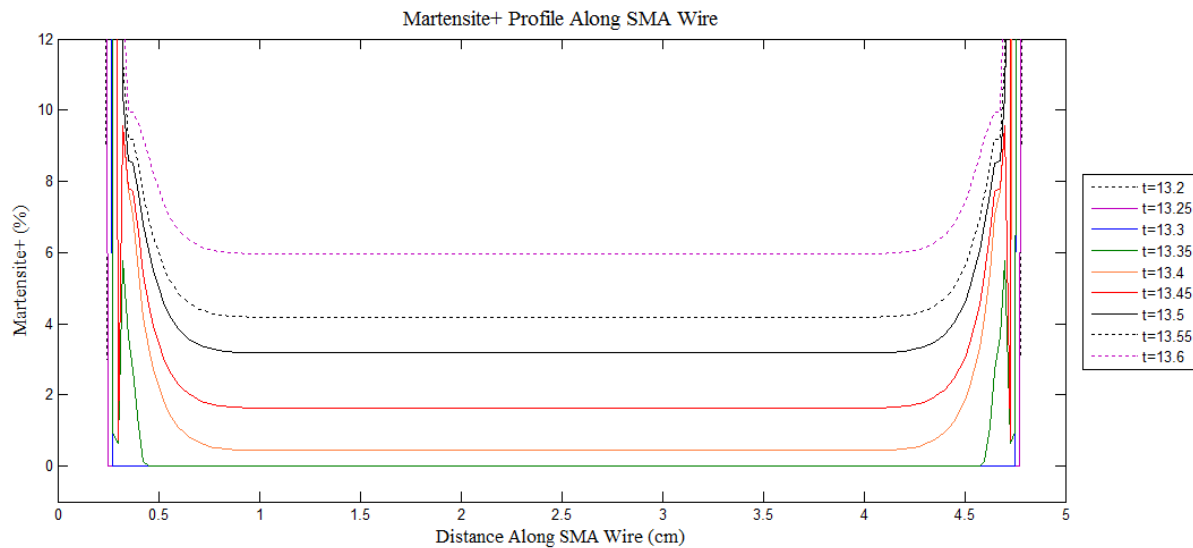


Figure 61: Evolution of martensite+ along the length of the SMA wire from $t=13.2$ - 13.6 s.

3.2.2.4 Results: Comparison

In order to analyze the differences between homogeneous and inhomogeneous temperature profiles, the adiabatic and isothermal results from this simulation were compared to the homogeneous temperature profile results from Appendix B. The differences in displacement are graphed together and shown in Figure 62 below.

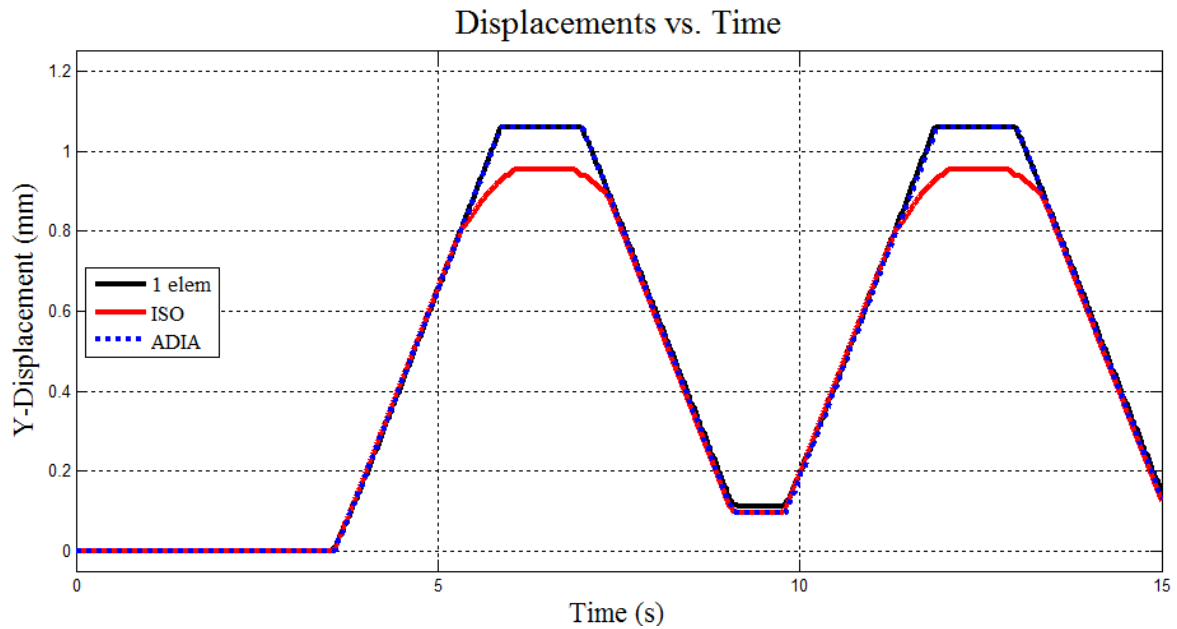


Figure 62: Displacement comparison of an actuated SMA wire attached to a spring with homogeneous and inhomogeneous temperature profiles.

The above graph compares the displacement of a single wire element attached to a spring (black line) against an inhomogeneous wire with adiabatic temperature boundary conditions (dotted blue line) and an inhomogeneous wire with isothermal boundary conditions (red line). All simulations were identical in geometry, material properties, and actuation. The

results show a difference in displacement between all three cases. The isothermal BC case has 0.105mm less displacement than the single element and adiabatic BC case. This difference in displacement is due to the ends of the wire with isothermal boundary conditions, which do not allow for a full transformation to austenite and thus a greater displacement. These differences in displacement, although small in this case, show that temperature boundary conditions have an effect on the performance of SMA wires and should be considered in SMA simulations. The differences in displacement between each case would vary for different SMA wire geometries due to the heating and cooling rates.

To further illustrate the effects of adiabatic and isothermal boundary conditions, a second spring simulation was performed using different SMA wire parameters. The input graph and displacement results are shown in Figure 64.

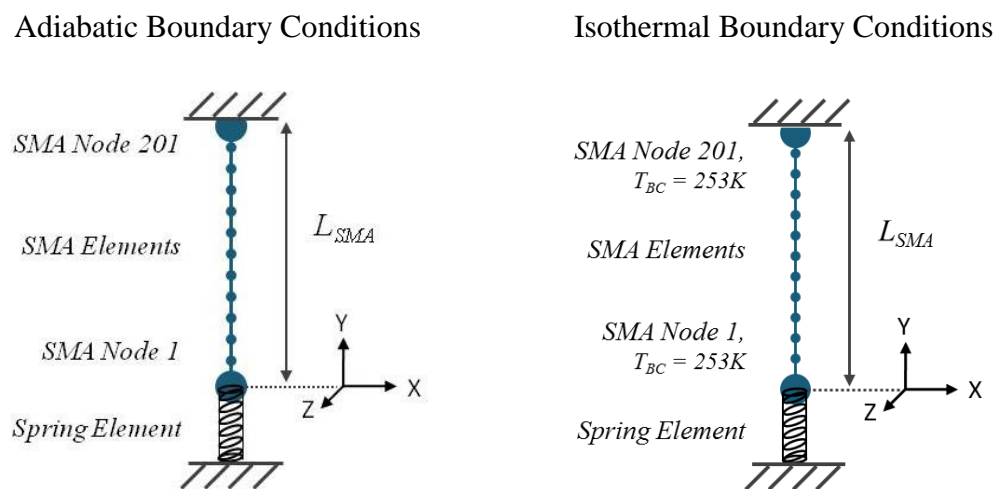
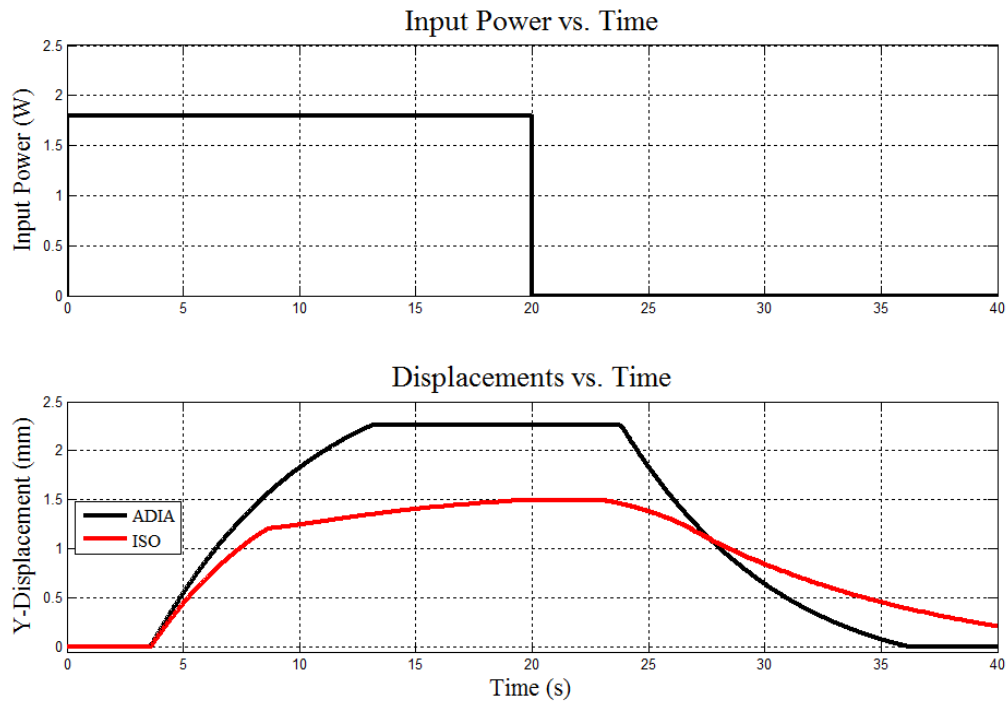


Figure 63: Simulation 6, Case 2 schematic: single SMA wire attached to a spring with actuation for adiabatic and isothermal boundary conditions.

Table 8: Simulation 6, Case 2: Initial Conditions and Model Parameters.

Parameter	Variable	Value
Spring Stiffness	k_{spring}	100.53e+03 N/m
SMA radius	r_{SMA}	4.0e-4 m
SMA length	L_{SMA}	0.06 m
Initial Condition: Martensite+	M_{+o}	100%
Initial Condition: Martensite-	M_{-o}	0%
Initial Condition: Pre-stress	σ_o	0.0 MPa
External Temperature	T_{ext}	253.0 K

**Figure 64:** Displacement comparison between adiabatic and isothermal boundary conditions.

The above graph compares the displacement of an inhomogeneous wire with adiabatic temperature boundary conditions (black line) and an inhomogeneous wire with isothermal

boundary conditions (red line). These two simulations were identical in geometry, material properties, and actuation. The results show that the SMA wire with isothermal boundary conditions case has 0.762mm (34%) less displacement than the SMA wire with adiabatic boundary conditions. This difference in displacement is due to the ends of the wire with isothermal boundary conditions, which do not allow for a full transformation to austenite and thus a greater displacement. These differences in displacement show that temperature boundary conditions have an effect on the performance of SMA wires and should be considered in SMA simulations.

These SMA wire and spring simulations show the model's ability to predict the coupled temperature-displacement behavior for an actuated SMA wire attached to a spring element with an inhomogeneous temperature profile under both adiabatic and isothermal boundary conditions.

3.2.3 Simulation 7: Dueling Wires

In this simulation, two SMA wires are joined together to show the model's ability to simulate more than 1 SMA wire with actuation under an inhomogeneous temperature profile with isothermal boundary conditions. Effects of wire coupling are also investigated.

3.2.3.1 Geometry and Parameters

In this simulation, a SMA wire is coupled with another SMA wire and both wires are alternately actuated with joule heating. Both wires have a length of 0.05m, a radius 25.0e-6m and are modeled using 100 three-dimensional, two-node, coupled temperature displacement truss elements (T3D2T) shown in Figure 65. The left end of SMA wire 1, Node 1, and the right end of SMA wire 2, Node 101, are fixed in displacement and rotation. The right end of SMA wire 1, Node 101, is connected to the left end of SMA wire 2, Node 1, via a multi-point constrain in the form of a tie. The ends of both SMA wires have isothermal boundary conditions which are set equal to the external temperature of 273K. Power is alternately supplied to actuate each wire in the form of Joule heating via a triangular waveform with an amplitude of 0.1 Watts for a total of 6 cycles. SMA wire 1 is actuated for 3 seconds and allowed to cool for 3 seconds before SMA wire 2 is actuated. The initial conditions and model parameters for the simulation are listed in Table 9 and the results from the simulation are explained in the Results section below.

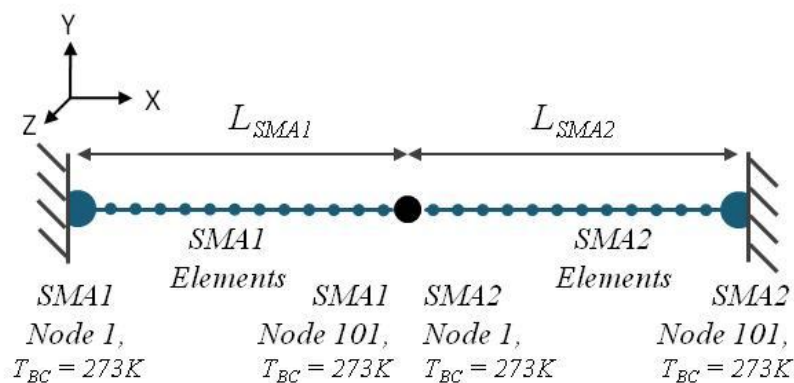
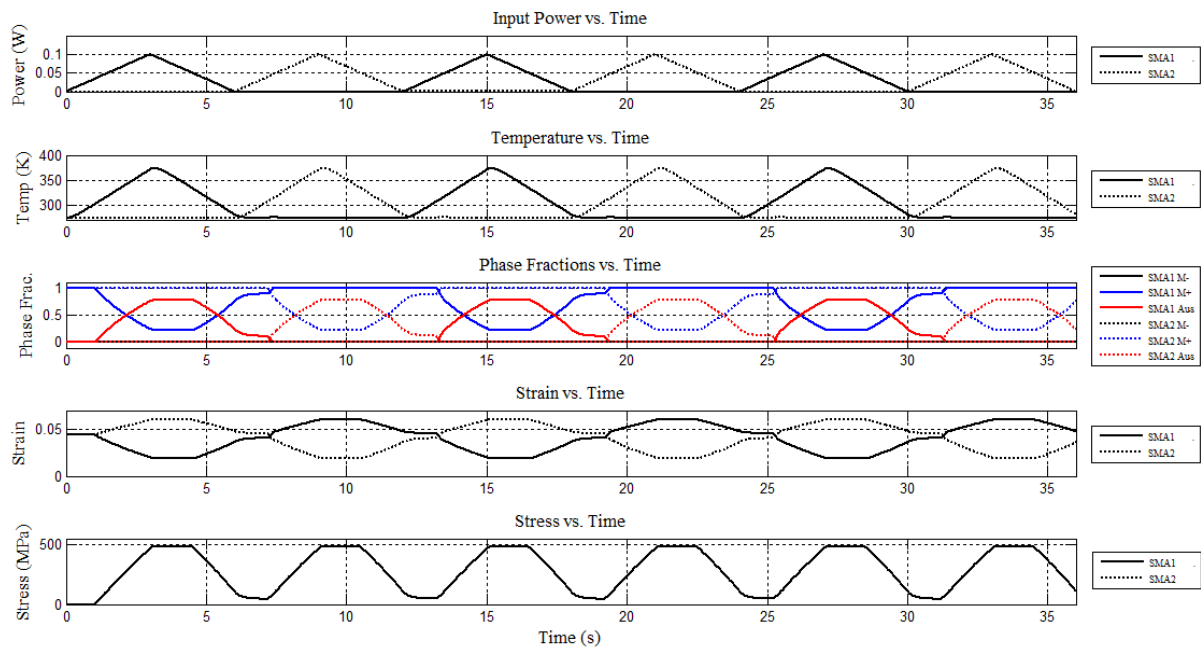


Figure 65: Simulation 7 Schematic: Two SMA wires attached to each other with actuation.

Table 9: Simulation 7: Initial Conditions and Model Parameters.

Parameter	Variable	SMA 1 Value	SMA 2 Value
SMA radius	r_{SMA}	25.0e-6 m	25.0e-6 m
SMA length	L_{SMA}	0.05 m	0.05 m
Initial Condition: Martensite+	M_{+o}	100%	100%
Initial Condition: Martensite-	M_{-o}	0%	0%
Initial Condition: Pre-stress	σ_o	0.0 MPa	0.0 MPa
External Temperature	T_{ext}	273.0 K	273.0 K

3.2.3.2 Results

**Figure 66:** Time resolved power input to two SMA actuators and corresponding temperature, phase fractions, strain and stress responses.

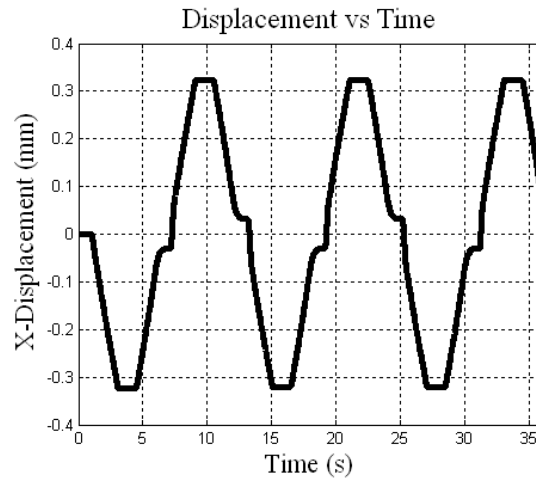


Figure 67: Displacement of the SMA wire connection point versus time response.

Both SMA wires are initially in 100% martensite with 4.4% (0.0 MPa of pre-stress). The isothermal boundary conditions on each end of both SMA wires are set constant to the external temperature of 273K. When power is gradually applied to each SMA wire in the first graph it causes changes in the temperature, phase fractions, strain, and stress in the following graphs versus time for each SMA wire. Due to the inhomogeneous profiles along each wire, the data in Figure 66 was obtained from the middle element of each SMA wire. Profiles along the entire wires are shown in Figures 68-77 for $t=12-18s$. When SMA wire 1 is gradually heated to 0.1W from $t=0$ to 3s, the internal temperature of its middle element rises above the martensite to austenite transformation temperature to 373.5K. The middle element of SMA wire 1 begins to transform from 100% martensite+ and, in this simulation, the middle element settles at 77.19% austenite and 22.81% martensite+. The change in phase fractions causes a direct decrease in strain in the middle element from 4.4% to 1.898%, which in turn causes SMA wire 2 to increase in strain from 4.4% to 6.016%. The point where the two wires are tied together displaces from 0.0mm to 0.3231mm in the negative X

direction, as shown in Figure 67. The stress-strain relationship from Eq (7) causes both wires to reach a maximum stress value of 485.0 MPa. When the joule heating is gradually released from SMA wire 1 during $t=3$ to 6s, the temperature of the wire decreases to the external temperature of 273K and drops below the austenite to martensite transformation temperature. At this temperature, SMA wire 1 begins transforming back to martensite+. The phase fractions at the end of transformation for the middle element are 75.25% martensite+ and 24.75% austenite, which correspond to strain values of 3.624% and 4.766% in SMA wire 1 and wire 2, respectively. The point where the wires are tied together displaces 0.24799mm in the positive X direction at -0.07311mm. Both wires decrease in stress to a value of 110.0MPa.

When 0.1W of power is gradually supplied to SMA wire 2 from $t=6$ to 9s, the same sequence of wire heating and transformation occurs as in SMA wire 1. In addition, the same effects that were seen in SMA wire 2 when SMA wire 1 was heated are now seen in SMA wire 1 when SMA wire 2 is heated.

The following figures illustrate the evolution of the temperature, martensite+, strain, and stress profiles along both wires during the heating and cooling of SMA wire 1 from $t=12$ to 18s. The graphs show the effects of isothermal temperature boundary conditions on the ends of the SMA wire. The solid lines represent SMA wire 1 and the dashed lines represent SMA wire 2. As power is supplied to SMA wire 1, the temperature in the center of SMA wire 1

increases beyond the temperature at the wire's ends. As a result, the transition from martensite+ to austenite in SMA wire 1 occurs proportionally with the change in the wire's temperature. The amount of martensite+ and austenite along the wire directly results in changes in the strain and stress along the wire. In addition, as SMA wire 1 decreases in strain it causes an increase in strain in SMA wire 2 and a corresponding increase in martensite+. As SMA wire 2 increases in strain and martensite+ from austenite, it experiences latent heats as a result of phase transformation, which is shown in Figure 72.

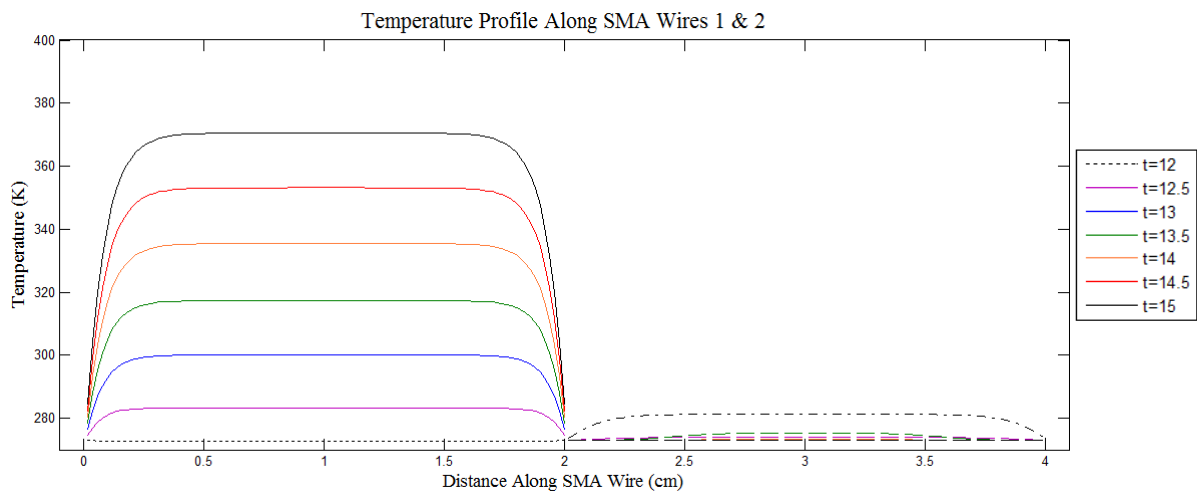


Figure 68: Evolution of temperature along the length of SMA wires 1 and 2 from $t=12$ - 15 s.

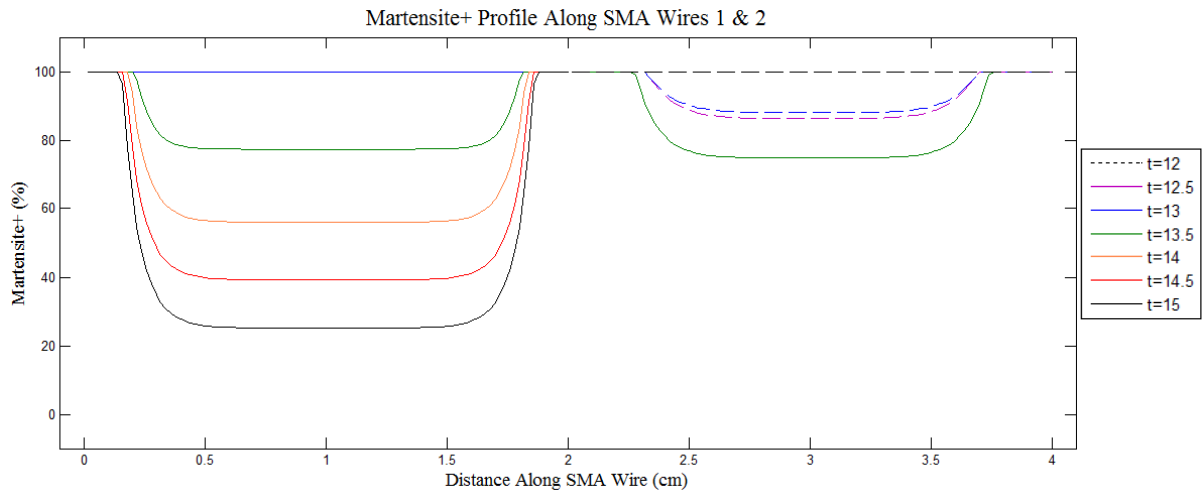


Figure 69: Evolution of martensite+ along the length of SMA wires 1 and 2 from t=12-15s.

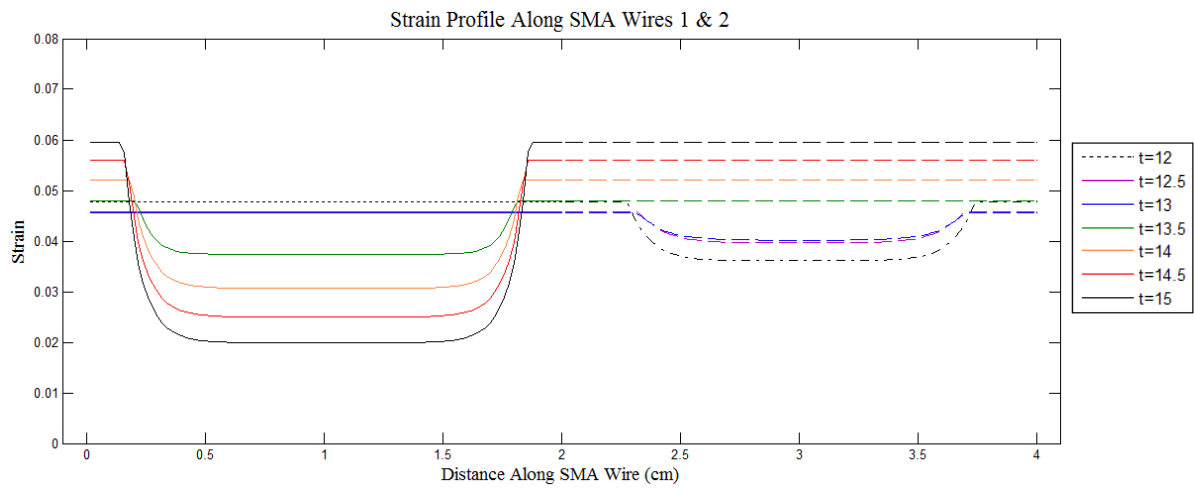


Figure 70: Evolution of strain along the length of SMA wires 1 and 2 from t=12-15s.

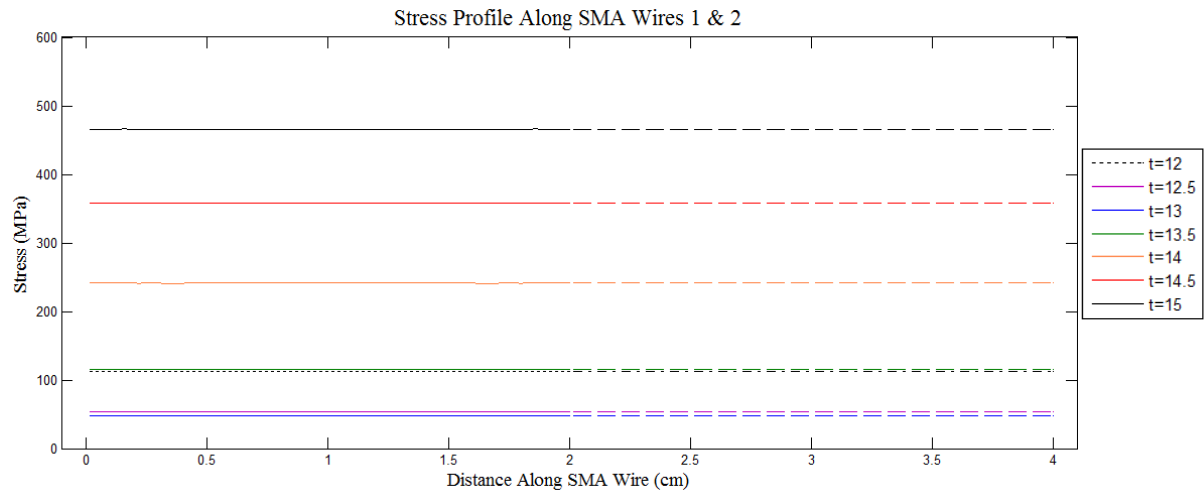


Figure 71: Evolution of stress along the length of SMA wires 1 and 2 from $t=12-15$ s.

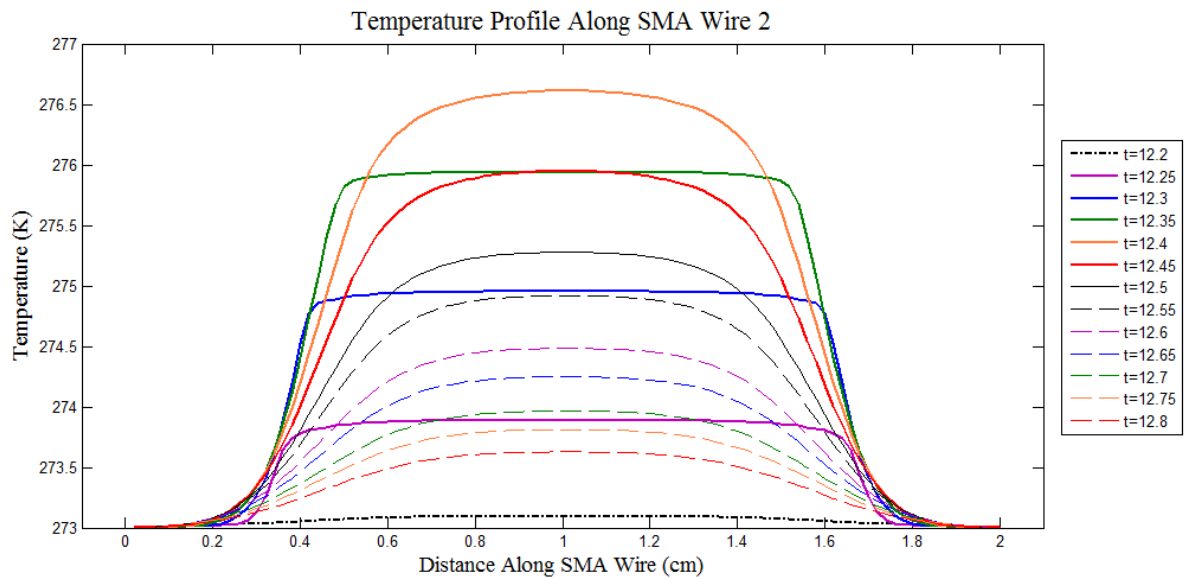


Figure 72: Evolution of latent heats as a result of phase transformation occurring in SMA wire 2 from $t=12-13$ s.

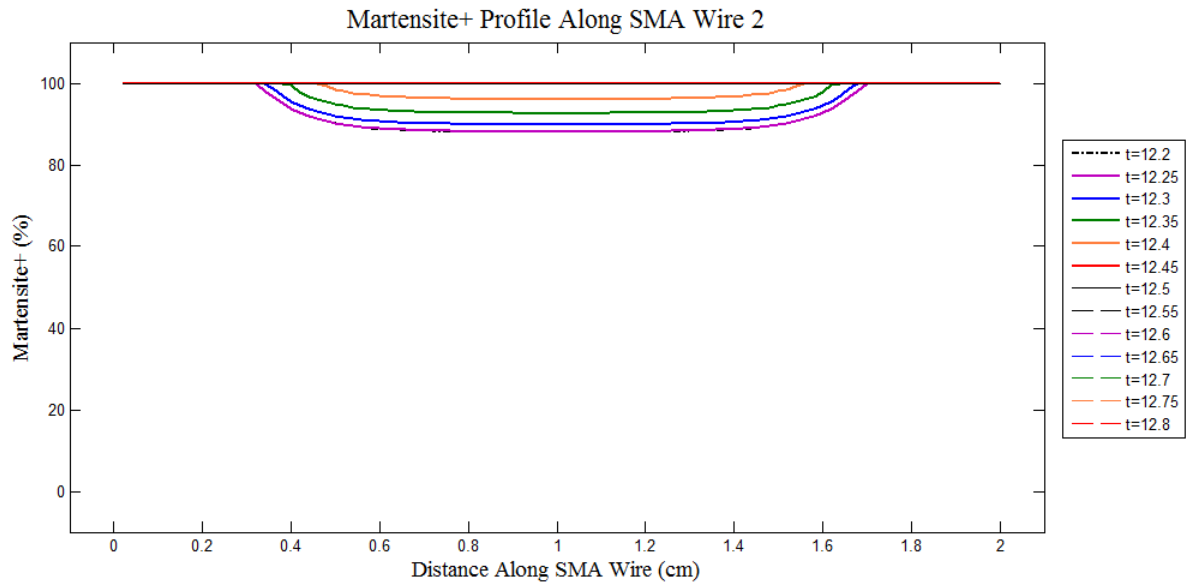


Figure 73: Evolution of martensite+ as a result of phase transformation occurring in SMA wire 2 from t=12-13s.

When power is gradually released from SMA wire 1 during t=15 to 18s, the temperature along the wire decreases and approaches the temperature at the ends of the wire. A decrease in temperature results in a decrease in austenite and an increase in martensite+, which also results in an increase in strain and a decrease in stress. Wire coupling from SMA wire 2 also assists in the increase in strain in SMA wire 1.

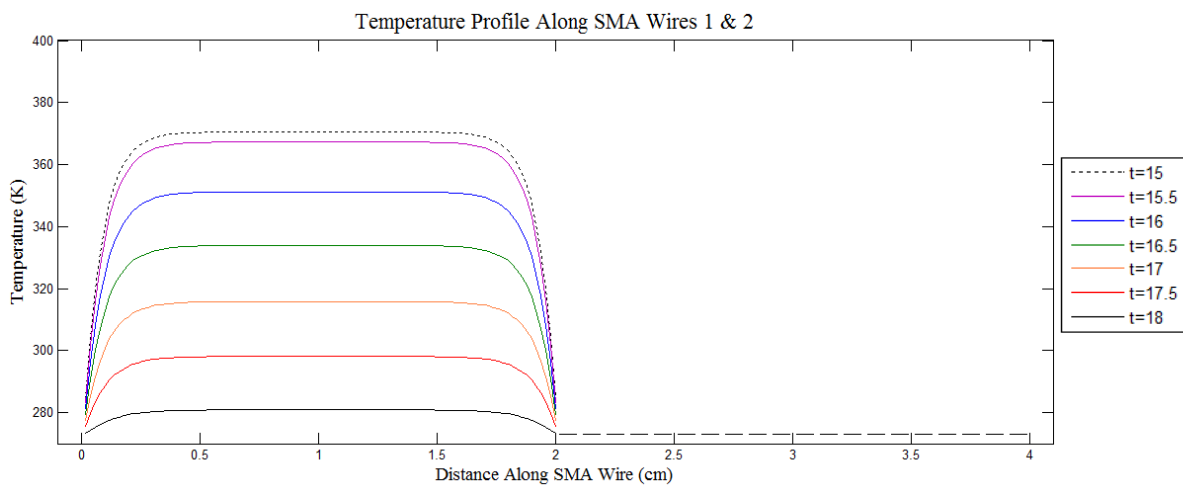


Figure 74: Evolution of temperature along the length of SMA wires 1 and 2 from t=15-18s.

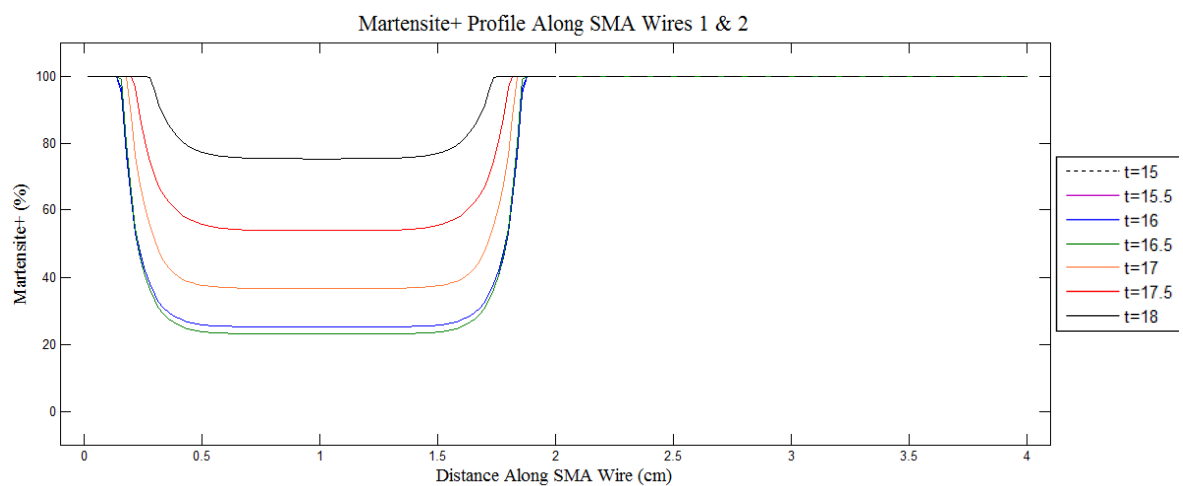


Figure 75: Evolution of martensite+ along the length of SMA wires 1 and 2 from t=15-18s.

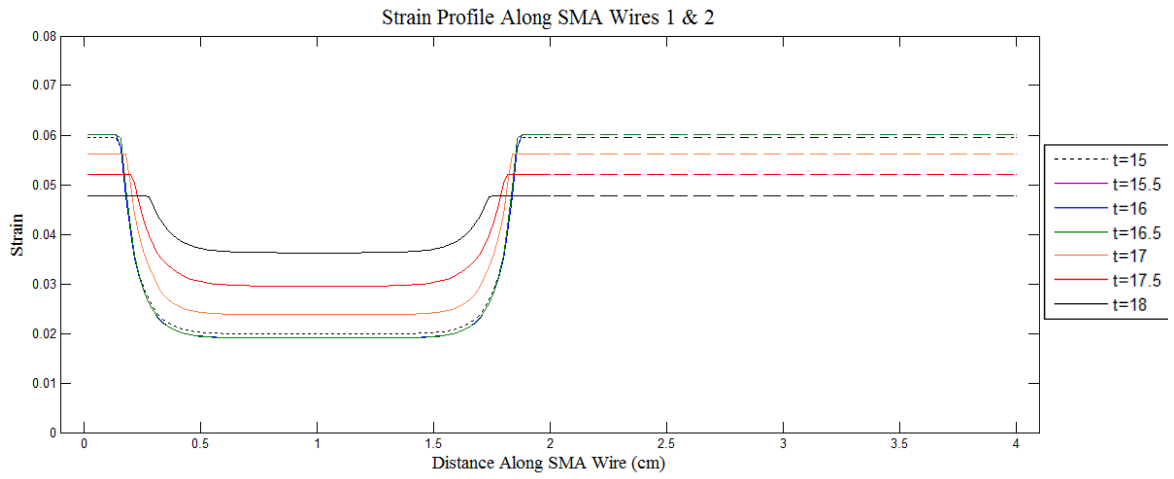


Figure 76: Evolution of strain along the length of SMA wires 1 and 2 from t=15-18s.

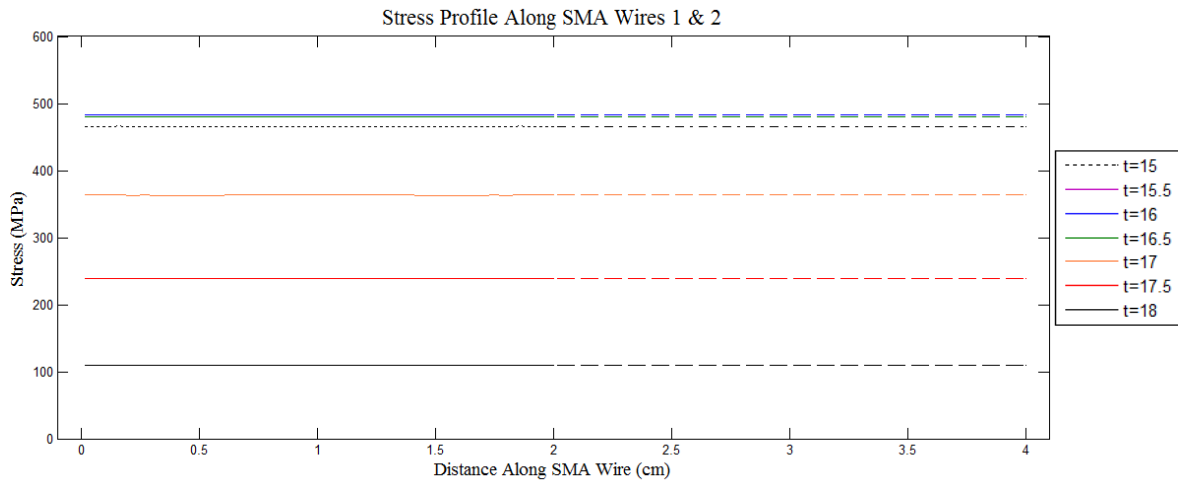


Figure 77: Evolution of stress along the length of SMA wires 1 and 2 from t=15-18s.

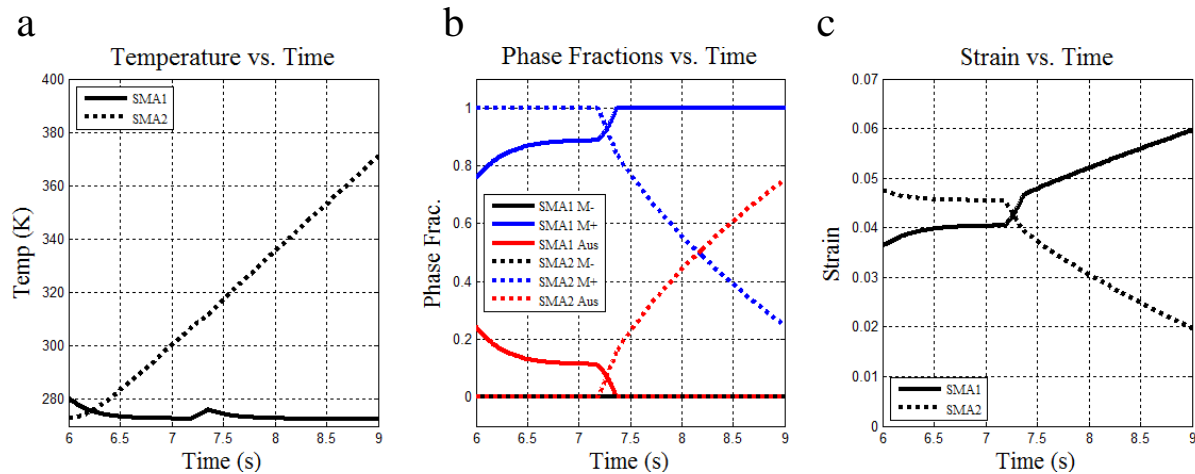


Figure 78: Second order effects due to wire coupling. a) Temperature versus time, b) phase fractions versus time, c) strain versus time for $t=6-9s$.

In this simulation with two SMA wires second order effects are observed due to wire coupling, as shown in Figure 78. Effects of wire coupling in this simulation are best observed during the actuation of SMA wire 1 between $t=6$ and $9s$. After SMA wire 1 was actuated, it returned to 75% martensite+ and 3.6% strain instead of 100% M+ and 4.4% strain which it experienced at the beginning of the simulation. In order to return to 100% martensite+, an external tensile force must be applied to SMA wire 1 to increase its strain and cause a full transformation to martensite+. When SMA wire 2 is actuated from $t=6$ to $9s$, its decrease in strain causes additional tension to be applied to SMA wire 1. As a result, SMA wire 1 increases in strain from 3.6% to 6.0%, enough to fully transform it back into 100% M+ as seen in Figures 78b and 78c. In addition, latent heats of transformation for SMA wire 1 are visible in the temperature versus time plot at $t=7.35s$ in Figure 78a. The same types of secondary effects are seen in SMA wire 2 when SMA wire 1 is actuated.

This simulation shows the model's ability to predict the coupled temperature-displacement behavior for a multi-SMA wire simulation with actuation and inhomogeneous temperature profiles under isothermal boundary conditions.

3.2.4 Simulation 8: SMA Wire and Elastic Beam

This next simulation also implements the same SMA model described in Chapter 2 for inhomogeneous temperature, phase fraction, strain and stress profiles along the SMA wire with both adiabatic and isothermal boundary conditions. The fourth simulation increases in complexity by coupling the SMA wire with a stiff, 3-D elastic beam structure and observing the effects of wire actuation. The resulting temperature, phase fractions, strain, stress, and displacements versus time are investigated.

3.2.4.1 Geometry and Parameters

In this simulation, a SMA wire is coupled with a stiff, 3-D beam and actuated with joule heating. The SMA wire has a length of 0.05m, a radius 25.0e-6m and is modeled using 200 three-dimensional, two-node, coupled temperature displacement truss elements (T3D2T) shown in Figure 79. The elastic beam has a length of 0.01m, a circular cross-section with a radius of 0.001m and is modeled using 20 three-dimensional beam elements (B31). The top of the SMA wire, SMA Node 201, is fixed in displacement and rotation and the bottom of the SMA wire, SMA Node 1, is tied to the left end of the beam, Beam Node 1, via a multi-point

constrain in the form of a tie. The right end of the beam, Beam Node 21, is fixed in displacement and rotation. Power is cyclically supplied to the wire in the form of Joule heating in a triangular waveform with an amplitude of 0.64 Watts for 2 cycles to actuate the SMA wire. The initial conditions and model parameters for the simulation are listed in Table 10 and the results from the simulation are explained in the Results section below.

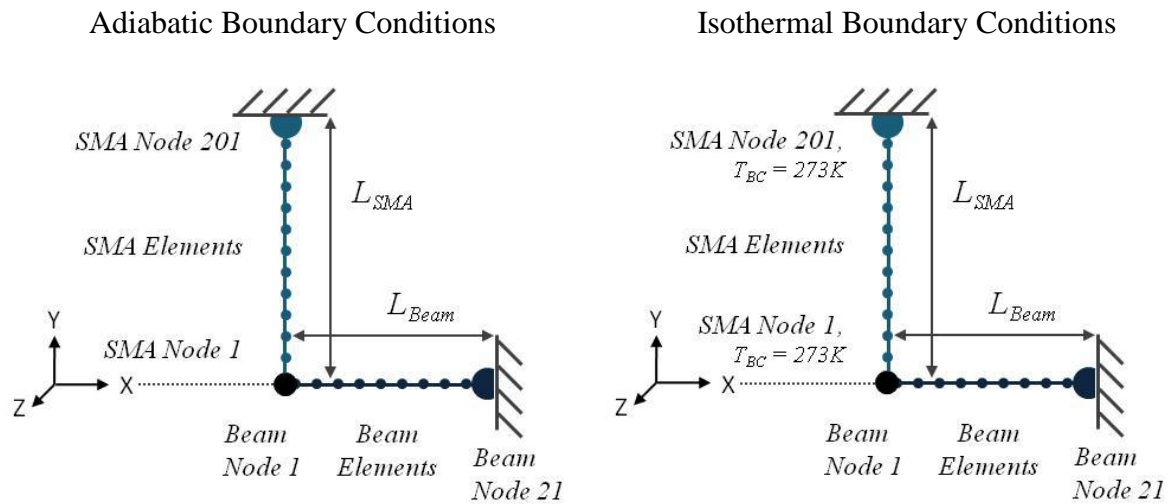


Figure 79: Simulation 8 schematic: SMA wire coupled with a 3-D elastic beam for adiabatic and isothermal boundary conditions.

Table 10: Simulation 8: Initial Conditions and Model Parameters.

Parameter	Variable	Value
SMA radius	r_{SMA}	25.0e-06 m
SMA length	L_{SMA}	0.05 m
Initial Condition: Martensite+	M_{+o}	100%
Initial Condition: Martensite-	M_{-o}	0%
Initial Condition: Pre-stress	σ_o	0.0 MPa
Beam radius	r_{Beam}	0.001 m
Beam length	L_{Beam}	0.01 m
Beam elastic modulus	E_{Beam}	1.0e+09 Pa
Beam Poisson's Ratio	ν_{Beam}	0.3
External Temperature	T_{ext}	273.0 K

3.2.4.2 Results: Adiabatic Boundary Conditions

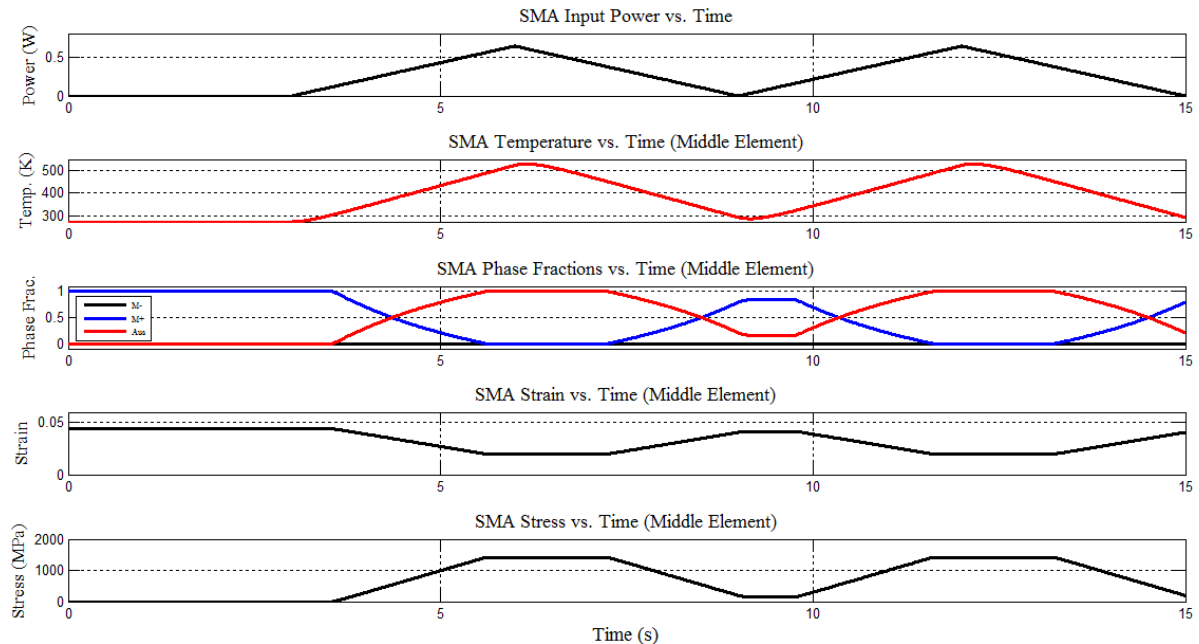


Figure 80: Time resolved power input to SMA actuator and corresponding temperature, phase fractions, strain and stress responses for adiabatic boundary conditions.

The SMA wire is initially strained to 4.4% with 0.0 MPa of pre-stress and in 100% martensite+. The temperature boundary conditions on both ends of the SMA wire are adiabatic. When power is gradually applied to the SMA wire in the first graph it causes changes in the SMA wire temperature, phase fractions, strain, and stress in the following graphs versus time. Due to the inhomogeneous profile, the data in Figure 80 above was taken from the SMA wire's middle element. Profiles along the entire wire are shown in Figures 83-86 for $t=9-15$ s. When the wire is gradually heated to 0.64W from $t=3$ to 6s, the internal temperature of the SMA rises above the martensite to austenite transformation temperature and reaches 529.9K. The wire begins to transform from 100% martensite+ and, in this

simulation, completely transforms into austenite. The change in phase fractions causes a direct decrease in strain from 4.4% to 1.99%, which in turn causes a change in displacement of the wire end from 0.0mm to 1.205mm in the +Y direction, as shown in Figure 81. The stress-strain relationship from Eq (7) causes the wires to reach a maximum stress value of 1415 MPa. When the joule heating is gradually released at $t=6s$, the temperature of the wire decreases and drops below the austenite to martensite transformation temperature. At this temperature, the wire begins transforming back to martensite+. The phase fractions at the end of transformation are 83.93% martensite+ and 16.07% austenite, which correspond to a strain value of 4.145% and a stress value of 149.6 MPa. When power is supplied to the SMA wire again at $t=9s$, the same sequence of wire heating and transformation occurs. The SMA stress versus strain and strain versus temperature responses are graphed in Figure 82.

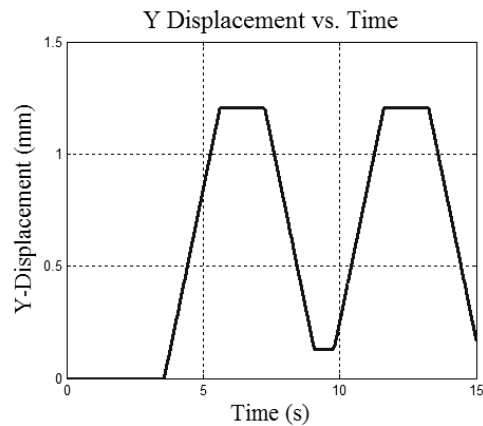


Figure 81: SMA wire tip displacement versus time response for adiabatic boundary conditions.

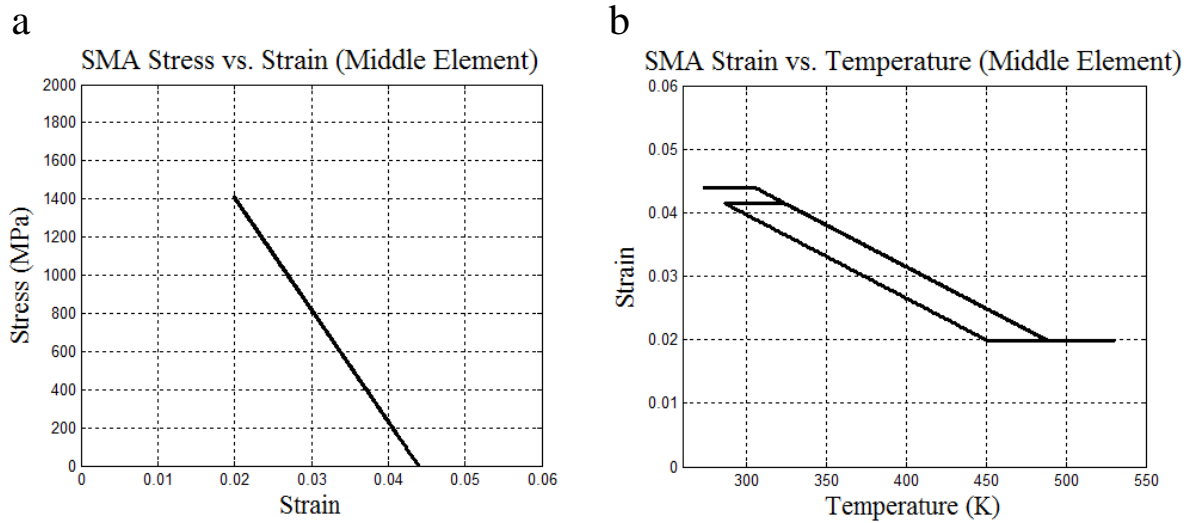


Figure 82: (a) Stress versus strain and (b) strain versus temperature relationships for adiabatic boundary conditions.

The following figures illustrate the evolution of the temperature, martensite+, strain, and stress profiles along the SMA wire during actuation from $t=9$ to 15s. The graphs show the effects of adiabatic temperature boundary conditions on the ends of the SMA wire. As power is supplied to the SMA wire from $t=9$ to 12s, the temperature in the center of the wire increases along with the temperature at the wire's ends. As a result, the transition from martensite+ to austenite in the SMA wire occurs uniformly along the wire with the change in the wire's temperature. The amount of martensite+ and austenite along the wire directly results in changes in the strain and stress along the wire.

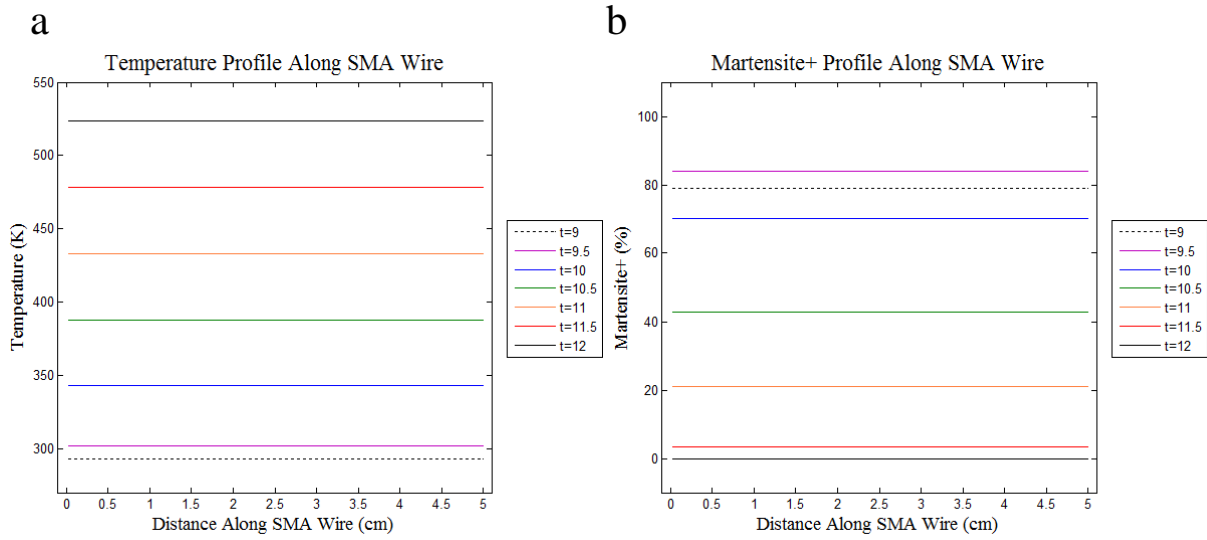


Figure 83: Evolution of (a) temperature and (b) martensite+ along the length of the SMA wire from $t=9$ - 12 s for adiabatic boundary conditions.

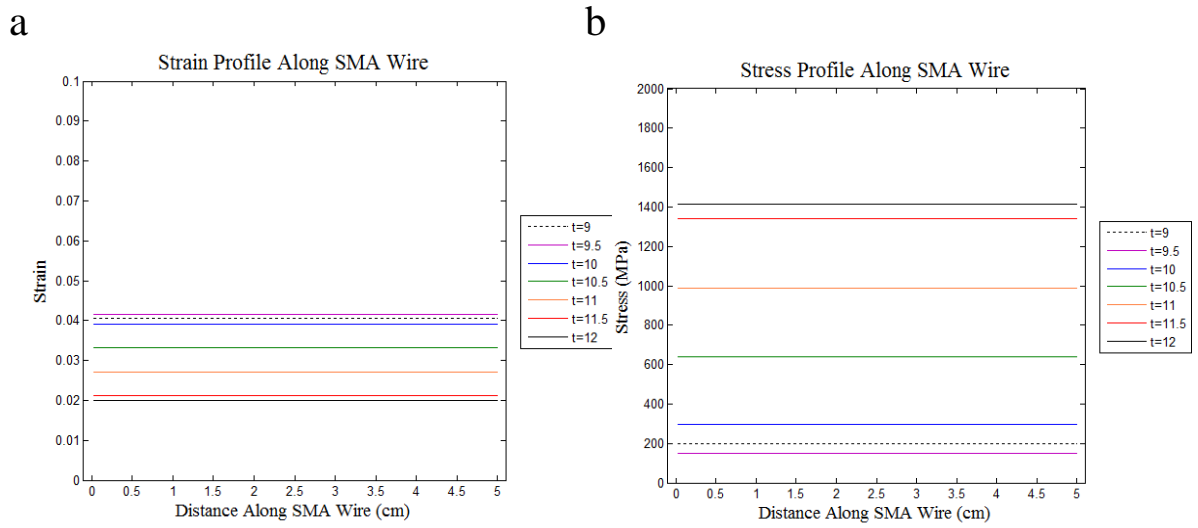


Figure 84: Evolution of (a) strain and (b) stress along the length of the SMA wire from $t=9$ - 12 s for adiabatic boundary conditions.

When power is gradually released from the SMA wire during $t=12$ to 15 s, the temperature along the wire decreases uniformly along the length of the wire as a result of the adiabatic boundary conditions. A decrease in temperature results in a decrease in austenite and an increase in martensite+, which also results in an increase in strain and a decrease in stress.

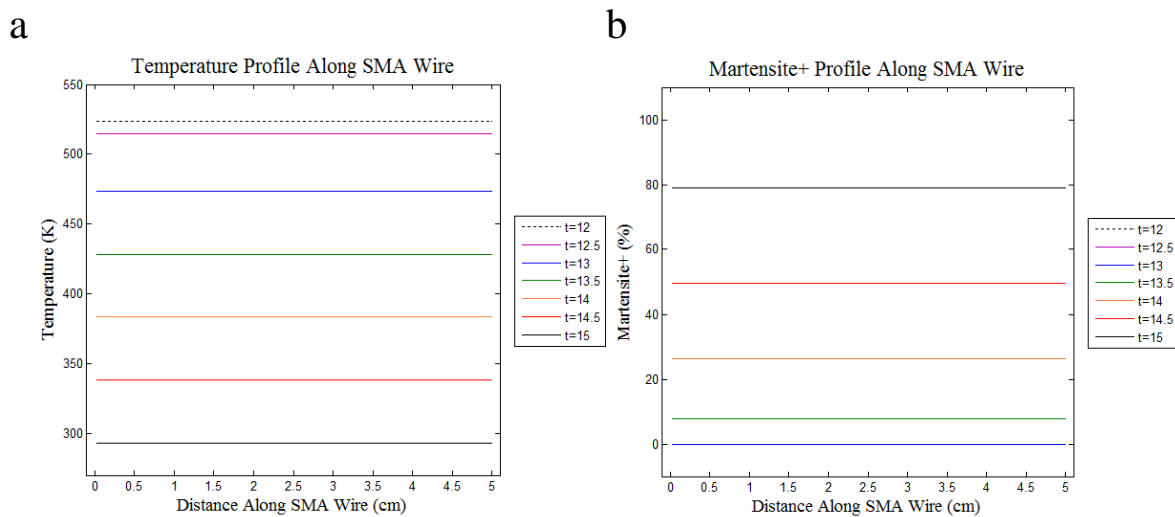


Figure 85: Evolution of (a) temperature and (b) martensite+ along the length of the SMA wire from $t=12$ - 15 s for adiabatic boundary conditions.

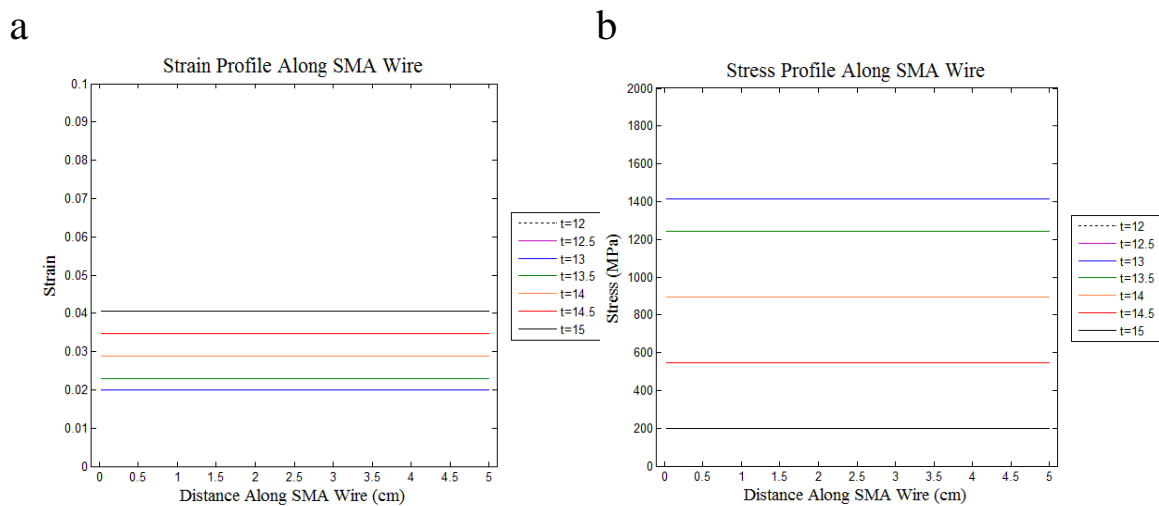


Figure 86: Evolution of strain and stress along the length of the SMA wire from $t=12$ - 15 s for adiabatic boundary conditions.

3.2.4.3 Results: Isothermal Boundary Conditions

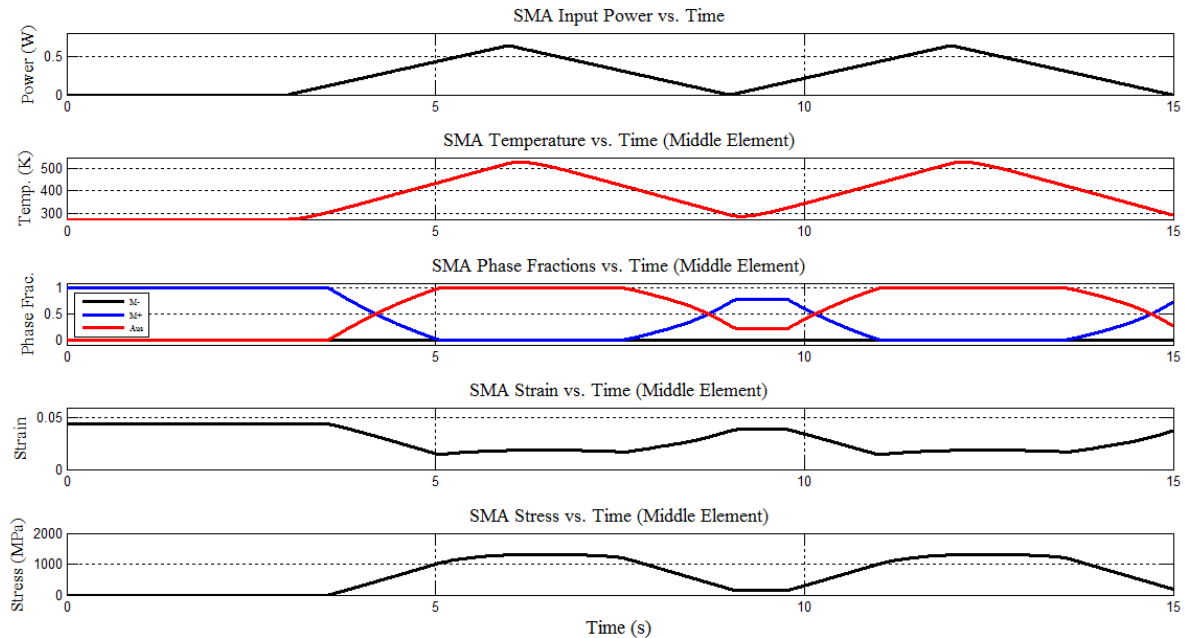


Figure 87: Time resolved power input to SMA actuator and corresponding temperature, phase fractions, strain and stress responses for isothermal boundary conditions.

The SMA wire is initially strained to 4.4% with 0.0 MPa of pre-stress and in 100% martensite+. The temperature boundary conditions on both ends of the SMA wire are isothermal and set equal to the external temperature of 273K. When power is gradually applied to the SMA wire in the first graph it causes changes in the SMA wire temperature, phase fractions, strain, and stress in the following graphs versus time. Due to the inhomogeneous profile, the data in Figure 87 above was taken from the SMA wire's middle element. Profiles along the entire wire are shown in Figures 90-97 for $t=9-15$ s. When the wire is gradually heated to 0.64W from $t=3$ to 6s, the internal temperature of the middle element in the SMA rises above the martensite to austenite transformation temperature to 529.6K. The wire begins to transform starting in its middle from 100% martensite+ and, in

this simulation with isothermal boundary conditions at each of the wire's end, the middle element transforms completely to austenite. The change in phase fractions causes a direct decrease in strain in the middle element from 4.4% to 1.834%, which in turn causes a change in displacement of the wire end from 0.0mm to 1.11mm, as shown in Figure 88. The stress-strain relationship from Eq (7) causes the wires to reach a maximum stress value of 1304.0 MPa. When the joule heating is gradually released at $t=6s$, the temperature of the wire decreases and drops below the austenite to martensite transformation temperature. At this temperature, the wire begins transforming back to martensite+. The phase fractions at the end of transformation for the middle element are 78.64% martensite+ and 21.36% austenite, which correspond to a strain value of 3.884% and a stress value of 145.1 MPa. When power is supplied to the SMA wire at $t=9s$, the same sequence of wire heating and transformation occurs again. The SMA stress versus strain and strain versus temperature responses are graphed in Figure 89.

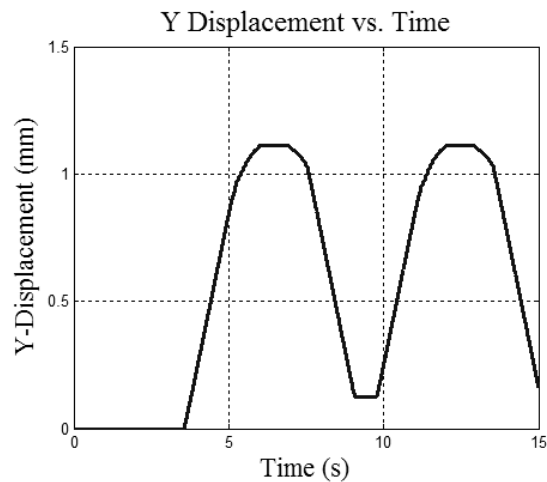


Figure 88: SMA Wire tip displacement versus time response for isothermal boundary conditions.

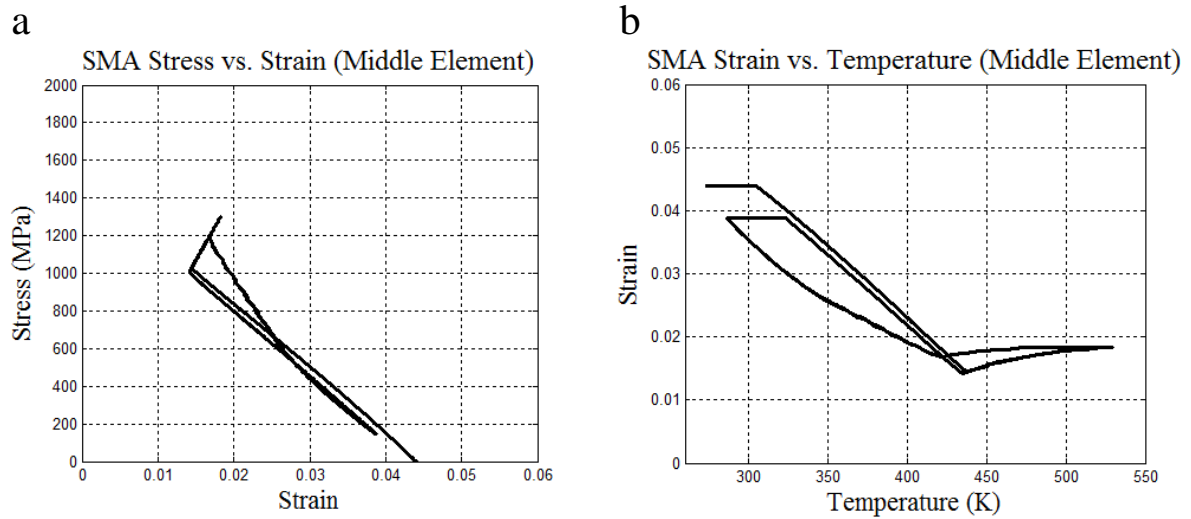


Figure 89: (a) Stress versus strain and (b) strain versus temperature relationships for isothermal boundary conditions.

The following figures illustrate the evolution of the temperature, martensite+, strain, and stress profiles along the SMA wire during the heating and cooling from $t=9$ to 15s. The graphs show the effects of isothermal temperature boundary conditions on the ends of the SMA wire. As power is supplied to the SMA wire, the temperature in the center of the wire increases beyond the temperature at the ends of the wire. As a result, the transition from martensite+ to austenite in the SMA wire occurs proportionally with the change in the wire's temperature. The amount of martensite+ and austenite along the wire directly results in changes in the strain and stress along the wire.

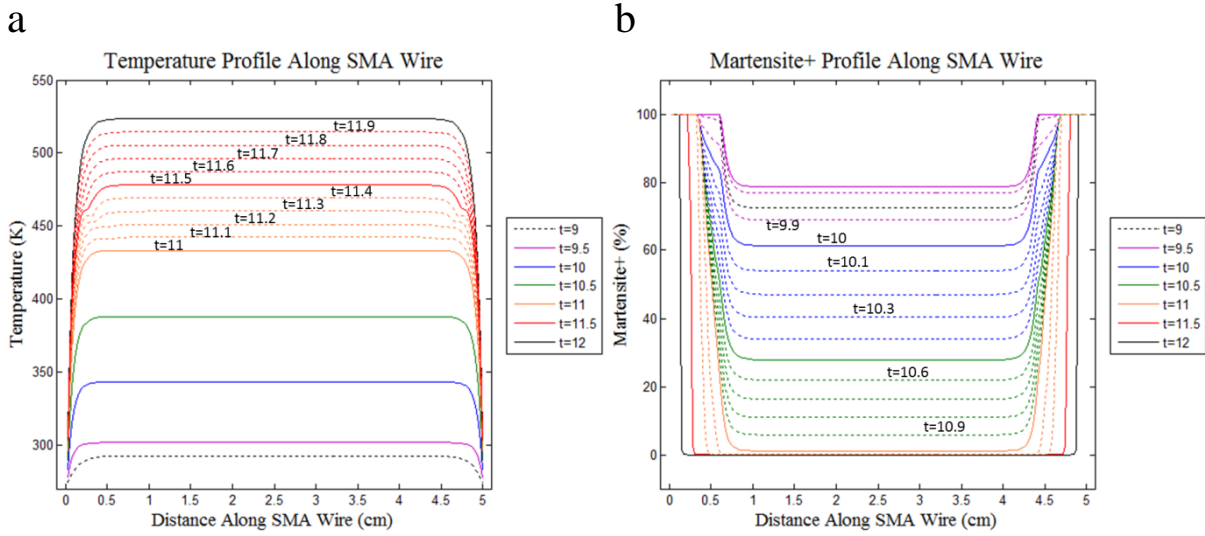


Figure 90: Evolution of (a) temperature and (b) martensite+ along the length of the SMA wire from t=9-12s for isothermal boundary conditions.

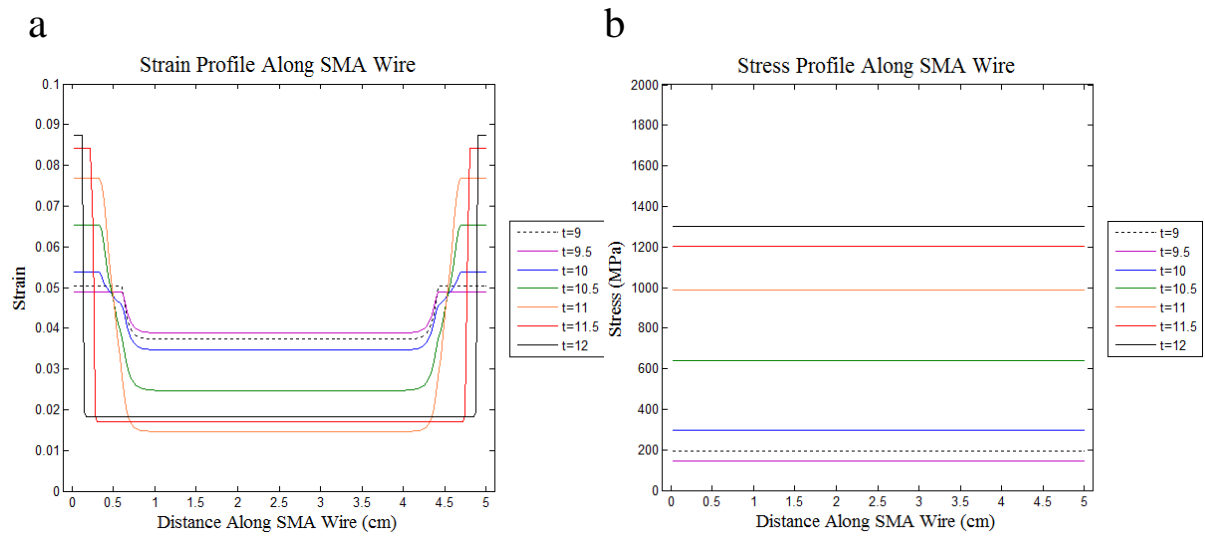


Figure 91: Evolution of (a) strain and (b) stress along the length of the SMA wire from t=9-12s for isothermal boundary conditions.

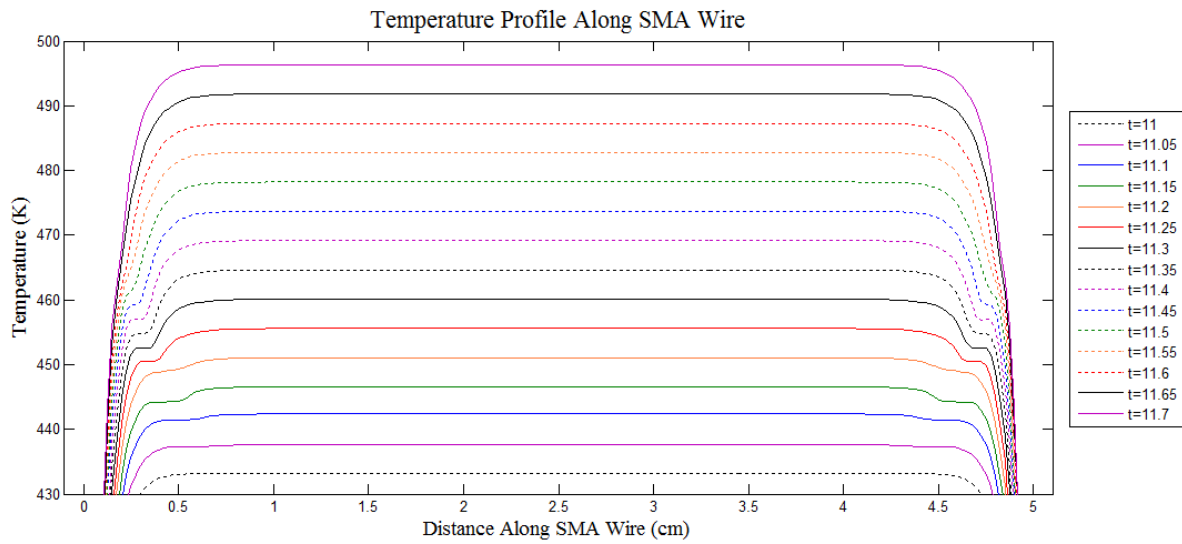


Figure 92: Evolution of temperature along the length of the SMA wire from $t=11-11.7s$.

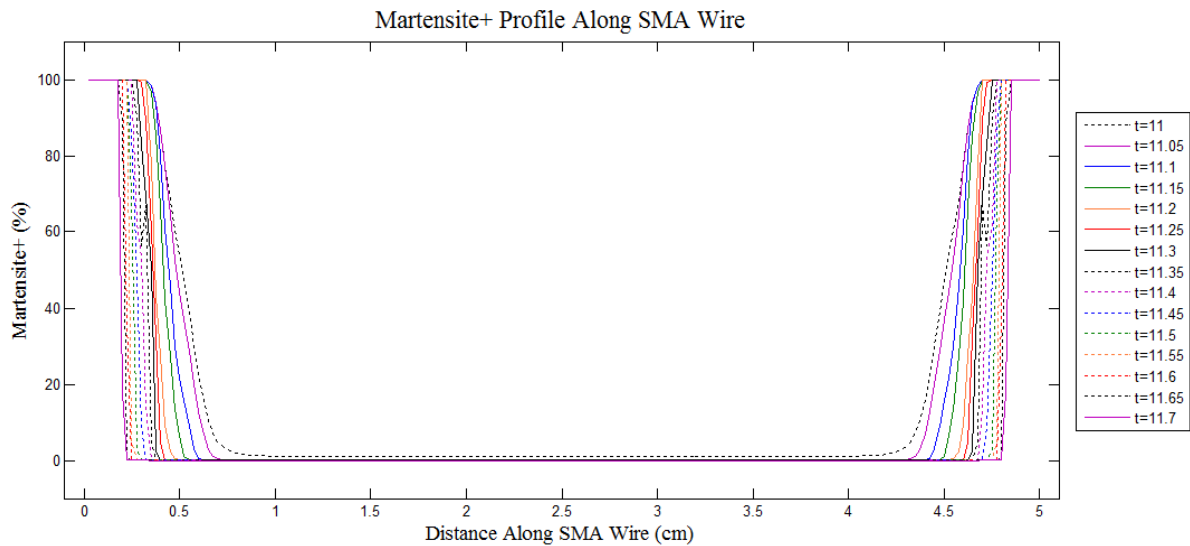


Figure 93: Evolution of martensite+ along the length of the SMA wire from $t=11-11.7s$.

When power is gradually released from the SMA wire during $t=12$ to $15s$, the temperature along the wire decreases and approaches the temperature of the ends of the wire. A decrease

in temperature results in a decrease in austenite and an increase in martensite+, which also results in an increase in strain and a decrease in stress.

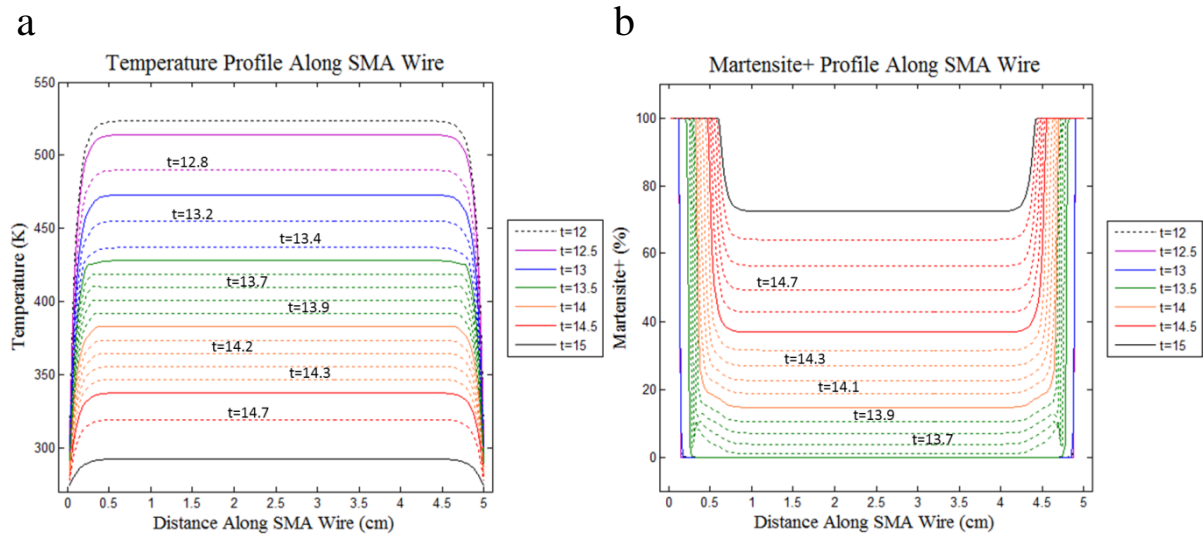


Figure 94: Evolution of (a) temperature and (b) martensite+ along the length of the SMA wire from t=12-15s for isothermal boundary conditions.

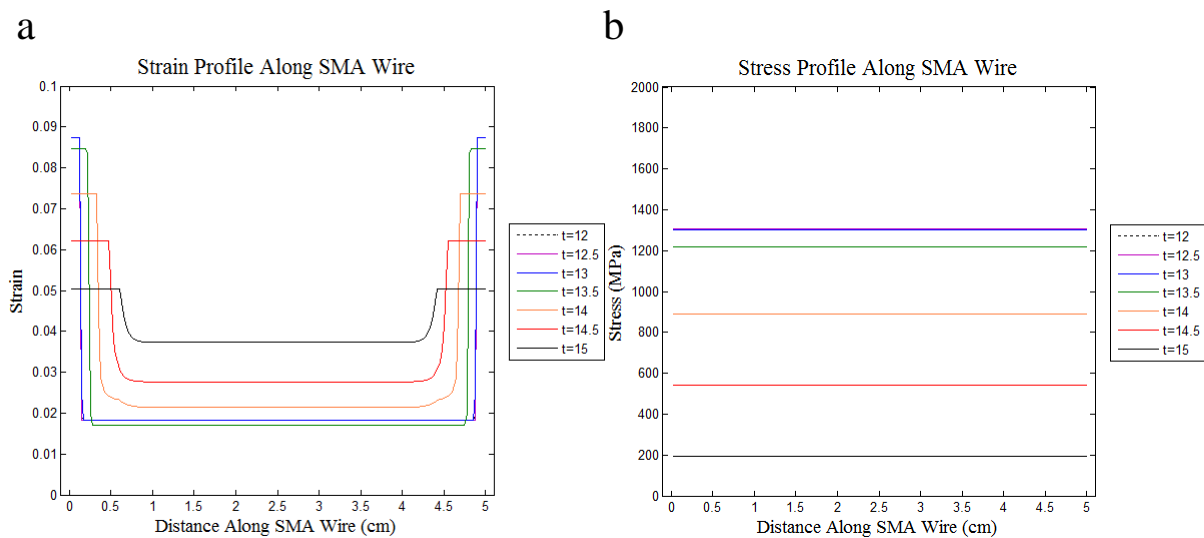


Figure 95: Evolution of (a) strain and (b) stress along the length of the SMA wire from t=12-15s for isothermal boundary conditions

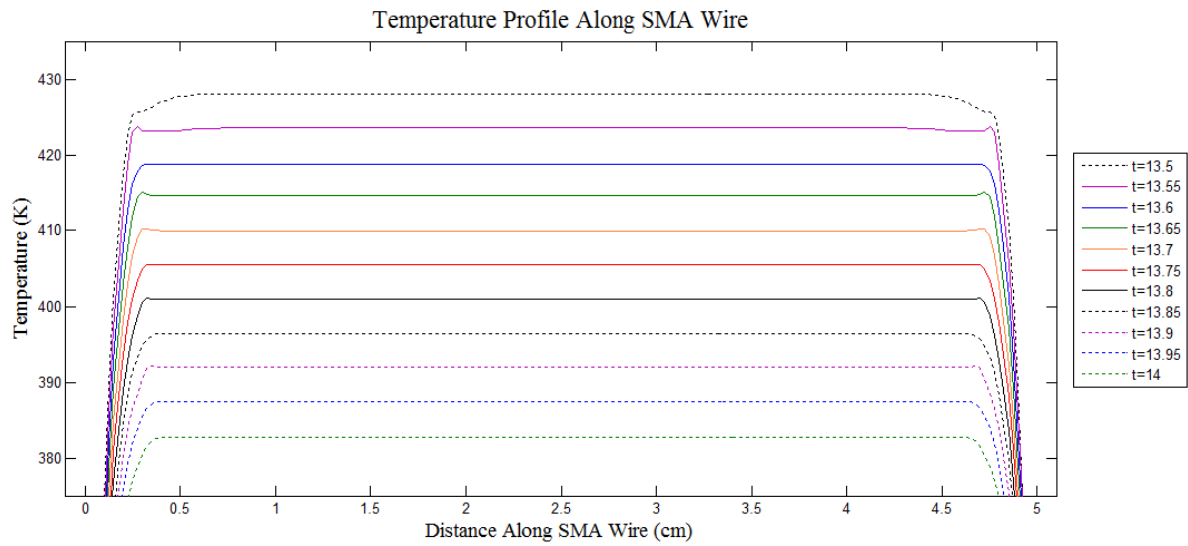


Figure 96: Evolution of temperature along the length of the SMA wire from $t=13.5$ - $14s$.

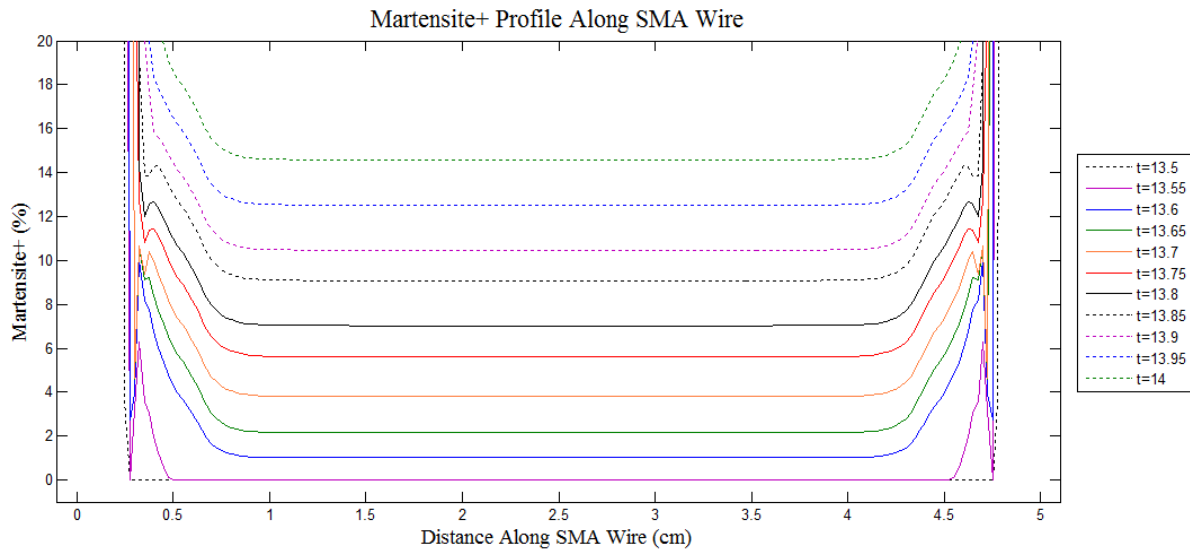


Figure 97: Evolution of martensite+ along the length of the SMA wire from $t=13.5$ - $14s$.

3.2.4.4 Results: Comparison

In order to analyze the differences between homogeneous and inhomogeneous temperature profiles, the adiabatic and isothermal results from this simulation were compared to the results from Simulation 3 with the homogeneous temperature profile. The differences in displacement are graphed together and shown in Figure 98 below.

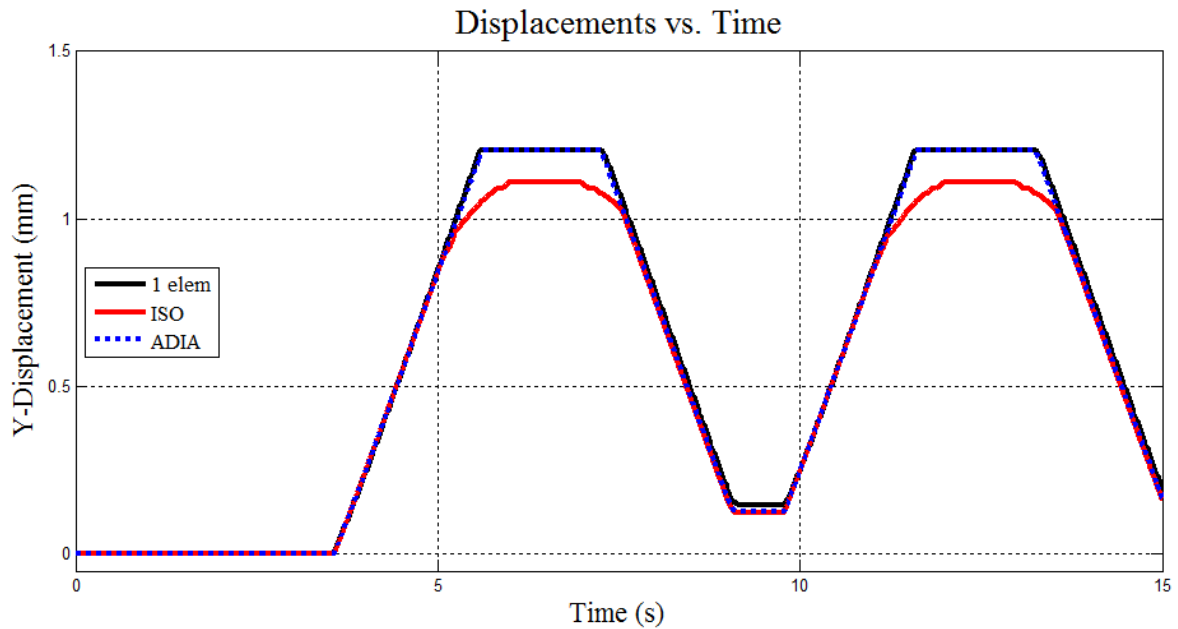


Figure 98: Displacement comparison of an SMA wire attached to an elastic beam with homogeneous and inhomogeneous temperature profiles.

The above graph compares the displacement of a single wire element attached to a beam (black line) against an inhomogeneous wire with adiabatic temperature boundary conditions (dotted blue line) and an inhomogeneous wire with isothermal boundary conditions (red line). All simulations were identical in geometry, material properties, and simulation. The

results show a difference in displacement between all three cases. The single element and adiabatic BC cases have 0.095mm more displacement than the isothermal case. This difference in displacement is due to the ends of the wire with isothermal boundary conditions, which do not allow for a full transformation to austenite and thus a decrease in strain which results in a larger displacement. These differences in displacement, although small in this case, show that temperature boundary conditions have an effect on the performance of SMA wires and should be considered in SMA simulations. The differences in displacement between each case would vary for different SMA wire geometries due to the heating and cooling rates.

This simulation shows the model's ability to predict the coupled temperature-displacement behavior for an actuated SMA wire attached to a three dimensional elastic beam with an inhomogeneous temperature profile under both adiabatic and isothermal boundary conditions.

Chapter 4

Conclusions

A thermomechanically coupled SMA actuator model was implemented into finite element software and used to simulate both single and multi-wire adaptive structures for homogeneous and inhomogeneous temperature profiles. The simulations were conducted in the finite element software ABAQUS with the SMA model incorporated via the user material option (UMAT). The physics based, mesoscopic free energy model for uniaxial stress and strain was validated against data from laboratory experiments with adaptive structures.

For simulations under homogeneous temperature profiles, a single SMA wire was cyclically actuated while coupled with a concentrated load and elastic beam. The input power, temperature, phase fractions, strain, stress and displacement of the wire tip were recorded for each simulation. A multi-wire analysis was also performed of an adaptive nozzle by actuating pairs of SMA wires, during which the input power, temperature, phase fractions, strain, and stress were recorded for each wire. The effects of structural coupling of the multi-wire system were also analyzed and validated the model's ability to predict the full behavior of adaptive structures. The nozzle tip trajectory from the simulation was compared to experimental data taken from the actual prototype. The comparison showed good agreement with the simulation matching the experimental data within 1 mm of displacement.

For inhomogeneous temperature profiles, simulations were conducted for a SMA wire with a concentrated load, a spring element, a second SMA wire and an elastic beam for both adiabatic and isothermal boundary conditions at the wires' ends. The input power, temperature, phase fractions, strain, stress and displacement of the wire tip were recorded for the middle element in each simulation. The inhomogeneous temperature, martensite+, strain and stress profiles were plotted along the length of each wire for both temperature boundary conditions. In additions, the effects of temperature boundary conditions and homogeneous profiles on wire tip displacement were analyzed. The results showed a large difference in displacement for identical simulations with different thermal boundary conditions which has a major effect on the behavior of adaptive structures. Simulations with isothermal boundary conditions experienced less wire tip displacement than those with adiabatic boundary conditions and a single wire element. Effects of latent heating and wire coupling were also observed in all simulations.

Future work will involve advancing the SMA model by investigating thermomechanical contact properties between the SMA wire(s) and structures in order to more accurately reproduce experimental conditions. In addition, electrical resistance calculations will be incorporated for sensor applications to allow for a truly multi-functional SMA model.

REFERENCES

- [1] Müller, I. and Seelecke, S., "Thermodynamic aspects of shape memory alloys," *Mathematical and Computer Modelling* 34, 1307-1355 (2001).
- [2] Tung, A.T., Park, B., Niemeyer, G. and Liang, D.H., "Laser-Machined Shape Memory Alloy Actuators for Active Catheters," *IEEE/ASME transactions on mechatronics* 12(4), 439-446 (2007).
- [3] Icardi, U. and Ferrero, L., "SMA Actuated Mechanism for an Adaptive Wing," *Journal of Aerospace Engineering* 24(1), 140-143 (2011).
- [4] Turner, T.L., Cabell, R.H., Cano, R.J. and Silcox, R.J., "Development of a Preliminary Model-Scale Adaptive Jet Engine Chevron," *AIAA Journal* 46(10), 2545-2557 (2008).
- [5] Saleeb, A.F. and Kumar, A., "Comprehensive modeling of shape memory alloy material response using a multimechanism-based inelastic model," *Journal of Aerospace Engineering* 22(4), 438-444 (2009).
- [6] Mangalgi, P.D. and Thakare, A.G., "Use of SMA constitutive model in finite element analysis of wire-based actuators," *IUTAM Symposium on Multi-Functional Material Structures and Systems*, IUTAM Bookseries 19, 45-53 (2010).
- [7] Thamburaja, P. and Nikabdullah, N., "A coupled thermo-mechanical theory for polycrystalline SMAs," *Smart Devices: Modeling of Material Systems, An International Workshop*, American Institute of Physics, 27-49 (2008).
- [8] Kleinstreuer, C., Li, Z., Basciano, C.A., Seelecke, S., and Farber, M. A., "Computational mechanics of nitinol stent grafts," *Journal of Biomechanics* 41, 2370-2378 (2008).
- [9] Vidal, N., Asua, E., Feuchtwanger, J., Garcia-Arribas, A., Gutierrez, J. and Barandiaran, J.M., "FEM simulation of the Nitinol wire," *Eur. Phys. J. Special Topics* 158, 39-44 (2008).
- [10] Peultier, B., Zineb, T.B. and Patoor, E., "A simplified micromechanical constitutive law adapted to the design of shape memory applications by finite element methods," *Materials Science and Engineering A* 481-482, 384-388 (2008).
- [11] Wang, X.M., Frotscher, M., Wang, Y.F. and Yue, Z.F., "Finite element analysis of pseudoelastic behavior of NiTi shape memory alloy with thin-wall tube under extension-torsion loading," *Journal of Material Science* 42, 2443-2449 (2007).

- [12] Bouvet, C., Calloch, S. and Lexcellent, C. "A phenomenological model for pseudoelasticity of shape memory alloys under multiaxial proportional and nonproportional loadings," *European Journal of Mechanics A/Solids* 23, 37–61 (2004).
- [13] Auricchio, F. and Taylor, R.L., "Shape-memory alloys: modelling and numerical simulations of the finite-strain superelastic behavior," *Computer Methods in Applied Mechanics and Engineering* 143, 175-194 (1997).
- [14] Auricchio, F., "A robust integration-algorithm for a finite-strain shape-memory-alloy superelastic model," *International Journal of Plasticity* 17, 971-990 (2001).
- [15] Chang, B., Shaw, J. A., and Iadicola, M. A., "Thermodynamics of shape memory alloy wire: modeling, experiments, and application," *Continuum Mechanics and Thermodynamics* 18, 83-118 (2006).
- [16] Frautschi, J. and Seelecke, S., "Finite element simulation of adaptive aerospace structures with SMA actuators," *Proc. SPIE* 5049, 65-75 (2003).
- [17] Frautschi, J.P., "Finite Element Simulation of Shape Memory Alloy Actuators in Adaptive Structures," Master's Thesis, North Carolina State University, USA (2003).
- [18] Yang, S. and Seelecke, S., "FE analysis of SMA-based bio-inspired bone-joint system," *Smart Materials and Structures* 18, 1-10 (2009).
- [19] Li, Q., "Modeling and Finite Element Analysis of Smart Materials," Ph.D. Thesis, North Carolina State University, USA (2006).
- [20] Richter, F., Kastner, O., and Eggeler, G., "Implementation of the Müller-Achenbach-Seelecke model for shape memory alloys in ABAQUS," *Journal of Materials Engineering and Performance* 18(5-6), 626-630 (2009).
- [21] Heintze, O. and Seelecke, S., "A coupled thermomechanical model for shape memory alloys—from single crystal to polycrystal," *Materials Science and Engineering A* 481–482, 389–394 (2008).
- [22] Heintze, O., "A Computationally Efficient Free Energy Model for Shape Memory Alloys—Experiments and Theory," Ph.D. Thesis, North Carolina State University, USA, (2004).
- [23] Roh, J-H. and Bae, J-S., "Thermomechanical behaviors of Ni-Ti shape memory alloy ribbons and their numerical modeling," *Mechanics of Materials* 42, 757-773 (2010).
- [24] Roh, J.-H., Han, J.-H., and Lee, I., "Nonlinear finite element simulation of shape adaptive structures with SMA strip actuator," *Journal of Intelligent Material Systems and Structures* 17, 1007–1022 (2006).

- [25] Pausley, M. E. and Seelecke, S., "Multifunctional SMA-based smart inhaler system for improved aerosol drug delivery—design and fabrication," Proc. of SPIE 6928 69280T, 1-10 (2008).
- [26] Kleinstreuer, C., and Zhang, Z., "Targeted drug aerosol deposition analysis for a four-generation lung airway model with hemispherical tumors," ASME Journal of Biomechanical Engineering 125, 197-206 (2003).
- [27] Kleinstreuer, C., Zhang, Z., Li, L., Roberts, W., and Rojas, C., "A new methodology for targeting drug-aerosols in the human respiratory system," International Journal of Heat and Mass Transfer 51, 5578–5589 (2008).
- [28] Furst, S., Hangekar, R., and Seelecke, S., "Development, assembly, and validation of an SMA-actuated two-joint nozzle and six-channel power supply for use in a smart inhaler system", Proc. SPIE 7643 76430J, 1-13 (2010).
- [29] Furst, S., personal communication, January 2011.

APPENDICES

Appendix A: Homogeneous Temperature Profile, SMA Wire with Prestress

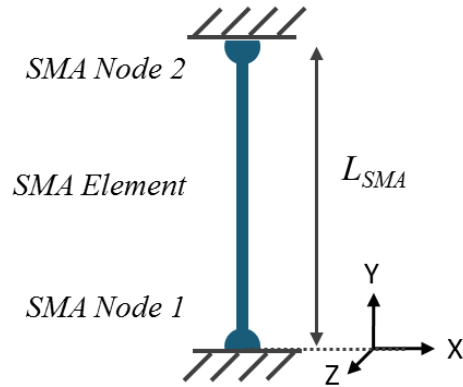


Figure 99: SMA wire with prestress schematic.

Table 11: SMA with Prestress, Initial Conditions and Model Parameters.

Parameter	Variable	Value
SMA radius	r_{SMA}	25.0e-6 m
SMA length	L_{SMA}	0.05 m
Martensite +	M+	100%
Martensite -	M-	0%
Pre-stress	σ_o	200.0 MPa
External Temperature	T_{ext}	273.0 K

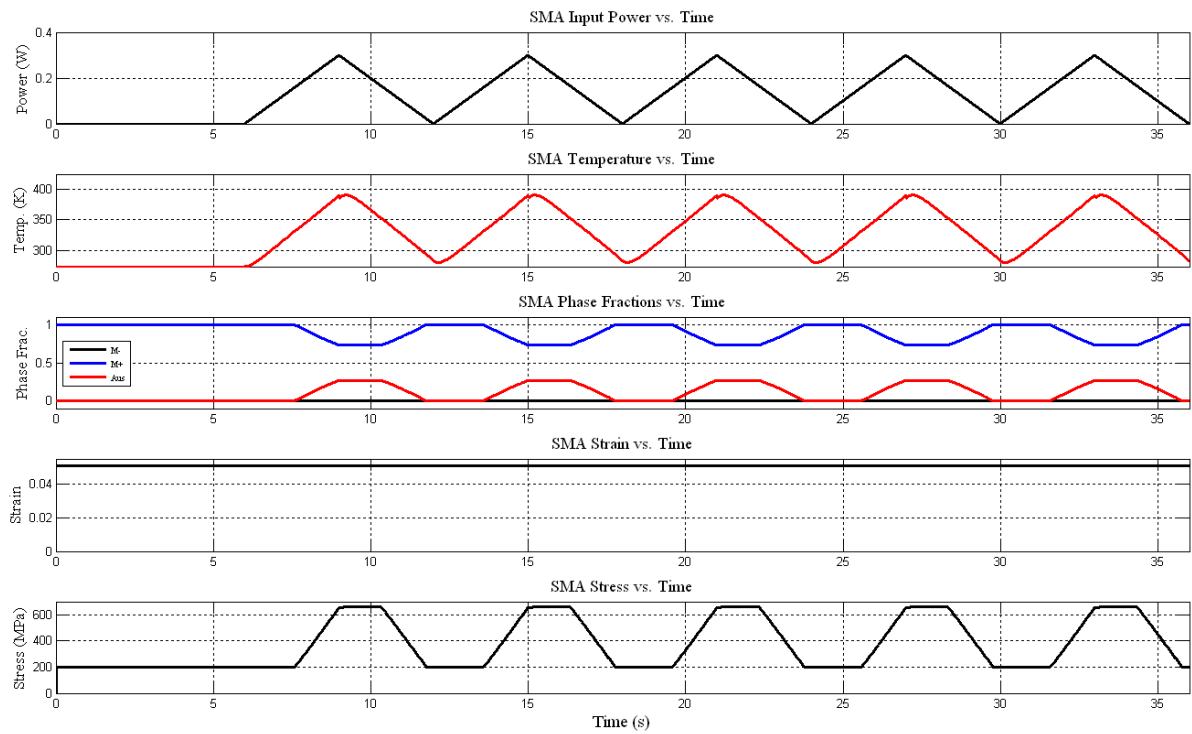


Figure 100: Time resolved concentrated load and power input to SMA actuator and corresponding temperature, phase fractions, strain and stress responses.

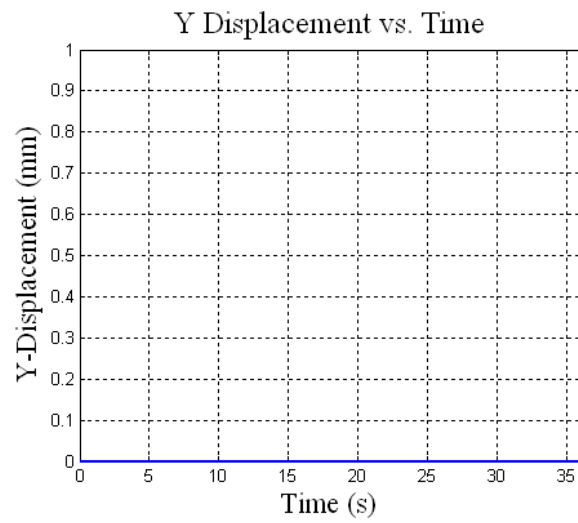
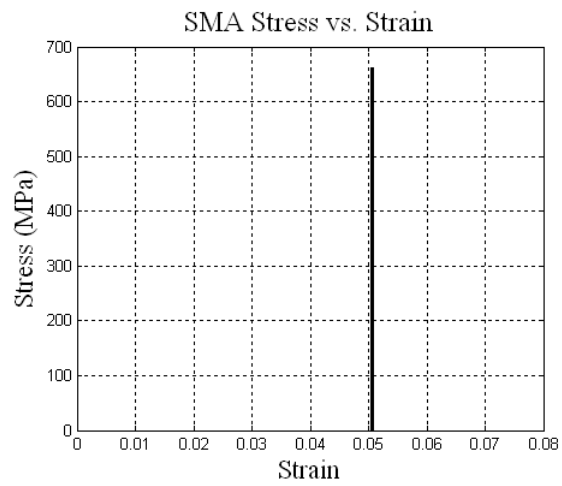


Figure 101: SMA Wire tip displacement versus time response.

a



b

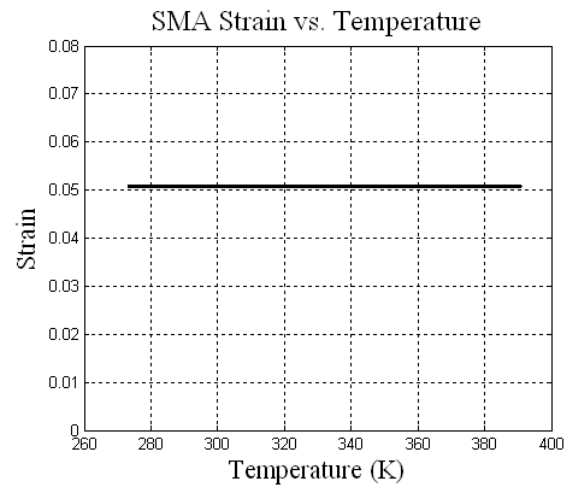


Figure 102: (a) Stress versus strain and (b) strain versus temperature relationships.

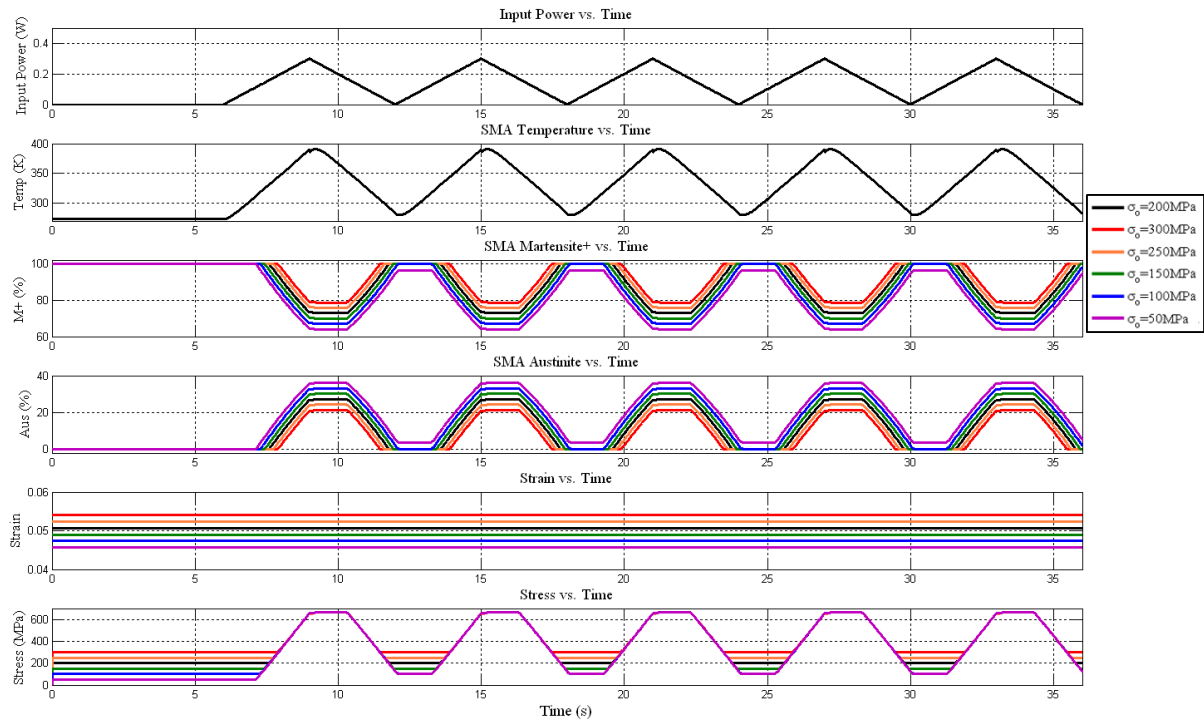


Figure 103: Time resolved power input to SMA actuator and corresponding temperature, phase fractions, strain and stress responses for different initial prestress values.

Appendix B: Homogeneous Temperature Profile, SMA Wire and Spring

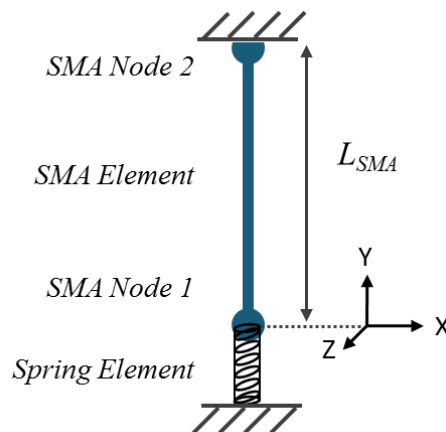
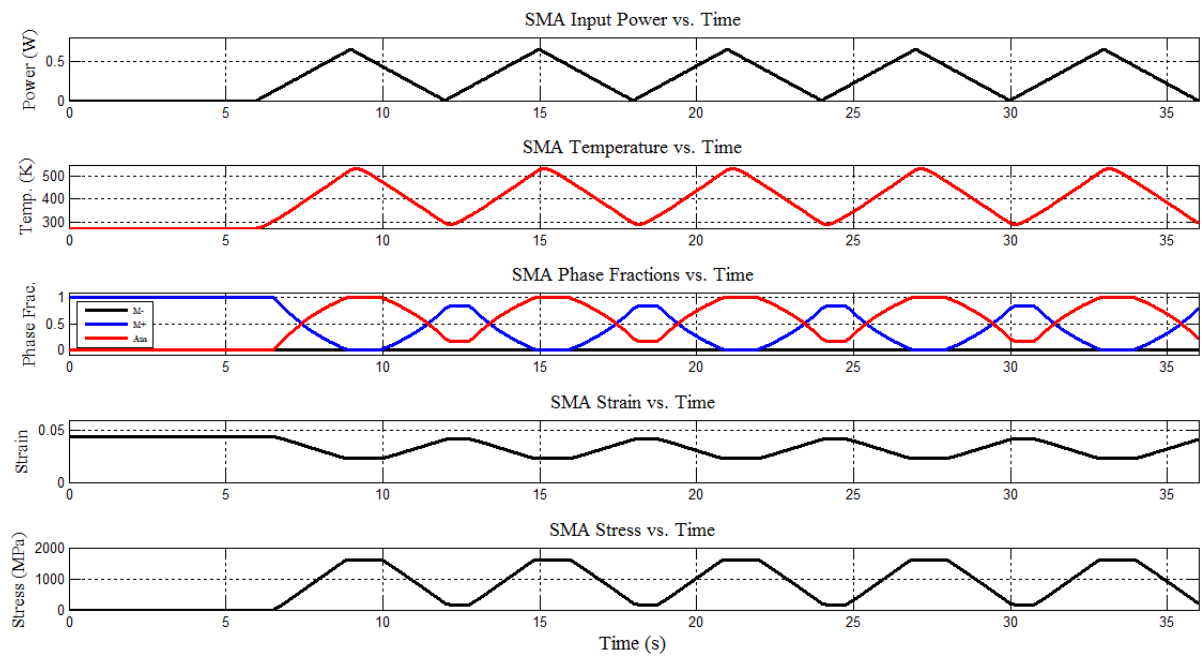


Figure 104: SMA wire with spring schematic.

Table 12: SMA with Spring, Initial Conditions and Model Parameters.

Parameter	Variable	Value
Spring Stiffness	k_{spring}	3.0e+03 N/m
SMA radius	r_{SMA}	25.0e-6 m
SMA length	L_{SMA}	0.05 m
Initial Condition: Martensite+	M_{+o}	100%
Initial Condition: Martensite-	M_{-o}	0%
Initial Condition: Pre-stress	σ_o	0.0 MPa
External Temperature	T_{ext}	273.0 K

**Figure 105:** Time resolved concentrated load and power input to SMA actuator and corresponding temperature, phase fractions, strain and stress responses.

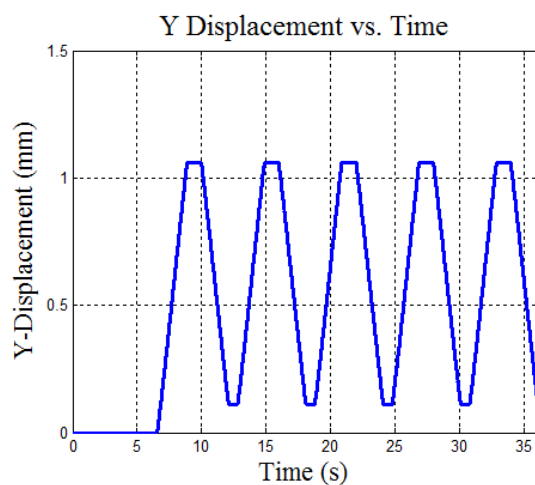
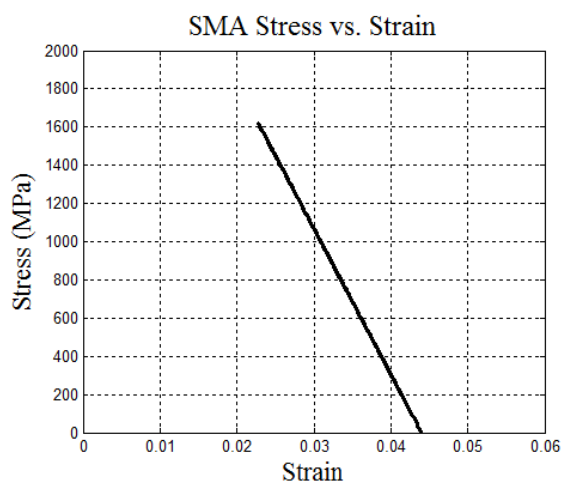


Figure 106: SMA Wire tip displacement versus time response.

a



b

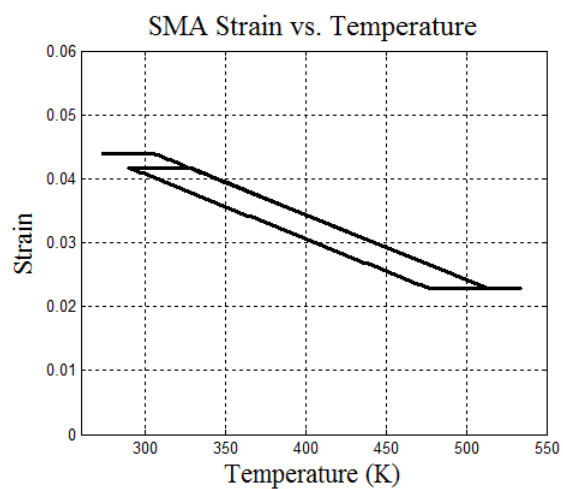


Figure 107: (a) Stress versus strain and (b) strain versus temperature relationships.

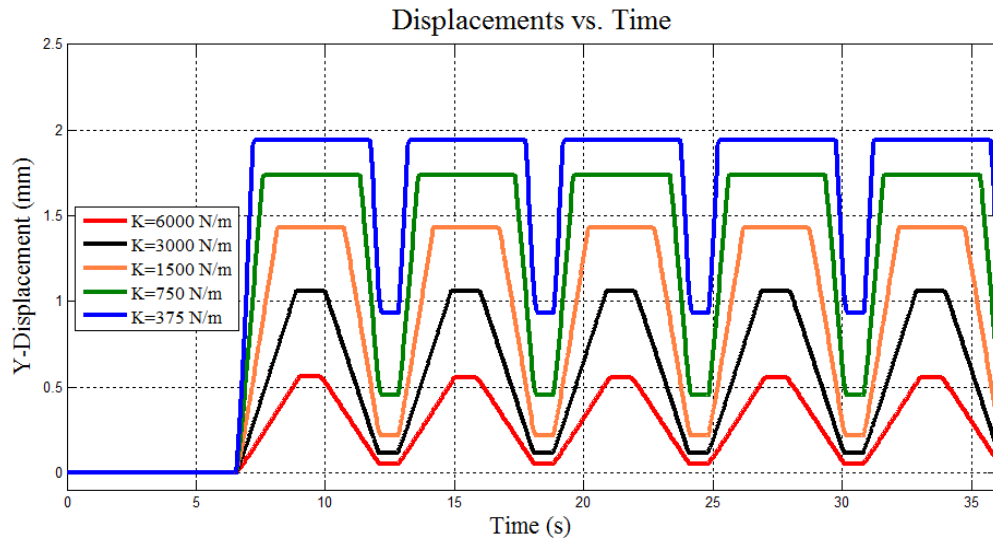


Figure 108: SMA wire tip displacement for different spring stiffness values.

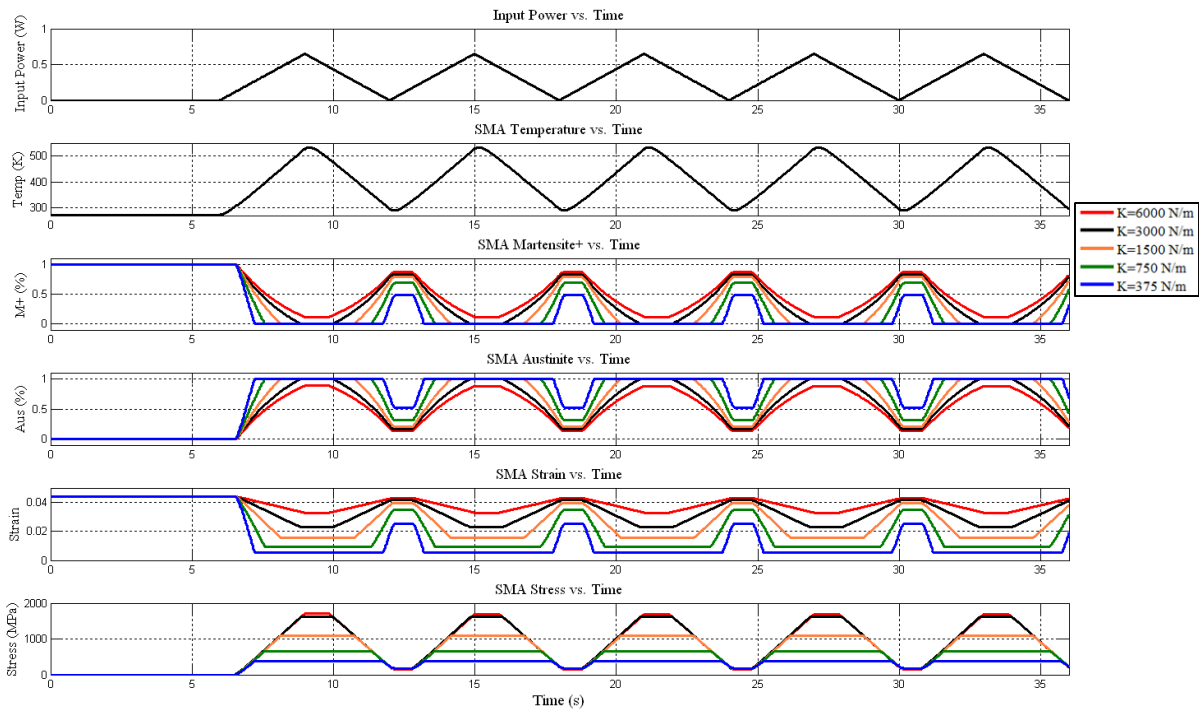


Figure 109: Time resolved power input to SMA actuator and corresponding temperature, phase fractions, strain and stress responses for different spring stiffness values.

Appendix C: UMAT Code

```

SUBROUTINE UMAT (STRESS, STATEV, DDSDE, SSE, SPD, SCD, RPL, DDSDDT,
&               DRPLDE, DRPLDT, STRAN, DSTRAN, TIME, DTIME, TEMP,
&               DTEMP, PREDEF, DPRED, CMNAME, NDI, NSHR, NTENS,
&               NSTATV, PROPS, NPROPS, COORDS, DROT, PNEWDT, CELENT,
&               DFGRD0, DFGRD1, NOEL, NPT, LAYER, KSPT, KSTEP, KINC)

INCLUDE 'ABA_PARAM.INC'

INTEGER        NPROPS, NDI, NSHR, NTENS, NSTATV, NOEL, NPT, LAYER,
&              KSPT, KSTEP, KINC
DOUBLE PRECISION
&              STRESS(NTENS), STATEV(NSTATV), DDSDE(NTENS,NTENS), SSE,
&              SPD, SCD, RPL, DDSDDT(NTENS), DRPLDE(NTENS), DRPLDT,
&              STRAN(NTENS), DSTRAN(NTENS), TIME(2), DTIME, TEMP, DTEMP,
&              PREDEF(1), DPRED(1), PROPS(NPROPS), COORDS(3), DROT(3,3),
&              PNEWDT, CELENT, DFGRD0(3,3), DFGRD1(3,3)

CHARACTER*80, CMNAME

INTEGER        n, lwork, liwork, ijac, mljac, imas, iout, itol, mlas,
&              mumas, idid, mujac, ipar, i

PARAMETER ( n=3, lwork=4*n*n+12*n+20, liwork=3*n+20

DOUBLE PRECISION
              work(lwork), reltol, abstol, rpar, f(n), nf(n)

INTEGER        iwork(liwork

INTEGER        htinc

EXTERNAL       fcn, jac, mas,

DOUBLE PRECISION
              props_dum(100), stran_dum, dstran_dum, time_dum, dtime_dum

DOUBLE PRECISION
              prestran, X1b4, X2b4, newdstran(1), taua, taum, xpls, xmns,
&              ppa, tau, pap, pma, pam, xaus, X3, tempi, rpaus, rppls,
&              rpmns, rpsma, rtotal, newheat, heatrate, prevh, presdv4,
&              temp_dum, dtemp_dum, elevolume, wa, wm, deltaBT, a1, a2,
&              a3, a4, a5, b1, b2, b3, b4, b5, c1, c2, c3, c4, c5, G1, G2,
&              G3, G4, G5, lamda, kb, ppa2, pap2, pma2, pam2, pma3,
&              Gmnsaus, Gausmns, Gauspls, Gplsaus, gam1, gam2, gam3, gam4,
&              gam5, nic3, c22, Em2, gamt2, Ea2, statev8, statev9

COMMON /ALLPROPS/ props_dum
COMMON /TIMEPS/ stran_dum, dstran_dum, time_dum, dtime_dum
COMMON /TEMP/ temp_dum, dtemp_dum

```

```

prestran      = props(30)
stran_dum    = stran(1)+prestran
dstran_dum   = dstran(1)
time_dum     = time(2)
dtime_dum    = dtime
X1b4        = statev(1)
X2b4        = statev(2)
kb          = 1.38044D-23
c
temp_dum = TEMP    !!add for inhomogeneous temperature profiles
dtemp_dum = DTEMP  !!add for inhomogeneous temperature profiles
c  Implement cyclic heating
if (props(35) .eq. 0.0D0) then      ! Step Input Heating Values
    htinc = 37
    do while (time(2) .ge. props(htinc))
        props(16) = props(htinc)    ! htstart, re-write over props(16)
        props(17) = props(htinc+1) ! htend, re-write over props(17)
        props(18) = props(htinc+2) ! htampl, re-write over props(18)
        if (time(2) .le. props(htinc+1)) then
            statev(4) = props(18)
        else
            statev(4) = 0.0D0
        endif
        htinc = htinc + 3           ! increment
    enddo
endif
c
htinc = 0
newheat = 0.0D0
heatrate = 0.0D0
presdv4 = statev(4)
c
if (props(35) .eq. 1.0D0) then ! Ramp Input Heating Values
    htinc = 37
    do while (time(2) .ge. props(htinc))
        prevh = props(htinc-1) ! previous htampl
        props(16) = props(htinc)    ! htstart, re-write over props(16)
        props(17) = props(htinc+1) ! htend, re-write over props(17)
        props(18) = props(htinc+2) ! htampl, re-write over props(18)
        if (time(2) .le. props(htinc+1)) then
            newheat = props(18)
        else
            newheat = 0.0D0
        endif
        heatrate = (newheat-prevh) / (props(17)-props(16))
        props(18) = heatrate*dtime + presdv4
        statev(4) = props(18)
        htinc = htinc + 3           ! increment
    enddo
endif

```

```

c
do i = 1,nprops
    props_dum(i) = props(i)
enddo

c Preparation for RADAU5
ijac = 0 ; mljac = n
imas = 0 ; itol = 0 ; imas = 0
mlmas = 0 ; mumas = 0 ; idid = 0
iout=0
c
do 10 i=1,liwork
    iwork(i) = 0
    work (i) = 0.0D0
10 continue
    iwork(2) = 500000
    abstol = props(4)
    reltol = props(4)
        !--
c
CALL RADAU5 ( n, fcn, time(2), statev, time(2)+dtime,
&           dtime/10.0d0, reltol, abstol, itol, jac,
&           ijac, mljac, mujac, mas, imas,
&           mlmas, mumas, solout, iout, work,
&           lwork, iwork, liwork, rpar, ipar, idid)
c
CALL taugamma(stress(1),stran_dum+dstran_dum,statev,n)

CALL tauvont(taua,taum,statev(3),statev(1),statev(2)) !!homogeneous
CALL tauvont(taua,taum,temp,statev(1),statev(2))      !!inhomogeneous

CALL pplsa (ppa,stress(1),taum,statev(3)) !!homogeneous
CALL pplsa (ppa,stress(1),taum,temp) !!homogeneous
CALL papls (pap,stress(1),taua,statev(3)) !!homogeneous
CALL papls (pap,stress(1),taua,temp) !!inhomogeneous
CALL pmnsa (pma,stress(1),taum,statev(3)) !!homogeneous
CALL pmnsa (pma,stress(1),taum,temp) !!inhomogeneous
CALL pamns (pam,stress(1),taua,statev(3)) !!homogeneous
CALL pamns (pam,stress(1),taua,temp) !!inhomogeneous

X3 = 1.0D0 - (statev(1) + statev(2))

f(1) = -statev(1)*ppa + X3*pap
f(2) = -statev(2)*pma + X3*pam

CALL Stiffness( statev(1), statev(2), f(1), f(2), dtime, dstran(1),
&              stran_dum+dstran(1), ddsdde(1,1), time(2),
&              X1b4 ,X2b4 , statev(8), statev(9), statev(11) )
! For inhomogeneous temperature profiles, calculate RPL term below
RPL = ((statev(4)/props(27))-(2*props(20)*((temp_dum+dtemp_dum)-
&      props(19)))/props(23))+f(1)*props(29)+f(2)*props(29)

```

```

!
statev(3) = statev(3)  !!homogeneous temperature profiles
statev(3) = RPL       !!inhomogeneous temperature profiles
statev(5) = dstran(1)
statev(6) = ddsdde(1,1)
statev(7) = dtime_dum
statev(10) = 0.0D0

RETURN
END

```

Subroutines

```

SUBROUTINE      fcn (n, t, y, f, rpar, ipar)
IMPLICIT NONE
c Declare IO variables
INTEGER        n, ipar
DOUBLE PRECISION t, y(n), f(n), rpar, props(100)
COMMON         /ALLPROPS/ props
c Declare local variables
INTEGER        i
DOUBLE PRECISION tau, gam, taua, taum, xpls, xmns, xaus, hpls, hmns,
&              wcoeff, cv, rho, extemp, temp, joule, pap, pam, pma,
&              ppa, thrmswtch, querfl, laeng0, oberfl, wa, wm,
&              deltaBT, a1, a2, a3, a4, a5, b1, b2, b3, b4, b5, c1,
&              c2, c3, c4, c5, G1, G2, G3, G4, G5, Gmnsaus, Gausmns,
&              Gauspls, Gplsaus, lamda, kb, ppa2, pap2, pma2, pam2,
&              gam1, gam2, gam3, gam4, gam5, Em2, Ea2, gamt2

wcoeff      = props(20)
cv           = props(21)
rho         = props(22)
extemp      = props(19)
thrmswtch   = props(28)
querfl      = props(25)
laeng0      = props(24)
oberfl      = props(26)
kb          = 1.38044D-23

xpls = y(1)  ;  xmns = y(2)  ;  temp = abs(y(3))
xaus = 1.0D0 - xpls - xmns

CALL strnctrl(gam,t)
CALL tempctrl(temp,t)  !!for inhomogeneous temperature profiles
CALL taugamma(tau,gam,y,n)
CALL tauvont(taua,taum,temp,xpls,xmns)
CALL elektro(joule,t)
CALL latent(hpls,hmns,tau)

```

```

CALL ppls (ppa, tau, taum, temp)
CALL papls (pap, tau, taua, temp)
CALL pmnsa (pma, tau, taum, temp)
CALL pamns (pam, tau, taua, temp)

f(1) = -xpls*ppa + xaus*pap
f(2) = -xmns*pma + xaus*pam
! for homogeneous temperature profiles
f(3) = thrmswtch*(-wkoeff*oberfl*(temp-extemp)/rho/cv/laeng0/
&          querfl+joule/rho/cv/laeng0/querfl
&          +f(1)*hpls/rho/cv + f(2)*hmns/rho/cv)
!
! for inhomogeneous temperature profiles
f(3) = temp
!
RETURN
END

```

```

SUBROUTINE taugamma (tau, gam, y, n)
IMPLICIT NONE
INTEGER,          INTENT(IN)   :: n
DOUBLE PRECISION, INTENT(IN)   :: gam,  y(n)
DOUBLE PRECISION, INTENT(OUT)  :: tau
DOUBLE PRECISION :: term1, term2
DOUBLE PRECISION gamt, ea, props(100)
COMMON /ALLPROPS/ props

ea      = props(6)
em      = props(7)
gamt    = props(8)

term1 = gam - y(1)*gamt + y(2)*gamt
term2 = y(1) + y(2) + (em/ea) * (1 - y(1) - y(2))
tau = em * term1 / term2
RETURN
END

```

```

SUBROUTINE tauvont (taua, taum, temp, xpls, xmns)
IMPLICIT NONE
DOUBLE PRECISION, INTENT(IN) :: temp, xpls, xmns
DOUBLE PRECISION, INTENT(OUT) :: taua, taum
DOUBLE PRECISION tu, tuo, tauatu, tauato, delta
DOUBLE PRECISION :: m, b, modify_taua, c_ModTauaFact

```

```

DOUBLE PRECISION props(100)
COMMON /ALLPROPS/ props

tu          = props(9)      ! Low Temperature
tuo         = props(11)
tauatu     = props(10)    ! Transformation stress at tu
tauato     = props(12)    ! Transformation stress at to
delta      = props(13)    ! Hysteresis width
c_ModTauaFact = props(2)  ! Factor for the transformation
c          stress vs. phase fraction slope
taua = tauatu + (tauato-tauatu)/(to-tu)*(temp-tu)
taua = tauatu + (tauato-tauatu)/(tuo-tu)*(temp-tu)
taua = max(taua, 0.0D0)
m = 2.0D0 * taua * c_ModTauaFact
b = taua * c_ModTauaFact
modify_taua = ( m * xpls ) + ( m * xmns ) - b
taua = taua + modify_taua
taum = taua - delta
RETURN
END

SUBROUTINE stiffness ( X1, X2      ,
&                    dX1dt , dX2dt ,
&                    dtime  , dstran ,
&                    stran  , ddsdde ,
&                    time   , X1b4  ,
&                    X2b4   , seconds ,
&                    thirds , dsigs  )

IMPLICIT NONE
DOUBLE PRECISION, INTENT(IN) :: X1      ,
                                X2      ,
                                dX1dt   ,
                                dX2dt   ,
                                dtime    ,
                                dstran   ,
                                stran    ,
                                time     ,
                                X1b4     ,
                                X2b4     ,
DOUBLE PRECISION, INTENT(OUT) :: ddsdde(1,1) ,
                                seconds(1)   ,
                                thirds(1)    ,
                                dsigs(1)

DOUBLE PRECISION props(100)
COMMON /ALLPROPS/ props
DOUBLE PRECISION :: num      ,

```

```

&          denom      ,
&          dsigde     ,
&          ddX1num    ,
&          ddX1denom  ,
&          dsigdX1    ,
&          ddX2num    ,
&          ddX2denom  ,
&          dsigdX2    ,
&          dX1        ,
&          dX2        ,
&          ddsddepre  ,
&          second     ,
&          third      ,
&          fourth     ,

ddsdde(1,1) = 0.0D0
num = props(7)*(stran-(X1-X2)*props(8))
denom = (X1+X2+(props(7)/props(6))*(1.0D0-X1-X2))
dsigde = props(7)/denom
ddX1num = -1.0D0*props(7)*props(8)
ddX1denom = 1.0D0 - props(7)/props(6)
dsigdX1 = (ddX1num*denom - ddX1denom*num) / (denom**2)
ddX2num = props(7)*props(8)
ddX2denom = 1.0D0 - props(7)/props(6)
dsigdX2 = (ddX2num*denom - ddX2denom*num) / (denom**2)
dsigs(1) = dsigde
IF (dstran .eq. 0.0D0) then
  ddsdde(1,1) = dsigde
  seconds(1) = 0.0D0
  thirds(1) = 0.0D0
ELSE
  ddX1num = -1.0D0*props(7)*props(8)
  ddX1denom = 1.0D0 - props(7)/props(6)
  dsigdX1 = (ddX1num*denom - ddX1denom*num) / (denom**2)
  second = dsigdX1*dtime/dstran
  seconds(1) = second
  ddX2num = props(7)*props(8)
  ddX2denom = 1.0D0 - props(7)/props(6)
  dsigdX2 = (ddX2num*denom - ddX2denom*num) / (denom**2)
  third = dsigdX2*dtime/dstran
  thirds(1) = third
  fourth = second + third
  ddsdde(1,1) = dsigde + fourth      !--
END IF
seconds(1) = 0.0D0
thirds(1) = 0.0D0
ddsdde(1,1) = dsigde
RETURN
END

```

```

SUBROUTINE pplsa(ppa,sig,sgm,temp)
IMPLICIT NONE
DOUBLE PRECISION, INTENT(IN)  :: sig,sgm,temp
DOUBLE PRECISION, INTENT(OUT) :: ppa
DOUBLE PRECISION taux,gamt,ea,em,kb,vs,pi,Z,alpha,A,B
DOUBLE PRECISION DERFCX
DOUBLE PRECISION props(100)
COMMON /ALLPROPS/ props
taux = props(15)      ! Relaxation time
ea   = props(6)       ! Austenite elastic modulus
em   = props(7)       ! Martensite elastic modulus
vs   = props(14)      ! Activation volume
kb   = 1.38044d-23
pi   = 4.0d0*DATAN(1.0d0)
alpha = SQRT( vs / ( 2.0D0 * em * kb * temp ) )
Z = alpha * ( sgm - sig )
A = 1.0D0 / taux
B = SQRT(pi) / 2.0D0
ppa = A * ( 1.0D0 / ( B * DERFCX( Z ) ) )
RETURN
END

```

```

SUBROUTINE papls(pap,sig,siga,temp)
IMPLICIT NONE
DOUBLE PRECISION, INTENT(IN)  :: sig,siga,temp
DOUBLE PRECISION taux,gamt,ea,em,kb,vs,pi
DOUBLE PRECISION alpha,Z,DZ,A,num,den
DOUBLE PRECISION DERFC
DOUBLE PRECISION props(100)
COMMON /ALLPROPS/ props
taux = props(15)
ea   = props(6)
em   = props(7)
vs   = props(14)
kb   = 1.38044d-23
pi   = 4.0d0*DATAN(1.0d0)
alpha = SQRT( vs / ( 2.0D0 * ea * kb * temp ) )
Z = alpha * ( siga - sig )
DZ = alpha * 2.0D0 * siga
A = 1.0D0 / taux
IF (DZ.LE.(0.4D0)) THEN
    DZ = 0.4D0
ELSE ; END IF
num = EXP( -( Z**2 ) )
IF (Z.LE.(-5.5D0)) THEN
    pap = A * ( -SQRT( pi ) * Z )

```

```

ELSEIF ((Z-DZ).GE.(5.5D0)) THEN
  pap = 0.0D0
ELSE
  pap = A * ( num / den )
END IF
RETURN
END

```

```

SUBROUTINE pmnsa(pma,sig,sign,temp)
IMPLICIT NONE
DOUBLE PRECISION, INTENT(IN)  :: sig,sign,temp
DOUBLE PRECISION, INTENT(OUT) :: pma
DOUBLE PRECISION taux,gamt,ea,em,kb,vs,pi
DOUBLE PRECISION Z,alpha,A,B
DOUBLE PRECISION DERFCX
DOUBLE PRECISION props(100)
COMMON /ALLPROPS/ props
taux = props(15)
ea   = props(6)
em   = props(7)
vs   = props(14)
kb   = 1.38044d-23
pi   = 4.0d0*DATAN(1.0d0)
alpha = SQRT( vs / ( 2.0D0 * em * kb * temp ) )
Z = alpha * ( sign + sig )
A = 1.0D0 / taux
B = SQRT(pi) / 2.0D0
pma = A * ( 1.0D0 / ( B * DERFCX( Z ) ) )
RETURN
END

```

```

SUBROUTINE pamns(pam,sig,siga,temp)
IMPLICIT NONE
DOUBLE PRECISION, INTENT(IN)  :: sig,siga,temp
DOUBLE PRECISION, INTENT(OUT) :: pam
DOUBLE PRECISION taux,gamt,ea,em,kb,vs,pi
DOUBLE PRECISION alpha,Z,DZ,A,num,den
DOUBLE PRECISION DERFC
DOUBLE PRECISION props(100)
COMMON /ALLPROPS/ props
taux = props(15)
ea   = props(6)
em   = props(7)
vs   = props(14)

```

```

kb      = 1.38044d-23
pi      = 4.0d0*DATAN(1.0d0)
alpha = SQRT( vs / ( 2.0D0 * ea * kb * temp ) )
Z = alpha * ( siga + sig )
DZ = alpha * 2.0D0 * siga
A = 1.0D0 / taux
IF (DZ.LE.(0.4D0)) THEN
    DZ = 0.4D0
ELSE ; END IF
num = EXP( -( Z**2 ) )
den = ( SQRT(pi) / 2.0D0 ) * ( DERFC( Z - DZ ) - DERFC( Z ) )
IF (Z.LE.(-5.5D0)) THEN
    pam = A * ( -SQRT( pi ) * Z )
ELSEIF ((Z-DZ).GE.(5.5D0)) THEN
    pam = 0.0D0
ELSE
    pam = A * ( num / den )
END IF
RETURN
END

```

```

SUBROUTINE tempctrl(temp,time)  !!only for inhomogeneous profiles
IMPLICIT NONE
DOUBLE PRECISION, INTENT(IN) :: time
DOUBLE PRECISION, INTENT(OUT) :: temp
REAL*8      temp_dum, dtemp_dum
COMMON /TEMP/ temp_dum, dtemp_dum
Temp = 1.0D0*(temp_dum+dtemp_dum)
RETURN
END

```

```

SUBROUTINE strnctrl(strain,time)
IMPLICIT NONE
DOUBLE PRECISION, INTENT(IN) :: time
DOUBLE PRECISION, INTENT(OUT) :: strain
REAL*8      stran_dum,dstran_dum,time_dum,dtime_dum, epsdot
COMMON /TIMEPS/ stran_dum,dstran_dum,time_dum,dtime_dum
strain = 1.0d0*(dstran_dum / dtime_dum)*(time-time_dum)+stran_dum
RETURN
END

```

```
SUBROUTINE latent(hpls,hmns,tau)
IMPLICIT NONE
REAL*8 hpls,hmns,tau
REAL*8 props(100)
COMMON /ALLPROPS/ props
hpls = props(29)
hmns = props(29)
RETURN
END
```

```
SUBROUTINE elektro(joule,t)
IMPLICIT NONE
REAL*8 joule,t
REAL*8 htstart,htend,htampl
REAL*8 props(100)
COMMON /ALLPROPS/ props
htstart = props(16)
htend = props(17)
htampl = props(18)
if (t .ge. htstart .and. t .lt. htend) then
    joule = htampl
else
    joule = 0.0D0
endif
RETURN
END
```